# Development and Assessment of a Soda Lime Glass Model for Ballistic Impact

Prusodman Sathananthan

A thesis
presented to the University of Waterloo
in fulfilment of the
thesis requirement for the degree of
Master of Applied Science
in
Mechanical Engineering

Waterloo, Ontario, Canada, 2019

# Author's Declaration

I hereby declare that I am the sole author of this thesis. This is a true copy of the thesis, including any required final revisions, as accepted by my examiners. I understand that my thesis may be made electronically available to the public.

# Abstract

Transparent armour (more commonly known as bullet-resistant glass) is used in armoured land vehicles to provide increased visibility while maintaining adequate levels of protection for the occupants. Soda-lime glass is commonly used in transparent armour due to the ease of manufacture and relatively low cost. Computational impact models of soda-lime glass can be used to aid in the development and optimization of transparent armour systems, but require experimental data to provide input parameters and must be assessed against independent impact data for model validation. In this study, a robust computation model of soda-lime glass was developed and successfully validated against a wide range of experimental data from coupon level dynamic tensile testing to full-scale ballistic impact experiments.

To support the development and validation of the computational model, three experimental tests were conducted: a dynamic diametral compression test to measure the tensile strength of the soda lime glass; a sphere ballistic impact test on glass tiles to characterize the dynamic failure of soda-lime glass over a range of impact velocities; and a depth of penetration test to validate the ballistic performance of the soda-lime glass model.

Three discretization methods commonly used to model impact problems were investigated including smooth particle hydrodynamics (SPH), element free Galerkin (EFG) and the finite element method (FEM). A first set of models were used to assess common numerical modelling techniques using the sphere on glass tile impact tests and material parameters from the literature. The Johnson Holmquist (JH-2) ceramic constitutive model, accounting for strength dependence on pressure and material damage, was used to model the response and failure of the glass. The SPH method predicted projectile residual velocities with some success (difference in residual velocities as low as 15% at lower impact speeds) but had poor convergence tendencies ($p = 1.1$). The EFG method demonstrated higher rates of convergence ($p = 2.1$) but did not predict residual velocities well (differences as high as 348% using literature parameters). Lastly, the FEM showed acceptable convergence tendencies ($p = 1.88$). Although other solution methods predicted ballistic performance more accurately using literature parameters, the methods were prone to numerical error (SPH) or computationally expensive (EFG) to use effectively. The FEM with failure treated using erosion provided a good balance between simulation accuracy and runtimes, provided that a sufficiently fine mesh, 0.5 mm in this study, was used.

In a second set of simulations, the material parameters for the JH-2 constitutive model were determined by fitting strength curves to experimental data and improved using sphere on glass impact test data. It was

determined that the fractured strength of the material (B) had a significant effect on the residual velocities of the sphere on glass impact simulations, and the damage coefficient (D1) had an effect on the mode of failure predicted. There was some interaction between the fractured strength (B) and damage coefficient (D1) on the projectile velocities, so B and D1 were determined such that they minimized the error in the residual velocity prediction in the sphere on glass tests.

The performance of the updated FEM JH-2 material model was assessed using three sets of experimental data: dynamic Brazilian test, sphere on glass tile test, and preliminary assessment using depth of penetration (DOP) tests. The proposed new material parameters in the JH-2 constitutive model predicted the failure strain and mode of failure in diametral compression samples, within the range of experimental results, demonstrating the ability to predict complex tensile failure of soda-lime glass. Although the model parameters were determined in part using the projectile kinematics of the sphere on glass tile dataset, the measured damage progression and damage propagation velocities in the tiles were used separately for partial model validation. The FEM model with updated JH-2 parameters predicted the projectile penetration in the DOP tests with a 12% difference on average. The predicted difference was as low as 6% at higher impact velocities (930 m/s), and as high 95% associated with lower impact velocities and cases where the experimental projectile path veered off-axis relative to the target. The model used quarter symmetry and did not account for this aspect of projectile motion. This was considered a preliminary assessment since variable such as friction and the projectile material properties require further investigation. The FEM and JH-2 constitutive model with updated material properties predicted a wide range of soda-lime glass impact behaviour demonstrating improved response over a range of load cases.

# Acknowledgements

First, I would like to thank my supervisor, Dr. Duane Cronin for providing me with the opportunity, the resources and the guidance to tackle such challenging problem. I would also like to thank Dilaver Singh for his sound advice and technical assistance throughout this project.

I would like to acknowledge the sponsors of this project; the Natural Sciences and Engineering Research Council of Canada, Defence Research and Development Canada – Valcartier Research Centre, Prelco Inc., General Dynamics Land Systems – Canada and the National Research Council Canada. Thank you for sponsoring this project and providing financial and technical support. Without you, this thesis would not have been possible.

Lastly, I would like to thank my family and friends for cheering me on. I am truly lucky have such amazing people in my life ☺

# List of Figures

# List of Tables

# List of Abbreviations & Symbols

| | |
|---|---|
| **ALON** | Aluminum Oxynitride |
| **BVP** | Boundary Value Problem |
| **DOP** | Depth of Penetration |
| **EFG** | Element Free Galerkin |
| **FEM** | Finite Element Method |
| **JH-2** | Johnson-Holmquist 2 Ceramics Model |
| **JH-1995** | The Set of Soda Lime Glass Parameters Proposed by Johnson & Holmquist in 1995 |
| **HEL** | Hugoniot Elastic Limit |
| **LSTC** | Livermore Software Technology Corporation |
| **PHEL** | Pressure Component of the Hugoniot Elastic Limit |
| **RE** | Richardson Extrapolation |
| **SHEL** | Deviatoric Component of the Hugoniot Elastic Limit |
| **SHPB** | Split Hopkinson Pressure Bar |
| **SLG** | Soda Lime Glass (also Soda Lime Silicate Glass) |
| **SOG** | Sphere on Glass Tests |
| **SPH** | Smooth Particle Hydrodynamics |

# 1. Introduction

## 1.1 Motivation and Need for Computational Impact Model

Transparent armour (sometimes referred to as “bullet-resistant” glass) is used in armoured land vehicles to provide protection against ballistic impacts, while maintaining adequate visibility (Talladay et al., 2014). Modern transparent armour systems consist of multiple layers of transparent ceramic (e.g. soda-lime glass, borosilicate glass, ALON, sapphire, spinel) that disrupt the impacting projectile, and a spall layer (e.g. polycarbonate) that is used to contain the resulting debris (den Reijer, 1991). There are a wide range of transparent ceramic materials that can be used in the construction of transparent armour, however soda-lime glass is commonly used due to the relatively low cost (Grujicic et al., 2012a), but often results in high mass due to the required material thickness (Strassburger, 2009). Therefore, there is a need to understand the ballistic performance of glass and to develop tools, such as finite element models, that may be used to inform optimization of transparent armour.

To produce a robust model of soda-lime glass, experimental data is required to calibrate and validate computational models such that one can have confidence in the model to predict real world phenomena (ASME, 2006). There are two limitations with the available experimental data at the present time. First, there are few tests that study the damage progression of impacted planar targets. Although literature data that characterizes soda-lime glass under ballistic loading exists, the studies focus on non-planar targets, and do not present features typically seen in the impact of ceramic armour (e.g. fracture cones, radial cracks, edge cracks) (Sathananthan et al., 2019). When planar targets are studied in literature, they are often studied under some level of confinement, creating complex boundary conditions and making modelling of such tests difficult. Secondly, the tensile strength of soda-lime glass is heavily dependent on pre-existing flaws in the material and is not well defined in literature, with values ranging from 20 MPa to as high as 150 MPa (van der Velde, 2015). To effectively characterize soda-lime glass for a ballistic impact model, adequate experimental data is crucial to capture key failure and deformation mechanisms such that the modelled armoured systems behave in a realistic manner.

Historically, the armour development process was labour intensive, requiring many iterations of designing and field-testing prototypes to produce suitable armour (Templeton et al., 2001). Computational models can be used to reduce the development time and development costs of transparent armour by assessing proposed armour designs computationally and thus reducing the number of field tests required (Templeton et al., 2001). In recent years, there have been some successes with using computational methods to model the response of transparent armor in ballistic impact applications (Grujicic et al., 2011; Zhang et al., 2015; Binar et al., 2018; Dorogoy et al., 2019), and even some success in using these models to aid in the development of transparent armour (Antoine et al., 2015). The goal of a ballistic ceramics model is to accurately predict how the ceramic will respond and fail under impact loading conditions, thereby predicting the kinematics of the projectile. Current ballistic models of soda-lime glass excel at capturing projectile kinematics and local pulverization of material (Anderson, 2007), a level of detail that may be sufficient to model single impacts. However, these models are often limited in their capability to capture many other damage features commonly observed in the impact of planar soda-lime glass targets that may be important for simulating multiple impacts on transparent armour. Multiple impacts are required in many test standards (e.g. NATO Standards Organization, 2011; Grujicic et al., 2012), and therefore optimization of transparent armour also needs to consider multiple impacts.

## 1.2 Scope of Work and Objectives

This study aims to develop and assess a computational model of soda-lime glass for ballistic applications. Before a model is produced and validated, experimental data is required to adequately characterize soda-lime glass under ballistic impact conditions. The five (5) major objectives of the current study included:

O1. Perform a literature review covering current ceramic test methods and modelling techniques pertaining to ballistic impact.
O2. Gather sufficient material data (through O1 and additional experimental testing) to represent soda-lime glass in an existing constitutive model.
O3. Assess and identify suitable numerical methods for simulating ballistic impact of glass.
O4: Finalize constitutive model parameters for soda-lime glass.
O5. Validate a soda-lime glass model for use in depth-of-penetration ballistic impact applications, using projectile kinematics as the metric of validation.

Although the primary aim of this thesis was to develop and validate a ballistic model of soda-lime glass, this research study also developed tools and techniques that can be extended for use in the development and optimization of protective armour systems.

## 1.3 Structure of Thesis

Chapter 2 reviews the current literature, surveying the current experimental and numerical techniques used to understand the ballistic impact of ceramics, and in particular, techniques used to characterize and model soda-lime glass, while identifying any limitations in the field where applicable (O1).

Chapter 3 covers the experimental methods used in this study to bridge the gap in experimental data identified in Chapter 2,that are required to fully represent soda-lime glass under ballistic impact conditions. These experiments included measurement of the tensile strength of soda-lime glass at high deformation rate though a dynamic Brazilian splitting test, quantifying the rate of damage accumulation of glass through the sphere on glass tile tests, and assessing the ballistic performance of soda-lime glass using a depth-of-penetration test.

Chapter 4 presents the results from the experimental tests, as well as any limitations with the test methodologies. The data is presented such that it could be directly used to verify, calibrate and validate a ballistic model of soda-lime glass (O2).

Chapter 5 details the numerical models used to develop and assess a ballistic model of soda-lime glass. This chapter only serves to describe the construction of the models, including specifics on the modelling techniques used in the study, model geometry, and material properties.

Chapter 6 describes the application of the numerical models to meet the final three objectives of this study: to verify, calibrate and validate a ballistic model of soda lime glass (O3, O4 & O5). Limitations of the current methodology are also identified, including limitations in the numerical methods implemented and the constitutive model used in this work.

Finally, Chapter 8 summarises the major findings of this work and suggests pertinent next steps to guide future endeavours.

# 2. Literature Review

## 2.1 Phenomenology of a Ballistic Impact on a Ceramic Target

Ballistic impact is described by a free-flight projectile that uses kinetic energy to penetrate or perforate a target (Zukas, 2004), where the projectiles are much smaller than the targets (Naik, 2006). Ballistic impacts occur at high velocities ranging from few hundred metres per second for small arms fire (NATO Standards Organization, 2011) to several kilometres per second for shaped charges (Birkhoff, 1948). Upon impact, massive pressures are induced in the interacting materials with deformations at strain rates of up to $10^6$ $s^{-1}$ at the point of impact and $10^2$ $s^{-1}$ in the surrounding regions (Sharpe, 2008). An impact can be described in three phases of response (Zukas, 2004) (Figure 1) initial impact generating high pressures and stresses in the materials in the first few microseconds after initial impact, local deformation where damage initiates and propagates away from the impact location up to tens of microseconds, and structural response corresponding to large-scale deformation of the target.

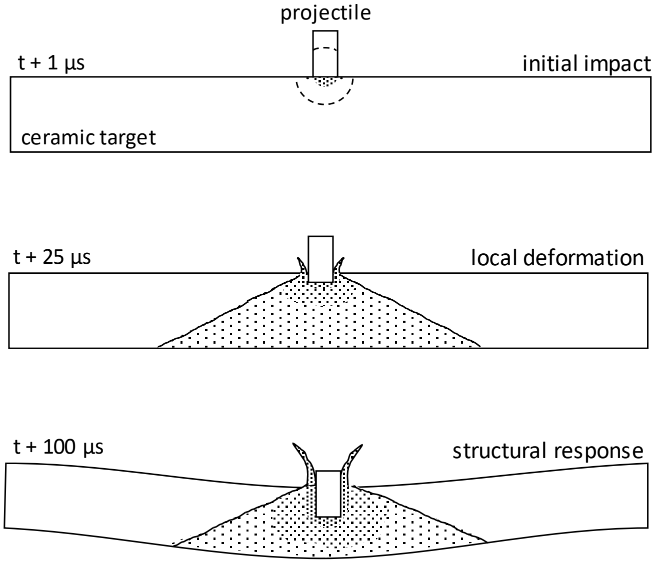

*Figure 1: Phases of response during a ballistic impact: initial, local and structure responses*

To understand the sequence of events that occur during a ballistic impact, consider a cylindrical projectile impacting a ceramic target (Figure 2A). When first contact is made at $t_0$, stress waves initiate at the impact location and propagate through the target and projectile (initial loading). The stresses are compressive at the point of impact and can reach magnitudes on the order of gigapascals (Chaudri, 2015) (Figure 2B), while shear and tensile stress waves propagate across the adjacent free surface of the material. The development of these stress waves result in local deformation of the target and projectile, leading to localized failure of the materials.

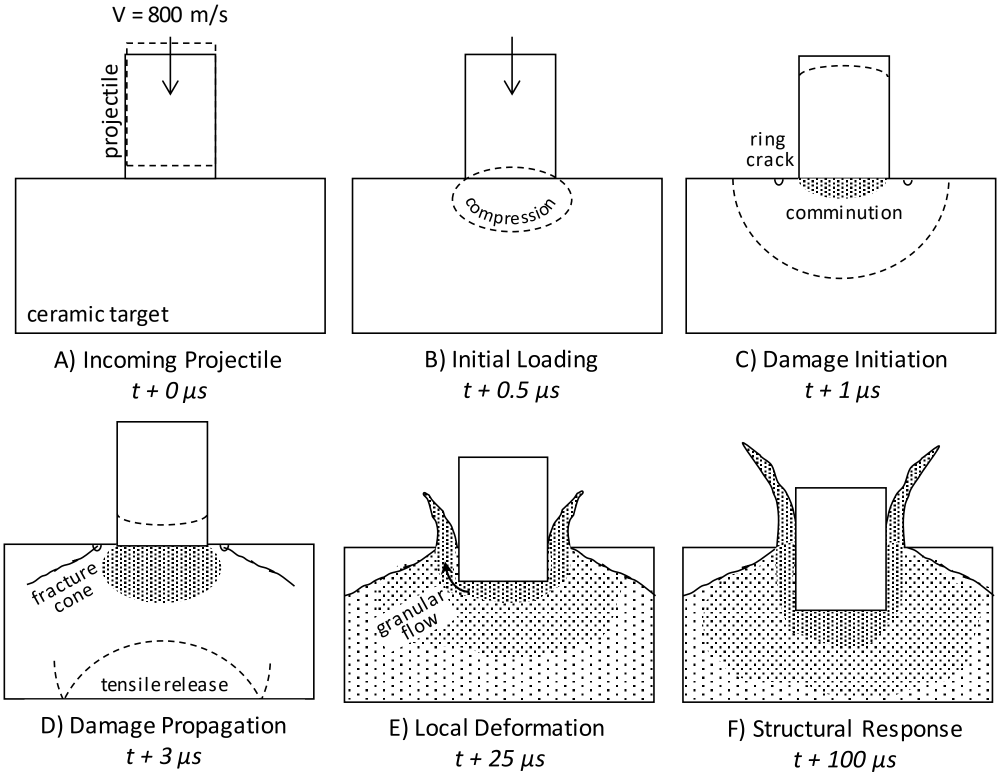

A) Incoming Projectile *t + 0 µs*
B) Initial Loading *t + 0.5 µs*
C) Damage Initiation *t + 1 µs*
D) Damage Propagation *t + 3 µs*
E) Local Deformation *t + 25 µs*
F) Structural Response *t + 100 µs*

*Figure 2: Stages of damage progression in a ceramic during the local deformation phase.*

The tensile stresses at the surface of the target form shallow ring cracks that extend into the material at an angle ranging from 25°to 75° (Chaudri et al., 1978) (Figure 2C) eventually leading to a fracture cone. Under the point of impact, a fine network of pulverized or comminuted material is created through linking of micro-fractures (Figure 2C) and enables the target material to absorb large amounts of energy (Mescall, 1983). At this point, the individual ring cracks have coalesced into a single fracture cone (Figure 2D) and the peak stresses in the target have been reached. Once the material under the point of impact has reached a fully comminuted state, it behaves like a granular material (Curran et al., 1994) and begins to flow around the projectile (Figure 2E), allowing the projectile to intrude or penetrate into the target. The target subsequently undergoes a structural response (Figure 2F) corresponding to large scale deformation.

If the target is planar in nature (length and width much larger than the thickness), the target can experience high flexural stresses over the upper and lower surfaces, resulting in the formation of concentric cracks (Thornton et al., 1986) around the point of impact.  The bending stresses can also generate radial cracks (Thornton et al., 1986) that extend outwards from the point of impact to the extremities of the target (Figure

3). As the compressive stress waves reach the free surfaces of the target, the stress waves reflect in the opposite sense, resulting in a tensile release waves (Wilkins, 1978) and potentially internal rupture (spall) of the ceramic material, forming edge cracks. If the target is sufficiently damaged, the projectile will pass through the target, resulting in perforation.

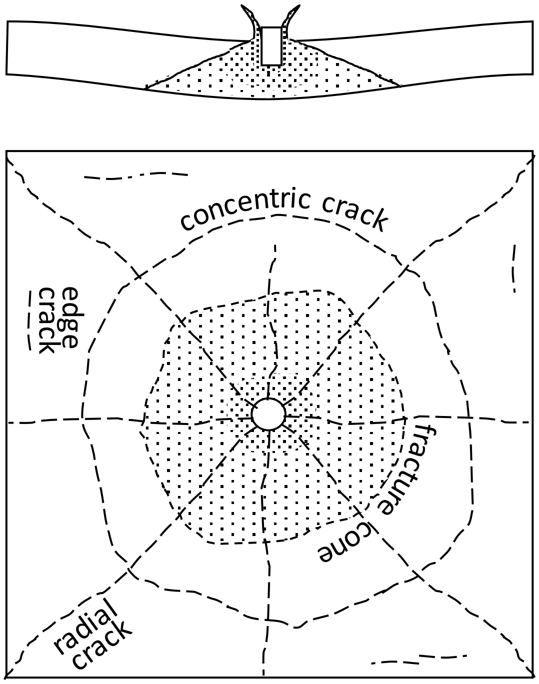

*Figure 3: Features of planar impact damage typically seen during ballistic impact of ceramics*

## 2.2 Deformation and Failure Mechanisms in Ceramic Materials

During a ballistic impact, materials may deform, damage and fail; and more than one failure mechanism may be active, making it difficult to associate a specific failure mechanism to the resultant kinematic behaviour of the projectile (Wilkins, 1987). The goal of a ballistic ceramics model is to predict how the ceramic will respond and fail under impact loading conditions, thereby predicting the kinematics of the projectile.

The behaviour of brittle materials, such as ceramics, are heavily dependent on the distribution of flaws in the material (Griffith, 1920). These flaws act as points of failure through the promotion of crack growth. As a load is applied, small defects in the material provide points of crack initiation. Once cracks initiate, they will grow until they meet other cracks and combine (coalesce) (Rajendran & Bless, 1996). These cracks behave differently in both tension and compression. Three mechanisms will be discussed in the following section; fracture (tension), comminution (compression) and plastic deformation (very high pressures).

Under little or no hydrostatic pressure and at room temperature, ceramics behave as a brittle solid (i.e.: linear elastic until catastrophic failure) (Callister, 1991). If the tensile strength of the material is exceeded, the material will fracture. The energy required to form a crack (or a surface) per unit area is the following (Grady, 1983):

$$\gamma = \frac{K_{IC}^2}{2\rho c_o^2} \qquad \text{Equation 1}$$

where $\gamma$ is the surface energy per unit area, $K_{IC}$ is the mode I fracture toughness of the material, $\rho$ is the material density and $c_o$ is the longitudinal wave speed in the material. Under compressive stresses, cracks are constrained from extending. The applied compressive load must be overcome to continue to grow a crack perpendicular to direction of loading. However, further crack extension can still develop parallel to the direction of loading through the growth of wing cracks. Wing cracks are secondary cracks that propagate from pre-existing flaws and form parallel to the direction of loading (Cannon, 1990). Cracks formed in compression are diffuse resulting in pulverization of material (Shockey et al., 1990), unlike cracks in tension. Bulk crushing or pulverization of the material is also referred to as comminution. Grady (1983) proposed two conditions that govern tensile failure in brittle solids that are useful in understanding the comminution process. Grady's first condition defines a zone of interaction that subdivides the material into regions that fail independently of one another and governs the maximum size of particles that can be formed during a given loading condition, where the size of these zones are inversely proportional to the strain rate. The second condition is an energy consideration that states that the total energy within one of these zones must exceed the fracture energy threshold of the material for fracture to initiate. This allows for the quantification of energy absorbed by the comminution process. The energy absorbed by a volume of comminuted material is inversely proportional to the particle size (more surfaces require more energy to form). As the strain rate increases, the material produces finer fragments and results in the dissipation of more energy per unit volume. Thus, higher applied strain rates generally enable ceramics to absorb more energy via comminution.

Once the material has reached a fully comminuted state, the damaged ceramic behaves as a granular material (Curran et al., 1994) where the primary deformation mechanisms are sliding and rotation of fragments. The strength of granular materials comes from the friction between particles. Fully comminuted material also has the unusual quality of increasing in volume when subjected to shear deformations, referred to as shear dilatancy, Reynold's dilatancy (Nedderman, 2005) or material bulking (Rajendran & Bless, 1996), (Johnson & Holmquist, 1995). When sheared, neighbouring particles must leave their fully consolidated state (most closely packed state), and "ride-up" against other particles (Curran et al., 1994) resulting in an expansion of the material. Rapid expansion can also be caused by the unloading of compressive stresses in a glass upon fracture (Johnson, 1992).

True plastic deformation through slip systems in glass is only possible under large hydrostatic pressures that may be achieved in the early stages of a ballistic impact. This plastic deformation is highly dependent on the composition of the glass, with more plastic behaviour present in glasses with a higher impurity content (Hagan, 1983).

## 2.3 Ceramic Material Test Methods and Constitutive Modeling

Experimental data is required to determine material constitutive model parameters (characterize materials) and to validate numerical models (model validation) (ASME, 2006). Basic mechanical properties of soda-lime glass (such as density and Young's modulus) are typically agreed upon in literature (Table 1).

*Table 1: Material properties of soda-lime glass*

| Property | *Units* | *SLG* |
|---|---|---|
| Density | *$g/cm^3$* | 2.50* |
| Young's Modulus | *GPa* | 72.1* |
| Poisson's Ratio | - | 0.222* |
| Fracture Toughness | *$MPa\sqrt{m}$* | 0.7 – 0.8** |

*Dannemann (2011)
** Doremus (1976)

### 2.3.1 Constitutive Modelling of Ceramics

To model ceramics under ballistic impact conditions, a suitable constitutive model relating the material stress to material strain is required (Anderson et al., 1993). Ceramic constitutive models were introduced in the late 1960s, spurred on by a need for lightweight armor to defeat armour piercing projectiles (Anderson, 2007). The first ceramic constitutive model intended for ballistic impact applications was developed by Mark Wilkins (1968), was used to model thin ceramic tiles used in ceramic-metal laminates. The model incorporated tensile failure and a damage variable to track material failure. Since Wilkin's model, a multitude of ceramic material models have been developed for ballistic impact applications.

There are four approaches used to model inelastic deformation and fracture in ceramics (Rajendran, 2002): an elastic-plastic model with softening based on a state variable (e.g. Wilkins 1968); an elastic model with a fracture mechanics (Griffth, 1920) based failure criterion (e.g Mescall and Tracey, 1984); a model based in micromechanics such as the Rajendran-Grove model (1994); or an elastic-plastic model with strength reduction based on accumulated damage (Johnson & Holmquist 1992). Wilkin's original ceramics model was used to study the development of fracture cones (Anderson, 2007). The model employed a critical principal stress to determine the onset of failure, and a time delay to reach a fully failed state (fractured). Wilkin's model was able to reproduce some impact phenomena; however, the model was heavily mesh dependent and required a very fine mesh to resolve the impact (40 zones across the radius of the projectile). Implementations of fracture mechanics based models using Griffith's criterion to determine the initiation of discrete fracture of a ceramic under bi-axial loading by assuming an initial flaw distribution, allowing the model to predict many features of impact (Mescall and Tracey, 1984). However, these models have only been used to model discrete cracks (Rajendran, 1988) and not the comminution of material, a feature that accounts for a large portion of energy dissipation in ceramics (Haney & Subhash, 2012). Micromechanics based models, like the Rajendran-Grove model (1994) or the more recently Desphande-Evans model (2008) use microphysical theories and analytical models to describe the deformation of the ceramic (Desphande et al., 2008). For example, in the Rajendran-Grove model, the total deformation is split up into two parts; the deformation of the matrix (elastic) and the deformation due to cracks sliding and opening (inelastic) with the cracking modelled using fracture mechanics principles (Rajendran, 1996). These models capture some physical phenomena; however, these models are computationally expensive (Desphande et al., 2008) and historically have not performed as well as phenomenological ceramics models (Templeton, 2001).

A ceramic constitutive model should predict the material stress-strain response and damage over a broad range of conditions using one set of material parameters. Phenomenological models such as the Johnson-Holmquist ceramics model, have been successfully been applied to a variety of impact scenarios (Anderson 2007). The JH-1 (Johnson & Holmquist, 1992) model accounted for many features of ceramic materials such as pressure-dependent yielding, damage accumulation, material bulking and strain rate dependency seen in some ceramics (see section 2.3). The JH-2 model incorporated gradual reduction of strength from intact to fractured material states, and a normalized form of the intact and damage strength curves (Johnson & Holmquist, 1994). The JH-2 model has many parameters that can be determined through direct experimentation, but some parameters, such as the failed material strength (B, m, $SF_{max,}$ Equation 5) and the damage parameters (D1, D2, Equation 7), have historically been determined through inverse methods to match a set of calibration experiments (Holmquist et al., 1995). The second iteration of the Johnson-

Holmquist model (JH-2) model is implemented in several commercial FE codes (e.g. LS-DYNA) and material parameters are available for a number of ceramic materials (Cronin et al. 2003).

The JH-2 model incorporates four ceramic response features: a yield function dependent on pressure and strain-rate; a pressure dependent damage model; an equation of state; and a bulking mechanism that returns internal energy back into pressure as an element accumulates damage (Figure 4).

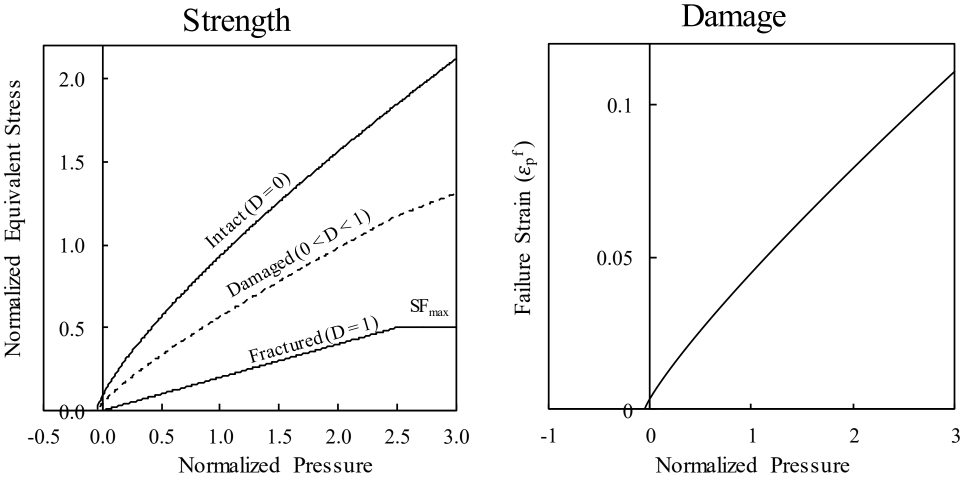

*Figure 4: Strength and damage curves implemented in the JH-2 model*

The yield strength ($\bar{\sigma}$) is scaled by the equivalent stress at the HEL (the SHEL):

$$\bar{\sigma} = SHEL * \bar{\sigma}^* \qquad \textit{Equation 2}$$

The normalized yield strength is calculated using the following equation:

$$\bar{\sigma}^* = \sigma_i^* - D\left(\sigma_i^* - \sigma_f^*\right) \qquad \textit{Equation 3}$$

where $\sigma_i^*$ is the normalized intact strength, $\sigma_f^*$ is the normalized fractured strength, D is the damage accumulated and $\sigma^*$ is the normalized yield strength. The intact and damaged strengths are defined by the following equations:

$$\sigma_i^* = A(P^* + T^*)^N(1 + C\ln\dot{\varepsilon}^*) \qquad \textit{Equation 4}$$

$$\sigma_f^* = B(P^*)^M(1 + C\ln\dot{\varepsilon}^*) \qquad \textit{Equation 5}$$

where A, N and T define the intact material curve, B and M define the fractured material curve and C and $\dot{\varepsilon}^*$ describe the strain rate dependence of the ceramic. The fractured strength, $\sigma_f^*$, can also be limited using

SF$_{max}$, a behaviour that is seen in some materials, like soda lime glass (Dannemann, 2011). The strain rate $\dot{\varepsilon}^*$ is normalized by a reference strain rate. P$^*$ and T$^*$ are the normalized hydrostatic pressure and hydrostatic tensile pressure to failure (constant) respectively.

The damage model is dependent on plastic strain increment and pressure, and is defined by the following equation:

$$D = \sum \frac{\Delta\varepsilon_p^{eq}}{\varepsilon_f^p} \qquad \textit{Equation 6}$$

where $\Delta\varepsilon_p^{eq}$ is the plastic strain increment and $\varepsilon_f^p$ is the plastic fracture strain for a given pressure and is defined by:

$$\varepsilon_f^p = D_1(P^* + T^*)^{D_2} \qquad \textit{Equation 7}$$

where D1 and D2 are material specific parameters that control the pressure dependence of the fracture strain. The last two features of the JH-2 model are the equation of state and material bulking. The equation of state before damage begins to accumulate is defined by the following:

$$P = K1\mu + K2\mu^2 + K3\mu^3 \qquad \textit{Equation 8}$$

where K1, K2, and K3 are material constants. For when the material is in net tension (pressure less than zero), the K2 and K3 terms are set to zero. Once the material begins to accumulate damage, a pressure increment is added to the equation of state:

$$P = K1\mu + K2\mu^2 + K3\mu^3 + \Delta P \qquad \textit{Equation 9}$$

### 2.3.2 Pressure-Strength Tests

The strength of ceramic materials is heavily dependent on the distribution of flaws in the material, and failure initiation at these flaws is influenced by pressure. To determine the pressure dependence of strength in ceramics, the strength is measured at various hydrostatic pressures (also referred to as a confining pressure). Typically, samples are either confined mechanically or hydraulically (Dannemann, 2011).

Under mechanical confinement, a cylindrical metal sleeve is placed around a cylindrical sample (Figure 5). The ceramic sample is then placed in compression. By measuring the strains at the surface of the metal confining sleeve, the stresses in the sleeve (and by extension, the stresses in the sample) can be determined. Once sample stresses are determined, the confining pressure can be calculated.

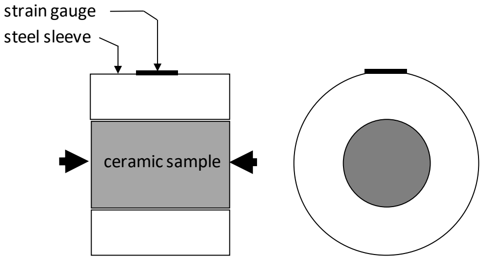

*Figure 5: A mechanically confined compression test*

Under hydraulic confinement, a cylindrical sample is surrounded by a pressurized chamber, typically filled with hydraulic fluid. The chamber is then pressurized and the sample is compressed along the axis (Figure 6). The confining pressure can be determined using the hydraulic pressure and the applied load.

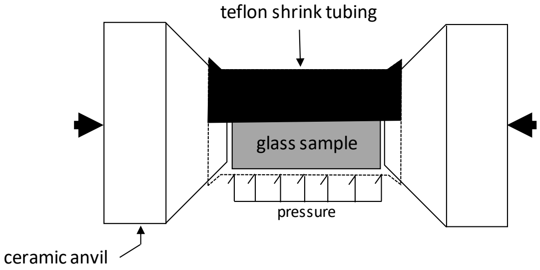

*Figure 6: A hydraulically confined compression test*

Dannemann et al. (2011) conducted a series of confined compression experiments on SLG and borosilicate glass. The confined compression experiments were primarily conducted at quasi-static rates. The quasi-static tests used cylindrical samples 6 mm in diameter and 12 mm in length made of soda lime glass. These samples precisely ground to the final dimensions, having a surface finish of 80-50 scratch-dig (a description of surface condition as defined in MIL-PRF-13830B) and parallelism of 0.005 mm (5 μm).

The cylindrical samples were confined around their circumference and compressed along their axis. Two methods of confinement were used depending on the initial confining pressure. Hydraulic confinement was used to measure material strength under 10, 50, 100, 250, 400 and 500 MPa of initial confining pressure (Figure 6). For higher pressures, the sample was mechanically confined (Figure 5) (Dannemann et al., 2011). Load cells were placed between the sample and the platens to directly measure the applied forces. Extensometers were placed on the samples to measure axial strain. This setup was used to measure axial force versus displacement (Figure 7). Using the confinement pressure and axial force, the equivalent stress could be determined. Pre-damaged samples were also tested. The samples were pre-damaged using a thermal shock process where the samples were heated to 500°C in a resistance tube furnace and twice quenched in an ice bath (Dannemann et al., 2011).

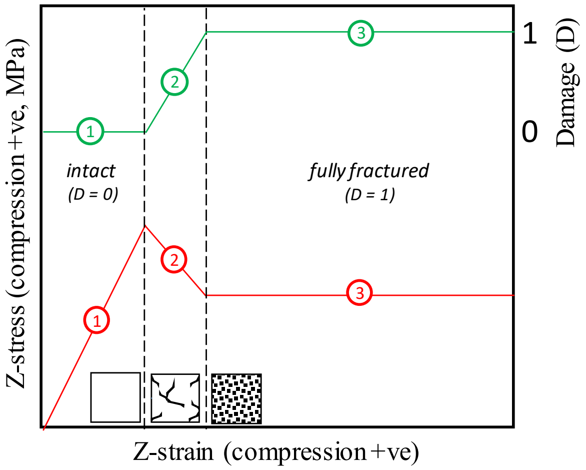

*Figure 7: Schematic of measured stress-strain data used to generate material strength curves (Dannemann, 2011)*

Both the undamaged soda-lime glass samples and the pre-damaged soda-lime glass samples failed differently in the tests Intact samples under low confining pressures (100 – 250 MPa) failed in a brittle-elastic manner, presenting fully elastic behaviour until catastrophic failure. Pre-damaged samples failed in a more complex manner (Figure 7). The samples failed over three phases of response: elastic loading (1) where the sample behaved elastically with a stiffness lower than an undamaged sample; material damage (2) where the maximum strength of the material decreased in a controlled manner until it reached a state of complete comminution, and finally a fully damaged state (3) where the sample maintained a constant strength with increasing strain.

If a material is well behaved, it may be possible to determine pressure-strength dependence with relatively few data points. Johnson, Holmquist et al. (1995), performed a series of coupon level tests and ballistic tests to determine materials parameters of SLG for the JH-2 model (Table 2). These parameters are commonly cited in literature (Zhang, 2015). The tests assessed material strength over a wide range of strains, strain rates and pressures (Johnson & Holmquist, 1995). There were relatively few tests performed, with 11 quasi-static compression and tension tests performed by Johnson and Holmquist (1995), three flyer plate impact tests to determine the equation of state and 2 depth of penetration tests performed by Anderson (1993). The quasi-static tension and compression tests were used to fit the intact material strength (A, N). T was extrapolated by determining when the intact strength curve intersected the pressure axis. The intermediate rate compression tests were used to assess the strain rate coefficient, C. The fractured strength terms (B, m, $SF_{MAX}$) and damage evolution terms (D1 and D2) were iteratively determined using the depth of penetration experiments performed by Anderson (1993).

*Table 2: Summary of Johnson & Holmquist Tests (Adapted from Johnson & Holmquist 1995)*

<table>
<tr><th colspan="9">Compression and Tension Tests</th></tr>
<tr><th>Test Number</th><th>Description</th><th>$\sigma_x$ (GPa)</th><th>$\sigma_y$ (GPa)</th><th>$\sigma_z$ (GPa)</th><th>$\tau$ (GPa)</th><th>$\sigma_{eq}$ (GPa)</th><th>P (GPa)</th><th>$\dot{\varepsilon}$ $(s^{-1})$</th></tr>
<tr><td>1</td><td>Compression</td><td>0</td><td>0</td><td>-1.12</td><td>0</td><td>1.12</td><td>0.37</td><td>0.001</td></tr>
<tr><td>2</td><td>Compression</td><td>0</td><td>0</td><td>-0.92</td><td>0</td><td>0.92</td><td>0.31</td><td>0.001</td></tr>
<tr><td>3</td><td>Compression</td><td>0</td><td>0</td><td>-1.17</td><td>0</td><td>1.17</td><td>0.39</td><td>0.001</td></tr>
<tr><td>4</td><td>Compression</td><td>0</td><td>0</td><td>-0.88</td><td>0</td><td>0.88</td><td>0.29</td><td>0.001</td></tr>
<tr><td>5</td><td>Compression</td><td>0</td><td>0</td><td>-0.149</td><td>0</td><td>1.45</td><td>0.48</td><td>250</td></tr>
<tr><td>6</td><td>Compression</td><td>0</td><td>0</td><td>-1.1</td><td>0</td><td>1.1</td><td>0.37</td><td>250</td></tr>
<tr><td>7</td><td>Compression</td><td>0</td><td>0</td><td>-1.05</td><td>0</td><td>1.05</td><td>0.35</td><td>250</td></tr>
<tr><td>8</td><td>Compression</td><td>0</td><td>0</td><td>-1</td><td>0</td><td>1</td><td>0.33</td><td>250</td></tr>
<tr><td>9</td><td>Tension</td><td>0.16</td><td>-0.48</td><td>0</td><td>0</td><td>0.42</td><td>0.11</td><td>0.001</td></tr>
<tr><td>10</td><td>Tension</td><td>0.17</td><td>-0.52</td><td>0</td><td>0</td><td>0.46</td><td>0.12</td><td>0.001</td></tr>
<tr><td>11</td><td>Tension</td><td>0.12</td><td>-0.35</td><td>0</td><td>0</td><td>0.31</td><td>0.08</td><td>0.001</td></tr>
<tr><th colspan="9">Flyer Plate Tests</th></tr>
<tr><th rowspan="2">Test Number</th><th rowspan="2">Description</th><th colspan="3">HEL</th><th colspan="3">Hugoniot State</th><th></th></tr>
<tr><th>$\sigma_z$ (GPa)</th><th>$\rho$ $(kgm^{-3})$</th><th>$\varepsilon_v$</th><th>$\sigma_z$ (GPa)</th><th>$\rho$ $(kgm^{-3})$</th><th>$\varepsilon_v$</th><th>$\dot{\varepsilon}$ $(s^{-1})$</th></tr>
<tr><td>12</td><td>Flyer Plate</td><td>5.95</td><td>2718</td><td>-0.069</td><td>11.46</td><td>3285</td><td>-0.32</td><td>$10^5$</td></tr>
<tr><td>13</td><td>Flyer Plate</td><td>5.95</td><td>2718</td><td>-0.069</td><td>14.25</td><td>3408</td><td>-0.258</td><td>$10^5$</td></tr>
<tr><td>14</td><td>Flyer Plate</td><td>5.95</td><td>2718</td><td>-0.069</td><td>18.76</td><td>3617</td><td>-0.301</td><td>$10^5$</td></tr>
<tr><th colspan="9">Ballistic Penetration Tests [Anderson et al. (1993)]</th></tr>
<tr><th>Test Number</th><th colspan="3">Description</th><th colspan="2">Impact Velocity (m/s)</th><th colspan="2">Penetration (P, mm)</th><th>P/L</th></tr>
<tr><td>15</td><td colspan="3">Depth of Penetration</td><td colspan="2">1250</td><td colspan="2">129</td><td>1.78</td></tr>
<tr><td>16</td><td colspan="3">Depth of Penetration</td><td colspan="2">1700</td><td colspan="2">172</td><td>2.38</td></tr>
</table>

### 2.3.3 Tensile Strength Tests

The tensile strength of ceramic materials depends on the size and distribution of flaws within the material. Some of these flaws can be introduced during the manufacturing process. Flat glass, typically used in windows, is produced using the float process, where a ribbon of molten glass is floated along a bath of molten tin and allowed to cool (Pilkington, 1969). There are many types of defects that can form in the float process such as bubbles, inclusions, cracks, tin contamination and material inhomogeneity (Liu et al., 2011), three of which can be considered flaws (bubbles, inclusions and cracks). Tin contamination has not shown to have an effect on ballistic performance of glass (Grujicic et al., 2012b), however the effect on tensile strength is not fully quantified. Inhomogeneties in material composition (Wereszczak and Anderson, 2014) and internal stresses (Vivek and Ramesh, 2015) produced in the float process are typically minor. The surface condition of the sample can also play a role in material strength (Holmquist et al., 2017), and poor surface finish control can result in higher variability in results (ASTM, 2018) and this make tensile testing of ceramics difficult. Four tests to determine ceramic tensile strength are often reported in literature: the uniaxial tension test; the three-point bending test, the indentation test and the Brazilian (diametral splitting) test (Figure 8).

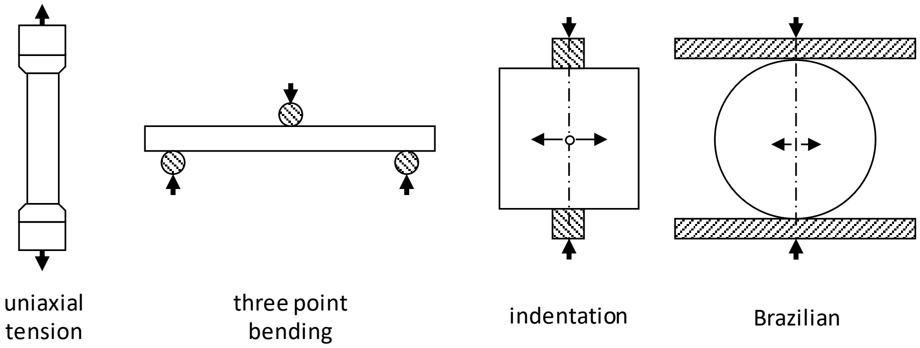

*Figure 8: Various ceramic tensile test methods (loading and sample geometry)*

Uniaxial tensile tests are a staple of mechanical stress-strain testing (Callister, 1991). The key advantage of a uniaxial tension test is that the sample is in a simple stress state (uniaxial tension) and the tensile strength of the material can be determined directly. Tensile test samples are generally cylindrical and taper to a specific gauge length at the centre (ASTM, 2018). However, preparing samples for direct (uniaxial) tension testing of brittle materials, like ceramics, is often challenging since ceramics cannot be machined through conventional methods (Berenbaum et al., 1958). Samples must be gripped using special collets to avoid contact stresses that could result in crack initiation and fracture at the grips (ASTM, 2018). There are also tight restrictions on surface finish, requiring average roughness values of on the submicron level (0.2 – 0.4 μm).

Another test to determine the tensile strength of a material is a three-point bend test (Callister, 1991). In a bend test, a length of ceramic material is bent, placing the surface opposite to the point of loading in tension. The stresses in the sample will not be purely uniaxial tension; however, the stresses at the point of failure can be determined using beam theory (Callister, 1991). The key advantage of the bend test is that is simple to perform and analyze. However, bend tests tend to over predict the tensile strength of the material, sometimes by a factor of two or more depending on the surface condition of the sample (Berenbaum et al., 1958).

The indentation test is an indirect method of measuring the tensile strength of brittle materials (Berenbaum et al., 1958). A square sample is indented (or compressed) between two indenters on opposite sides. The applied indentation load induces a complex stress field in the material and results in a tensile stress at the centre of the sample. However, if the test is improperly performed, contact stresses can cause fracture at the point of indentation, and lead to spurious results. The test methodology is straight forward, but the analysis can become quite complex (Iyengar et al., 1961).

The diametral splitting test (Brazilian test) is another indirect method of measuring the tensile strength of the ceramic (Akazawa, 1943; Caneiro, 1943). A cylindrical sample is loaded along the diameter. The compressive stress induces an internal tensile stress perpendicular to the axis of loading along the diameter of the sample. The tensile stress in the sample is given by the following equation (Andreev, 1991):

$$\sigma_{tensile} = \frac{2P}{\pi DT} \qquad \text{Equation 10}$$

where P is the applied load, D is the diameter of the sample, T is the thickness of the cylinder, and $\sigma_{peak}$ is the peak tensile strength of the sample. The principal stress along the diameter of the sample is of constant magnitude unless very close to the contact interface (Bernbaum et al., 1958), making the analysis of the tests easier than for the indentation test. To ensure repeatable results, faces of the sample should be flat (within 0.25 mm) and edges should be parallel to 0.25° (Ulusay and Hudson, 2007).

### 2.3.4 High Deformation Rate Testing of Ceramic Materials

A defining feature of ballistic impacts is that loading occurs under high strain rates. Although the material directly under the point of impact may experience strain rates in excess of $10^5 – 10^6$ $s^{-1}$, much of the target will experience much lower rates of loading (~ $10^2$ $s^{-1}$) (Sharpe, 2008). Loading greater than $10^2$ $s^{-1}$ can be achieved by the use of a split Hopkinson pressure bar (SHPB) apparatus (Gama et al., 2004). The apparatus consists of three long cylindrical bars (Kolsky, 1949) (Figure 9). A test specimen is placed between the incident and the transmitter bar. In a modern Hopkinson bar setup, strain gauges are located at the middle of each bar to record axial strains during the experiment (Gama et al., 2004). These strains are used to determine the stress-strain response of the specimen. During the test, the striker bar is accelerated and impacts the incident bar, sending a longitudinal stress wave travelling down the length of the incident bar (Figure 9).

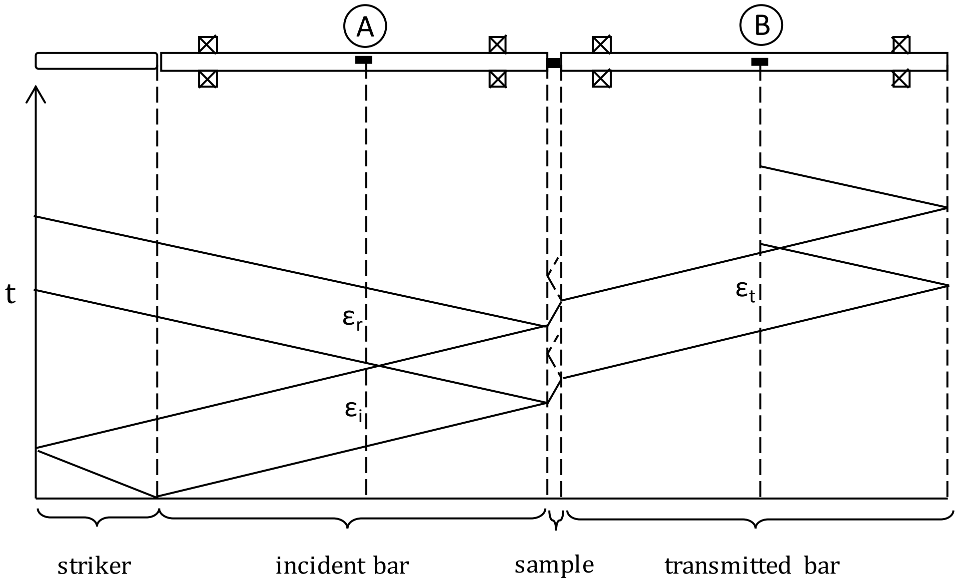

*Figure 9: Split Hopkinson pressure bar setup with wave diagram (Adapted from Sharpe, 2008)*

There are a few requirements to have successfully performed a Hopkinson bar test such as maintaining one-dimensional loading in the bars, maintaining one-dimensional loading in the sample, eliminating spurious wave reflections and reaching dynamic equilibrium in the sample. To maintain one dimensional loading in the bars, all bar lengths should be about 100 times longer than their diameters (Sharpe, 2008). Generally, longitudinal waves in the apparatus disperse as they travel through the bar a phenomenon that is dependent on the frequency of the input and referred to as Pochammer-Chree oscillations (Davies, 1948). However, these effects are negligible in metal bars.

Any friction at the interfaces will apply a radial load to the sample, taking the sample out of uniaxial compression and results in an artificially stiff response (Bertholf et al., 1975). To mitigate these effects, the surfaces of the samples should be well lubricated and the sample diameter should be approximately equal to the length of the sample. Depending on the sample geometry, inertial effects can also induce radial stresses (Gorham, 1989). To ensure uniaxial loading in the sample, friction and inertial loads should be minimized.

The impedance of the sample should be similar to that of the bars to reduce material impedance mismatch that can result in spurious wave reflections during testing resulting in noisy data (Davies, 1948). The sample diameters should be 2-4 times smaller than the bars to produce a geometric impedance mismatch to keep the sample in compression throughout the loading process (Sharpe, 2008). Bars typically range from 7-25 mm in diameter, as larger bars require more energy to launch the striker. Larger sample to bar ratios can be used to increase the impedance mismatch and test harder materials, if required (Sharpe, 2008).

There are a set of equations that can be used to analyze a Hopkinson bar impact using only the measured strains (Sharpe, 2008). These equations are derived from 1D elastic wave mechanics and conservation laws. There are two boundary constraints on the sample, at the incident bar (interface 1) and transmitted bar (interface 2) (Figure 10). As long as the bars remain in contact with the sample, the kinematics of the sample can be determined.

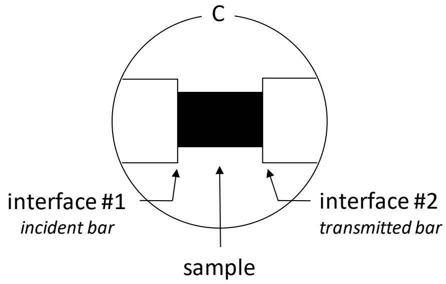

*Figure 10: Hopkinson bar-sample interface detail*

The force generated at each interface can be determined using the strains, elastic properties and cross-sectional areas of the bars:

$$P_1 = E_b A_b (\varepsilon_I + \varepsilon_R) \quad \text{Equation 11}$$

$$P_2 = E_b A_b (\varepsilon_T) \quad \text{Equation 12}$$

If the forces at each end of the bar are equal (P1 = P2) the sample is considered to be in dynamic equilibrium, a condition that is required for a successful Hopkinson bar test (Davies, 1948). Since the sample is loaded from interface 1 and has a finite wave speed, it takes time for the forces to propagate from one end to the other, so there is a non-zero time required for the sample to reach dynamic equilibrium. Force equilibrium is required to ensure the transmitter bar represents the stress in the sample. Previous work by Davies and Hunter (1963) in metals show that it requires at least three wave reflections to achieve dynamic equilibrium in the sample.

It is also possible to modify the Hopkinson bar test such that it can be used to measure tensile strengths. For example, Scapin et al. (2017) have used the Hopkinson bar to load a cylindrical sample along the axis of the sample, much like the diametral compression test configuration, to determine the tensile strength of ceramic materials at high rates with some success (variability experimental data on the order of ± 15%).

### 2.3.5 Direct Impact Tests

Direct impact tests are used to study the phenomena that occur during ballistic impact (Sharpe, 2008). These tests are often simplified cases of real-world ballistic impacts and use simplified geometries, materials and/or boundary conditions. Some ballistic impact tests are performed to study the propagation of damage in a material after an impact. One common test format is to strike one end of a ceramic sample and record damage propagation through the sample using some form of high speed imaging. Some examples include; Taylor impacts of glass rods (Willmott & Radford, 2005), edge on impact of glass tiles (Grujicic et al., 2009) and rod end impacts (Haney & Subhash, 2012). These tests excel at quantifying bulk material damage over time. They use simple boundary conditions and only require one or two material models. The projectile is usually intact after impact, making modelling of these tests straightforward. The key disadvantage of these tests is that they do not present features found in the impact of planar targets (such as the formation of a fracture cone, radial cracks, or concentric cracks). Other experiments focus on the impact of planar targets. These tests often involve a constrained or semi-constrained transparent laminate impacted by a projectile. Some examples for glass include the ballistic testing of multi-layer laminate systems with armour piercing projectiles (Strassburger, 2009), measurement of damage velocities in impacts of transparent armor using a cone point projectile surrogate and ceramic and polycarbonate bi-laminates (Anderson 2014), depth of penetration testing using glass tiles (Hazell, 2010) or the study of failure initiation during the impact of metal spheres on confined ceramic targets (Compton et al, 2013). These tests can produce a wealth damage propagation data as well as information on ballistic performance. However, these tests all incorporate some level of ceramic confinement, making analysis of the tests more difficult compared to an unconfined impact, due to the uncertainty of the boundary conditions An ideal test to study the propagation of damage in ceramics would be simple to model, requiring few material models and straight forward boundary conditions. The test should also be able to reproduce features found in planar impact such as formation of a fracture cone, radial cracks, and concentric cracks as well as comminution near the zone of impact and the propagation of damage and penetration at higher velocities.

There are also ballistic impact tests strictly used to study the ability of ceramics to stop oncoming projectiles. Depth of penetration (DOP) testing is a direct impact experiment often used to compare the ballistic efficiency of ceramic materials (Rosenberg et al., 1988). In the depth of penetration tests, ceramic targets are affixed to a ductile backing material and impacted with a projectile. The resulting depth of penetration into the backing material (r) can be measured and compared to the depth of penetration of a test performed with the backing alone (x) (Figure 11).

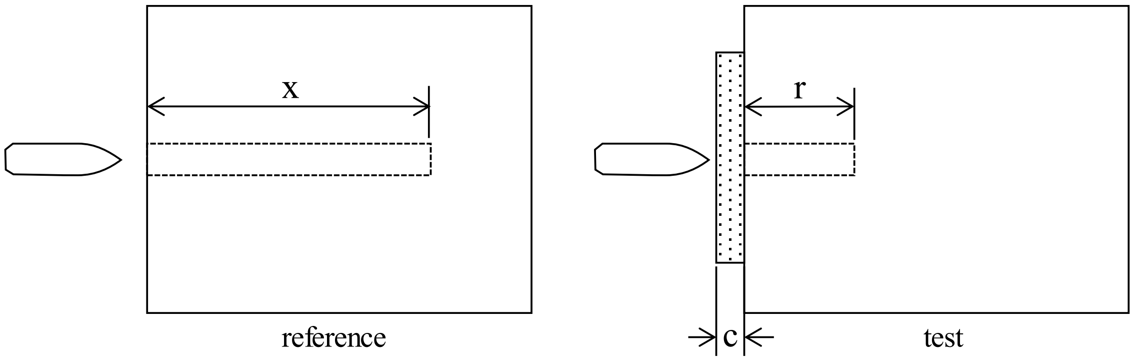

*Figure 11: Depth of penetration test; backing only (left), armour test (right)*

The tests were originally developed by Rosenberg et al. (1988) as a method to suppress tensile stresses that developed when impacting unsupported thin ceramic tiles. This is important as the full strength of a ceramic cannot be fully quantified without some level of confinement (Walley, 2010). This simple test is well established in literature and often used to characterize ceramic materials under ballistic loading conditions (Walley, 2010).

The depth of penetration test is a relatively low cost method to establish a performance criterion for ceramic, when compared to $v_{50}$ testing, a common test method for armour systems (Hazell, 2010). It was empirically shown that the ballistic efficiency of a tile was independent of the thickness, except for very thin tiles (less than ½ of the projectile diameter) (Rosenberg et al., 1988). Using the ballistic efficiency, direct comparisons between ceramic materials can be made for a given backing material.

## 2.4 Numerical Modelling of Ceramics under Ballistic Impact Conditions

Numerical models can assist in the development and optimization of transparent armour by reducing the amount of ballistic testing required in the design process (Templeton, 2001). Ballistic models are solved using computer codes and specific numerical methods to approximate solutions to analytical problems (Hamming, 1986). There are 5 steps in a numerical analysis (Belytschko, 2006):

1. Development of a model
2. Formulation of the governing equations
3. Discretization of the equations
4. Solution of the equations
5. Interpretation of the results

The analyst is responsible for the development of the model (constitutive model, geometry, placement of boundary conditions, etc.) and interpreting the results (steps 1 & 5). Although the solver is responsible for the discretization of equations, the analyst has some options available for how the problem should be discretized.

### 2.4.1 Numerical Modeling and Discretization Methods

To solve analytical problems through numerical methods, the problem must be discretized (Belytschko, 2006). A continuum body contains an infinite number of points, and to solve for the field variable at an infinite number of points would be computationally impossible. Discretization is the process where a continuous body is subdivided into a discrete or finite set of points.

**Finite element method using Hexahedral Solid Elements**

An eight node hexahedral solid element (or brick element or hex element) is a common method of discretizing a three dimensional solid. Hexahedral elements were developed in the mid-70s (Wilkins, 1974) to study solid mechanics and gas dynamics problems in three dimensions and are often used in finite element analysis. The finite element method is commonly used in the modelling of ballistic impacts of glass (Grujicic et al., 2011; Zhang et al., 2015; Binar et al., 2018; Dorogoy et al., 2019). The adaptability and widespread use of the finite element method make it a prime candidate for modelling ballistic impact.

However, the finite element method is not well suited to high deformations that may occur in ballistic impact problems. FEM uses a fixed connectivity between nodes, and large deformations can result in mesh entanglement (Johnson, 2011; Kupchella, 2015) and element inversion. FEM also uses shape functions to interpolate for values between nodes that become less accurate with increasing levels of deformation (Salagame & Belegundu, 1994). Simulation time steps (and therefore simulation runtimes) are directly related to the size of elements (Hallquist, 2006), so excessive deformation leading to small element edge lengths can also result in prohibitively long runtimes. To overcome these limitations and to incorporate material failure, many ballistic models employ element erosion techniques. Element erosion is a method used to simulate material failure in finite element models (Kuna, 2013). Element erosion is also desirable when elements become highly distorted, resulting in prolonged simulation runtimes (Cronin et al., 2003). When a specified threshold is exceeded (e.g. exceeding a critical plastic strain), the element is removed from the calculation. However, this process is element-size dependent and requires mesh regularization for a specific element size (Schwer, 2010). Lower erosion strains (or premature removal of elements) can lead to erroneous results and increased mesh sensitivity (Cronin et al., 2003).

### Smooth Particle Hydrodynamics

Smooth Particle Hydrodynamics (SPH) is a mesh-free discretization method. Smooth Particle Hydrodynamics was developed in the mid-70s by both Lucy (1977), and Gingold & Monaghan (1977) to study astrophysics problems. SPH has since been extended to model hydrodynamic impacts (Libersky et al., 1997), where pressures exceed the material strength and the material begins to flow, typically occurring above 3 km/s (Zukas, 2004). The interpolation and connectivity between particles are determined at every time step with no fixed connectivity between particles (Hallquist, 2006). Because of this, particles are free to move around without risk of entanglement. This alleviates one of the major issues finite elements have with large deformation problems. Due to the bounded smoothing length (and therefore calculation time step), SPH does not suffer as much with respect to runtimes by large deformations (Hallquist, 2006). This makes SPH ideal for problems with large material deformations like those seen in ballistic impact. However, SPH is susceptible to tensile instabilities, a numerical artifact that may result in artificial clumping or fragmentation of particles (Monaghan, 1999). SPH is still in development in some explicit dynamics codes such as LS-DYNA, and therefore features like the handling of contact and how symmetry planes are applied in simulation (LSTC, 2017) may not currently be as numerically robust as FEM.

### Element-Free Galerkin

The Element-Free Galerkin (EFG) method is a discretization method where the interpolation of the field variable is performed using a moving least squares method over a finite domain. EFG was first proposed by Belytschko et al. (1994) as an alternative to the standard finite element approach with the intent of overcoming some of the limitations that a finite element mesh produced, like the need to mesh geometry (a time intensive process). Due to the use of a least squares fit to interpolate, EFG is able to capture very high stress gradients (Belytschko et al., 1994), making it ideal for ballistic impact problems. The ability to capture very large stress gradients also allows EFG to converge much faster than a standard finite element model (Belytschko et al., 1994). It can also be coded such that the interpolation domain can account for cracks and exclude nodes from calculation, allowing for better handling of discontinuities (Belytschko et al., 1994). Due to the mesh-free nature of EFG, it can undergo large deformations often seen in ballistic impact problems without numerical instabilities. However, this approach has not seen widespread use in ballistic impact modelling due to the fact it is a fairly new method (proposed in 1994) and is relatively resource intensive with respect to computation time and memory required to perform an analysis (Hu et al., 2016).

### 2.4.2 Discretization Error and Model Assessment

Discretization of a continuous body (regardless of the method) is an approximation, and this approximation can result in discretization error (Hutton, 2004). Discretization error is a source of numerical error that is the result of expressing a continuous problem as a discrete one. Element size has a significant effect on the ability of a computational model to predict projectile kinematics (Kaufmann 2004; Schwer 2009; Dorogoy et al., 2011). These errors are present in all numerical analysis, and their effects can be estimated using a grid convergence index.

The grid convergence index (GCI) was first proposed by Roache (1994) as a standardized method to quantify uncertainty in models and is based on the Richardson extrapolation. The method requires at least two levels of mesh refinement, usually denoted by $h_1$ (fine mesh) and $h_2$ (medium mesh), where h is some characteristic length associated with the mesh. A parameter of interest, f, is computed using both the fine mesh ($f_1$) and medium mesh ($f_2$). The converged solution can be approximated by the following:

$$f_{exact} \approx f_1 + \frac{(f_1 - f_2)}{(r^p - 1)}$$

where r is the grid refinement ratio, r ($h_2 / h_1$). If a third level of refinement (coarse mesh) with mesh length $h_3$ and solution $f_3$ is calculated, the observed rate of convergence (p) can be determined by using the following equation:

$$p = \frac{\ln\left(\frac{f_3 - f_2}{f_2 - f_1}\right)}{\ln(r)}$$

Note that this equation requires the same grid refinement ratio (r) for all three meshes. Small grid refinement ratios (like r = 1.1) result in large errors in the estimate (on the order of 15%), so larger values are recommended (typically 2.0) (Roache, 1994). The GCI is an estimate of error using the Richardson extrapolation and is an indication of how close the calculated solution is to the estimated converged solution (Slater, 2008). A GCI can be calculated using the parameter of interest from the fine and medium meshes ($GCI_{12}$) and the medium and coarse meshes ($GCI_{23}$):

$$GCI = \frac{|\varepsilon|}{(r^p - 1)}, \qquad \varepsilon_{12} = \frac{f_2 - f_1}{f_1}, \qquad \varepsilon_{23} = \frac{f_3 - f_2}{f_2}$$

where $\varepsilon_{12}$ and $\varepsilon_{23}$ are the respective error calculations for $GCI_{12}$ and $GCI_{23}$. If the solution is in the range of convergence, the error should converge such that:

$$GCI_{23} = r^p \, GCI_{12}$$

Using these tools, one can estimate the error associated with the discretization of a continuous problem. However, discretization error is only one source of modelling error. Unfortunately, not all sources of modelling error can be quantified as directly as discretization error. To have confidence in a numerical model, the model must be assessed against experimental data. The primary goal of assessing a model is to build confidence in the ability of the model to predict real world phenomena (ASME, 2006) through verification and validation. Verification is the process that is used to establish that a computer model interpretation of a mathematical model is correct. Validation confirms than the mathematical model used appropriately captures the phenomena required to accurately predict a system to the level of detail that is required (Figure 12).

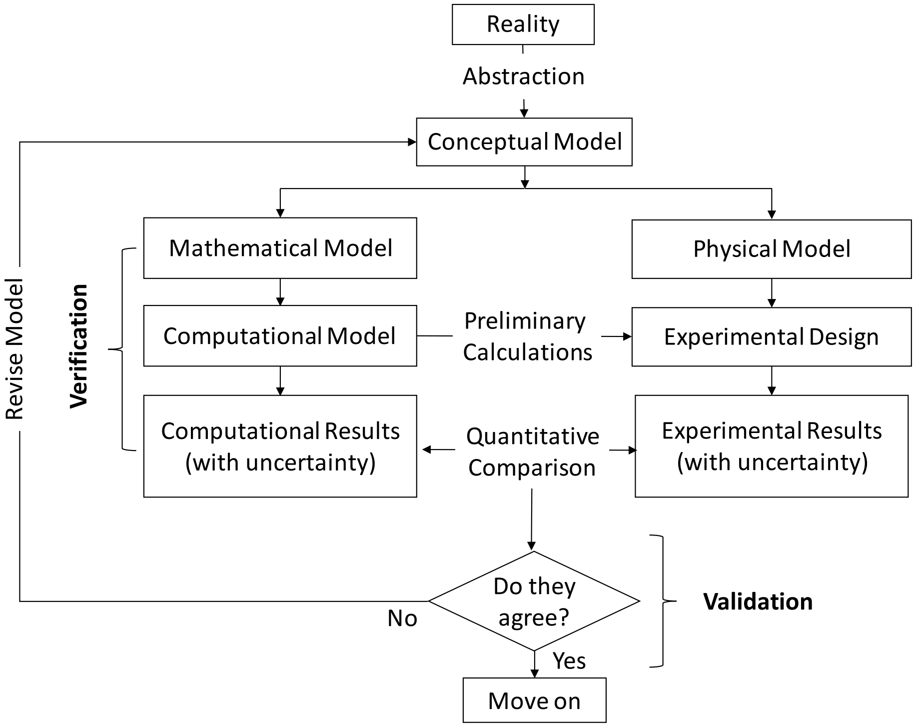

*Figure 12: Model design cycle as proposed by ASME V&V 10 (abridged).*

# 3. Experimental Methods

To assist in the development and validation of a ballistic model of soda-lime glass, three experimental tests were conducted. First, a sphere on glass tile ballistic impact test was performed to characterize the dynamic failure in planar targets of soda-lime glass over a range of impact velocities. Second, a dynamic Brazilian test was conducted to measure the tensile strength of the soda lime glass under high rates of loading, a parameter that is not well defined in literature (van der Velde, 2015). Finally, a depth of penetration test was used to assess the ballistic performance (ability to resist perforation by an oncoming projectile) of soda-lime glass.

## 3.1 Sphere on Glass Tile Tests

The sphere on glass tile ballistic tests were performed at DRDC Valcartier. Hardened steel ball bearings (projectiles), 6.35 mm (¼”) in diameter were contained in a sabot and accelerated using a fixed barrel, universal receiver setup (Figure 13). The targets were square, untreated, soda-lime glass tiles (Starphire, PPG Industries, Inc., Pittsburgh PA) with dimensions of 101.6 x 101.6 x 12 mm (30.24 kg/m$^2$ areal density). A tile thickness of 12 mm was used because it was on the same order of magnitude as the diameter of many projectiles of interest, and similar to the thickness of a single layer of glass that may be used in fielded armor systems (Weinhold, 2013). The tiles were placed on a test bench perpendicular to the projectile path, and a small amount of ballistic clay was applied to position the tile and ensure the tiles were level while not interfering with the response of the tile. Three test repeats were performed at each impact velocity: 100 m/s, 200 m/s, 300 m/s, 500 m/s, 550 m/s, 650 m/s, and 800 m/s (Table 3).

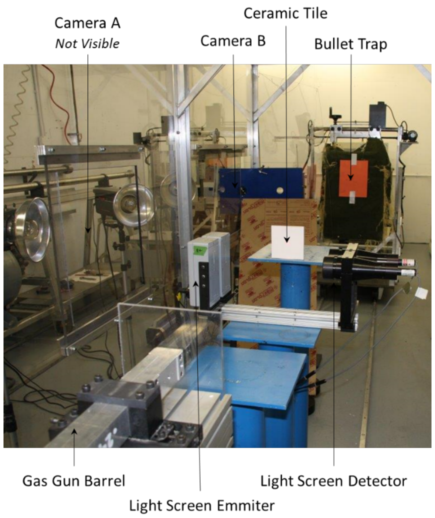

*Figure 13: Sphere on glass experimental test setup*

Table 3: Sphere on glass experimental test matrix

| Target | Sample Thickness *[mm]* | Areal Density *[kg/m$^2$]* | Projectile | Impact Velocity *[m/s]* | Test Repeats |
|---|---|---|---|---|---|
| Starphire Non-treated | 12 | 30.24 | 6.35mm Steel BB | 100 | 3 |
| | | | | 200 | 3 |
| | | | | 300 | 3 |
| | | | | 500 | 3 |
| | | | | 550 | 3 |
| | | | | 600 | 3 |
| | | | | 800 | 3 |

The impacts were recorded by two high speed cameras that were triggered by a light screen (Figure 14). The primary camera (Camera A, Fastcam SA-Z Model 2100K-M-8GB, IMAGICA Robot Holdings, Inc. (Photron), Tokyo, Japan) was set to a frame rate of 35 000 frames per second with a resolution of 1024x576 pixels to track the projectile. Camera A was placed orthogonal to the line of impact (Figure 14). The second camera (Camera B, Hypervison, Shimadzu Corp, Kyoto, Japan) was used to record damage propagation in the glass from a rear view of the target.

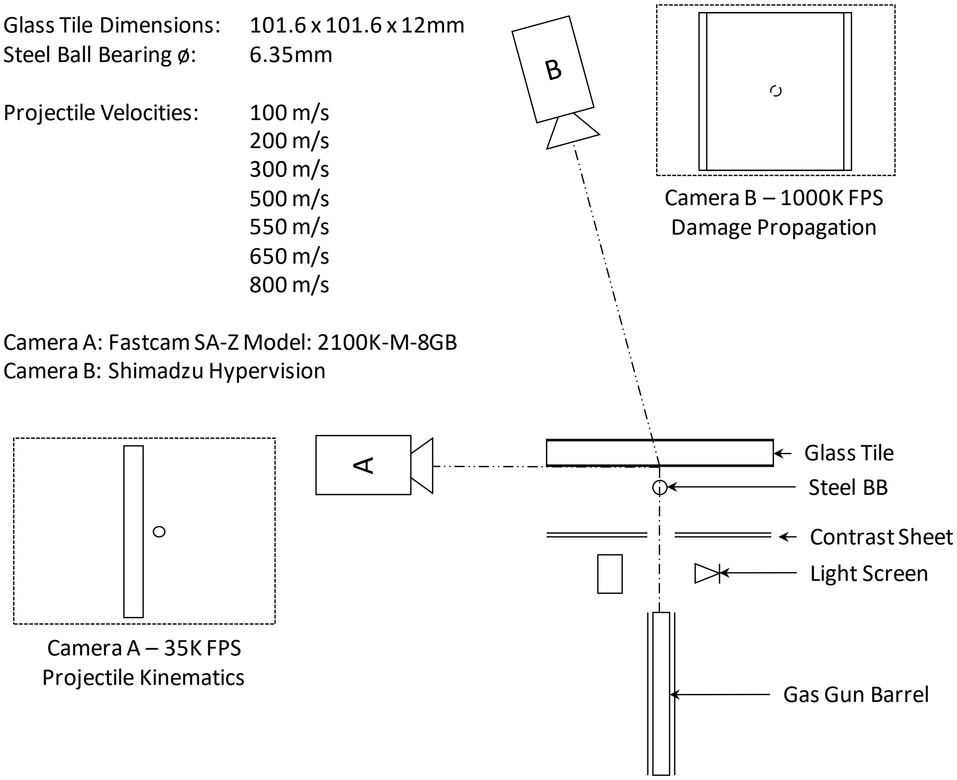

*Figure 14: A schematic view of the sphere on glass tile experimental setup*

Camera B was placed behind the target with respect to the point of impact and at a slight angle to allow for better visibility (the bullet trap was placed directly behind the target) and to prevent damage to the camera. Camera B was set to record with a frame rate of 1 000 000 frames per second and an effective resolution of 240 x 240 pixels (cropped from 400 x 250). Kinematic data, including projectile velocities and damage propagation velocities were obtained using a video analysis tool (Tracker, Open Source Physics).

### 3.2.1 Projectile Kinematics

To determine the projectile velocity, a single point on the sphere was tracked (Camera A, Figure 15). The diameter of the sphere and thickness of the tile were used for length calibration. This calibration was further verified by comparing the tracked projectile velocities with measured velocities from the light screens, all of which were in good agreement.

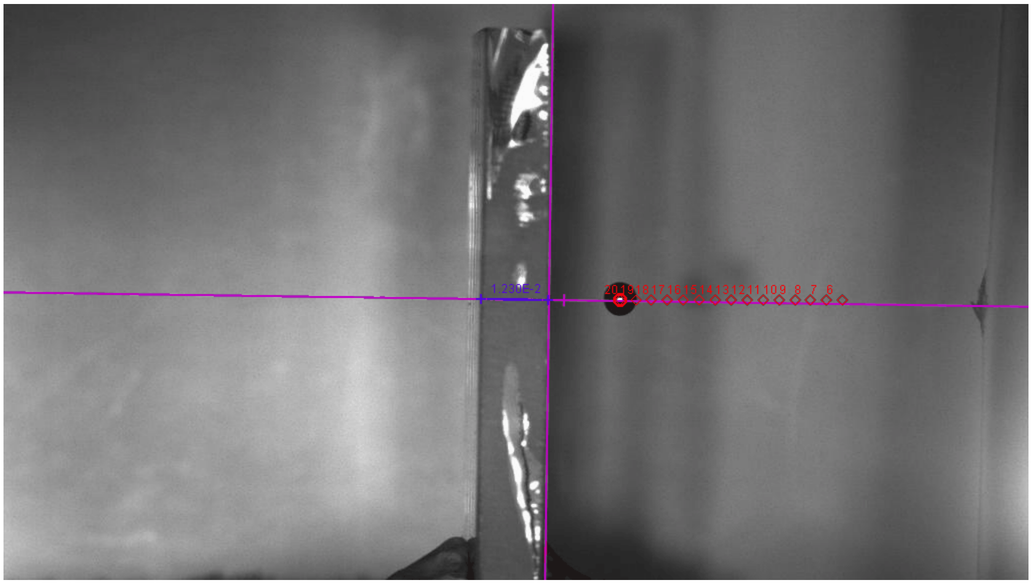

*Figure 15: Tracking the position of the projectile over time using Tracker (100 m/s impact, Camera A).*

The derivative of the displacement versus time data was taken to determine the projectile velocity. The initial and residual velocities were determined by finding the average velocity before and after the impact had occurred (Figure 16).

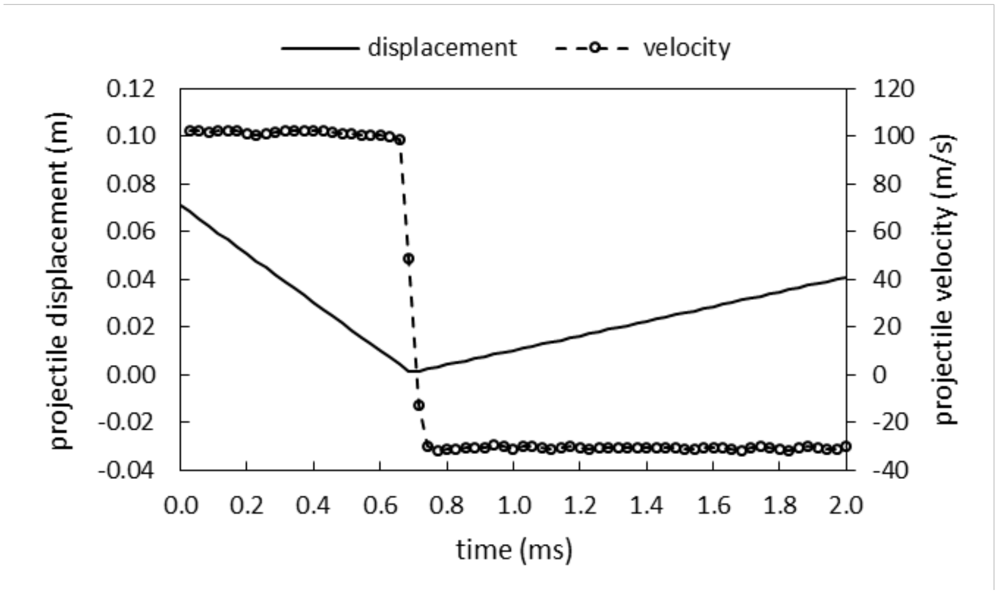

*Figure 16: Exemplar displacement-time data for initial and final projectile velocity (100 m/s impact velocity)*

### 3.2.2 Features of Impact

Six features of impact were consistently observed in the tests, categorized as: discrete fracture (fracture cone, radial cracks, concentric cracks, edge cracks); material comminution; and perforation of the tile. Camera B was used to track damage in the tile over time including discrete cracks and comminution. The damage features were measured at 250 µs after impact, well after the damage front had stopped progressing (50 µs after impact). This study did not consider the damage accumulated during gross motion of the tile, a process that took place later in time.

### 3.2.3 Damage Front Tracking

Damage propagation was tracked using video from Camera B (Figure 17). To facilitate proper visualization of damage in the tile, a contrast sheet (white paper) was placed between the gas gun and the target. A rectangular window was cut in the contrast sheet to allow the projectile to pass without tearing the sheet and obscuring the view (Figure 17). For the purposes of this study, the damage front was defined as the edge of damaged material (the boundary between visibly damaged and undamaged material, Figure 17) that originated from the point of impact. The damage front was tracked in the one direction (vertical) since this provided the best contrast. The damage front was confirmed to be approximately circular by tracking damage at 45$^0$ intervals for a representative case (100 m/s), with a variation of 3-7% of the radius (standard deviation in the radius varying from 1.6 mm - 3.4 mm over the impact event). Thus, it was deemed acceptable to measure the damage front in the vertical direction for the rest of the experiments.

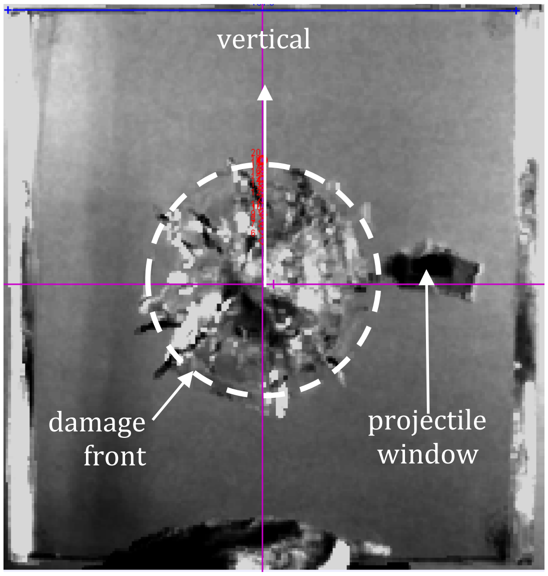

*Figure 17: Tracking the position (red circles) of the damage front over time (100 m/s impact, Camera B)*

## 3.2 Split Hopkinson Pressure Bar Tests

The split Hopkinson pressure bar (SHPB) tests were performed at the University of Waterloo (Figure 18). The apparatus used three bars: a striker bar, an incident bar and a transmitted bar (Figure 19).

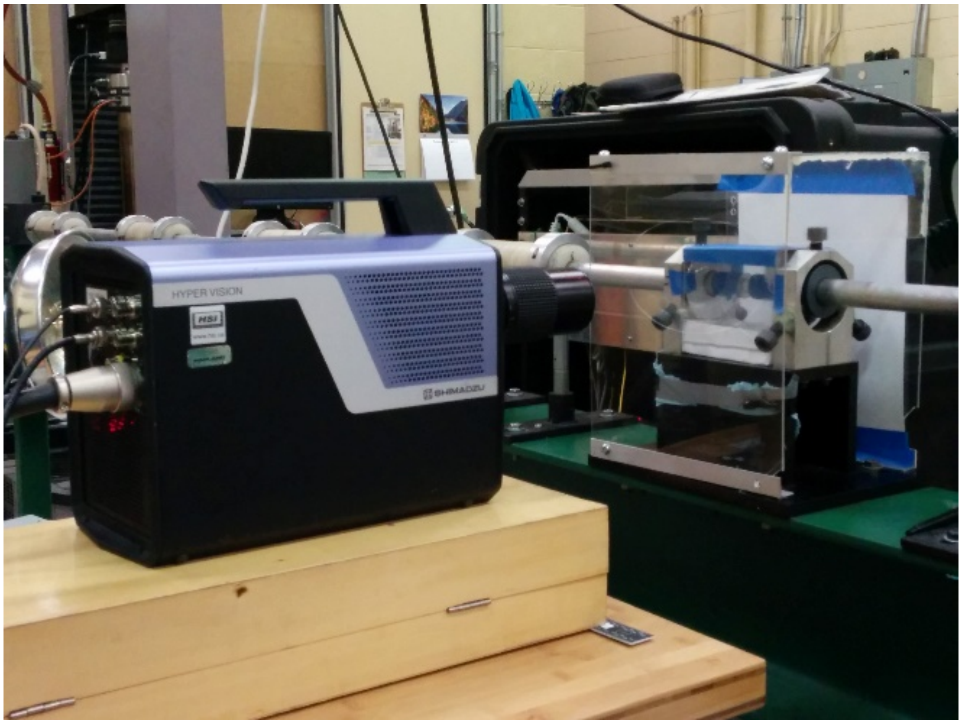

*Figure 18: Split Hopkinson pressure bar Apparatus experimental setup*

Strain gauges (1000 ohm) were applied to both the incident and transmitted bar at the midpoint of their spans (Figure 19). The gauges were connected to a signal amplifier (Vishay 2210B Conditioning Amplifier), and data was recorded using a data acquisition system (DAC) (National Instruments BNC-2110). Data was collected at 1 MHz and was unfiltered. Data collection was triggered using the rising edge of the incident bar strain gauge signal.

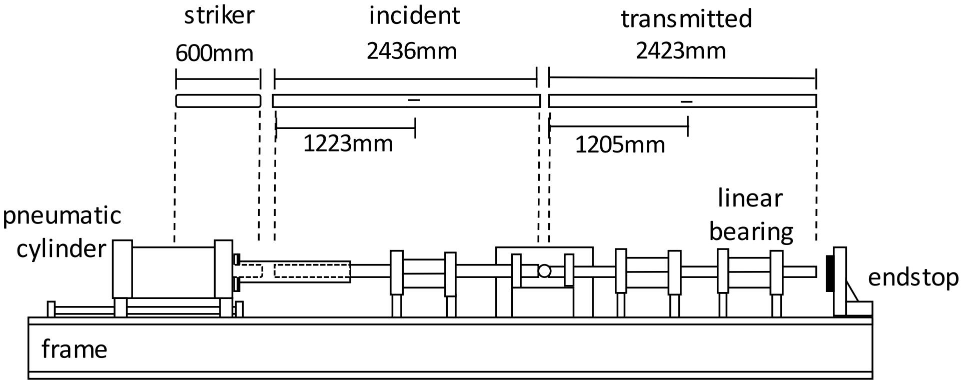

*Figure 19: A schematic view of the split Hopkinson pressure bar apparatus*

Two tests were performed: a diametral compression test (Brazilian), where a cylindrical sample was placed perpendicular to the axis of the bar, and a direct compression test, where a cylindrical sample was placed parallel to the axis of the bar (Table 4, Figure 20). Consumable shims, nominally 4 mm in thickness and 25.4 mm (1") in diameter, and made of aluminum (6061-T6) were placed between the bars and the glass samples to prevent marring of the bar ends during testing. The shims were not fixed in any way; however, a light coating of petroleum jelly (Vaseline) ensured the shims remained in place for the duration of the tests. For the diametral compression tests, aluminum bars (6061-T6) were used as to match the impedance of the soda-lime glass samples and reduce spurious wave reflections. For the direct compression samples, aluminium bars did not provide enough force to initiate failure in the samples, so maraging steel (Vascomax C350) bars were used in place of aluminum.

*Table 4: Test matrix for Hopkinson bar testing*

| Test Series | Sample Geometry | Material | Striker | Pressure | Test Repeats |
|---|---|---|---|---|---|
| Dynamic Brazilian | Ø 13 mm<br>T 12.54mm | SLSG | 600 mm Aluminum | 25 psi | 15 |
| Direct Compression | Ø 13 mm<br>T 12.54mm | | 600 mm Maraging Steel | 20 psi | 5 |

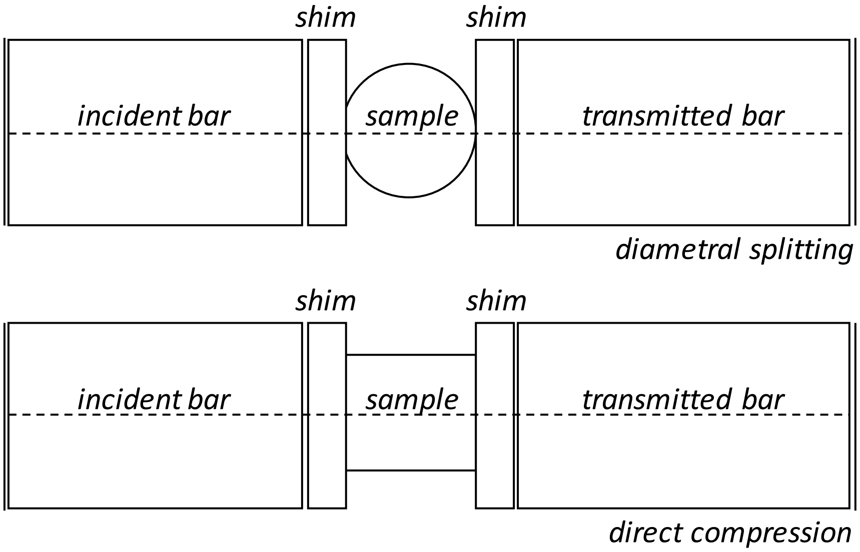

*Figure 20: A schematic view of the diametral splitting test (top) and direct compression test (bottom) performed on the SHPB apparatus*

The test samples were made of soda-lime glass and were nominally 13 mm in diameter and 12.46 mm thick. They were cut from 12 mm sheets of glass material to ensure that the samples were representative of the ceramic tiles used in other rounds of testing. All glass samples were provided by Prelco. The SLG samples had a ridge about the circumference of the sample and had to be ground flat to produce consistent results (Figure 21).

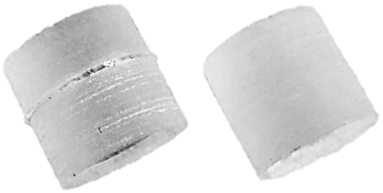

*Figure 21: SLG samples pre (left) and post (right) grinding.*

Although the grinding process removed the ridge on the samples, there was still a minor variation in diameter of the samples. To characterize the variation in diameter, two measurements were taken along the diameter of the sample at 90° to one another. Most samples had a variation in diameter of less than 50 µm; however, some samples had a minor variation (50 µm – 200 µm) or major variation (> 200 µm) in diameter (Figure 22). All samples were tested regardless the degree of diameter variation.

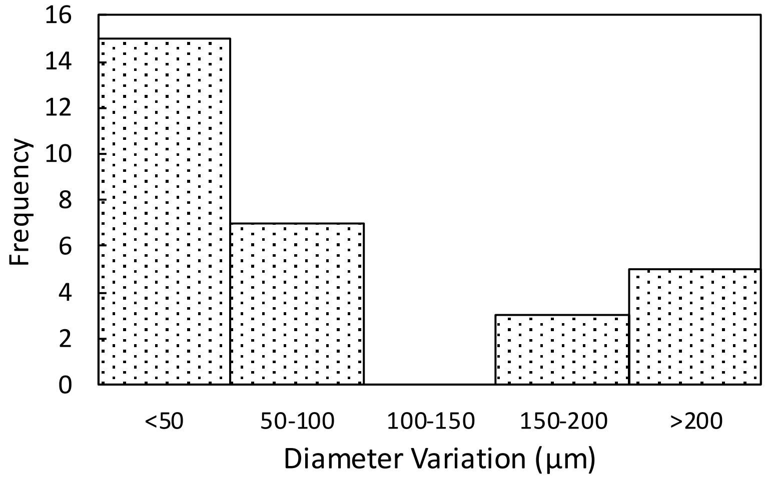

*Figure 22: Variation in diameter in cylindrical SLG SHPB test samples*

All tests were recorded with a high speed video camera (Shimadzu Hypervision HPV-X), at one million frames per second and a macro lens. The camera was triggered using the incident bar strain gauge signal, fed through an amplifier/delay generator designed in-house. A delay generator was required, since the signal was generated at the middle of the incident bar and the pressure wave would take an additional 250 µs to reach the sample (Figure 23).

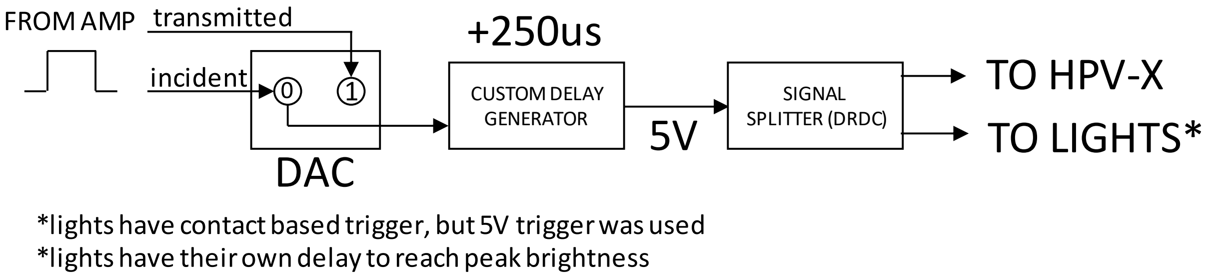

*Figure 23: Block diagram of Hopkinson bar wiring setup*

The Hopkinson bar was covered with two acrylic shields. The first was a containment shield to contain the glass debris resulting from the impact test and fracture of the sample, to facilitate easy clean up and sample collection. The second shield was a safety shield in case any fragments managed to escape the first shield. A sheet of white paper was placed behind the second shield to help with camera focusing and reflect light from the flash bulbs.

## 3.3 Depth of Penetration Tests

The depth of penetration (DOP) tests were performed in the ballistics lab at DRDC Valcartier. Twelve configurations were tested using various thicknesses of glass and projectile velocities (Table 5). Soda-lime glass tiles (Starphire, PPG Industries, Inc., Pittsburgh PA) with dimensions of 101.6 x 101.6 mm and varying thicknesses (5 mm, 9.5 mm, 12 mm) were laminated to polycarbonate cylinders, 6" in diameter and 12" in length. Some tested were undertaken with the only polycarbonate backing to assess the penetration of the projectile into the backing alone as a reference for the glass ballistic tests. A flat viewport, 2" in width was machined on one side of the cylinder to facilitate viewing of the projectile as it penetrated the backing material The tests were performed at three target test velocities (500 m/s, 750 m/s, 930 m/s) using a common small calibre armour piercing projectile (AP-M2). The projectile had three components, a gilding metal jacket (copper), point filler (lead) and a steel core (Figure 24) with a total weight of 10.8 g (Moynihan et al., 2000).

*Table 5: Test matrix for depth of penetration tests*

| Test Series | Sample Thickness *[mm]* | Areal Density *[kg/m$^2$]* | Projectile | Impact Velocity *[m/s]* | Test Repeats |
|---|---|---|---|---|---|
| Backing Only (No Glass) | 0 | 0 | APM2 | 500 | 3 |
| | | | | 750 | 3 |
| | | | | 930 | 3 |
| 5 mm SLSG | 5 | 12.6 | | 500 | 3 |
| | | | | 750 | 3 |
| | | | | 1000 | 3 |
| 9.5 mm SLSG | 9.5 | 23.9 | | 500 | 3 |
| | | | | 750 | 3 |
| | | | | 1000 | 3 |
| 12 mm SLSG | 12 | 30.2 | | 500 | 3 |
| | | | | 750 | 3 |
| | | | | 1000 | 3 |

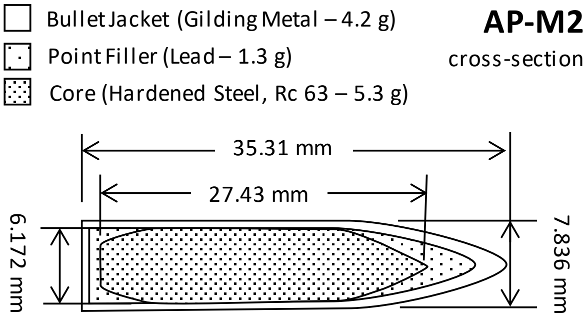

*Figure 24: A cross-section of the AP-M2 projectile (adapted from Moynihan et al.,2000)*

The tests were recorded with two high speed cameras (A, B in Figure 25), in a similar arrangement to the cameras used to record the sphere on glass tests (see section 3.1). The primary camera (Camera A) was used to track the projectile penetration through the polycarbonate backing material, and recorded images at 50,000 frames per second. Projectile displacement throughout the impact was tracked using the video analysis tool, (Tracker, Open Source Physics). The secondary camera (Camera B) was used to track the damage propagation of the tile by viewing a mirror placed in front of the target, and recorded images at 1 million frames per second.

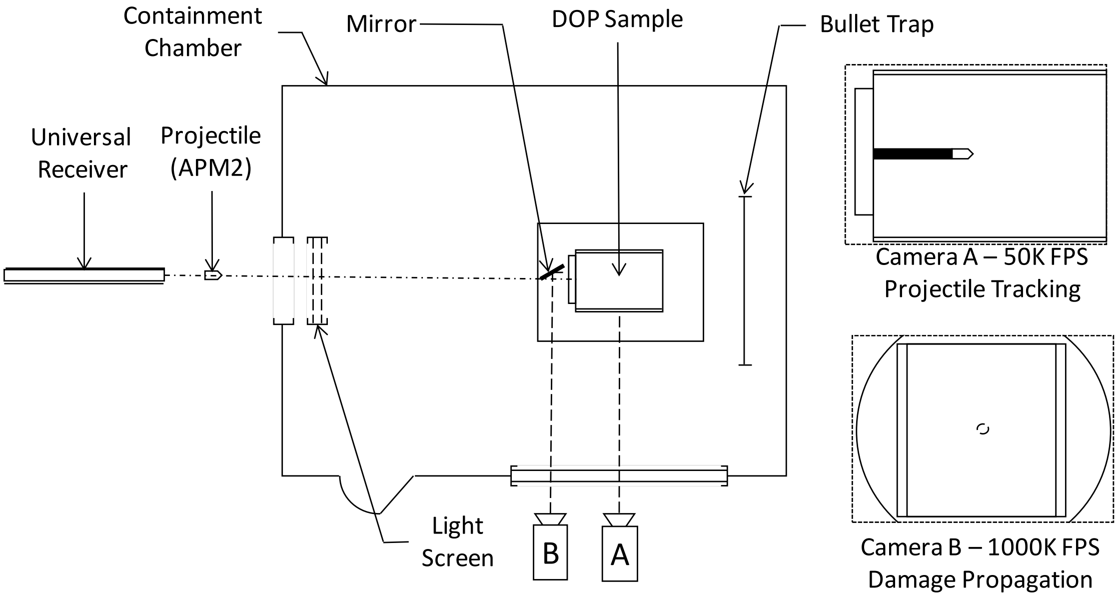

*Figure 25: A schematic view of the depth of penetration test*

Following ballistic testing, the samples were shipped to the University of Waterloo, where a post-impact analysis was performed. This included imaging the samples. Two orthogonal views perpendicular to the axis of the cylinders were taken to capture the position of the projectile. A third image of the top of the cylinders were also taken to assess the final damage sustained by the glass tiles (Figure 26).

*Figure 26: Post-test imaging of depth of penetration samples (top: two views of the same impact test demonstrating the projectile path; bottom: view of the impacted glass surface)*

# 4. Experimental Results and Discussion

## 4.1 Sphere on Glass Tile Results

The initial and residual projectile velocities of the sphere on tile tests demonstrated good repeatability (Table 6, Figure 27). The impact velocities varied at most ± 5% (at 550 m/s), while the residual velocities demonstrated higher variation. The tests captured both perforating and non-perforating events (Figure 28).For the non-perforating and perforating impacts, the residual projectile velocity magnitudes were within 10%, while the residual velocities in the vicinity of the target perforation velocity (300 - 550 m/s) showed higher variability (up to 400% at 550 m/s).

*Table 6: Initial and residual projectile velocities*

± = 1 standard deviation (COV in parentheses where applicable)

| Experimental Data | | Aggregate Results | | |
|---|---|---|---|---|
| Initial Velocity *(m/s)* | Residual Velocity** *(m/s)* | Test Velocity *(m/s)* | Initial Velocity *(m/s)* | Residual Velocity** *(m/s)* |
| 103 | -31 | 100 | 103±* | -31 |
| -* | -* | | | |
| -* | -* | | | |
| 200 | -22 | 200 | 199±1<br>(0.01) | -20±2<br>(0.10) |
| 199 | -18 | | | |
| 198 | -21 | | | |
| 299 | -31 | 300 | 300±2<br>(0.01) | -27±6<br>(0.22) |
| 300 | -30 | | | |
| 302 | -20 | | | |
| 497 | -15 | 500 | 501±4<br>(0.01) | -10±5<br>(0.50) |
| 504 | -7 | | | |
| 503 | -8 | | | |
| 567 | -* | 550 | 552±24<br>(0.05) | 2±8<br>(4.00) |
| 565 | -4 | | | |
| 523 | 7 | | | |
| 648 | 60 | 650 | 652±6<br>(0.01) | 62±3<br>(0.05) |
| 649 | 60 | | | |
| 658 | 66 | | | |
| 805 | 129 | 800 | 805±* | 129 |
| -* | -* | | | |
| -* | -* | | | |

* Projectile not visible in high speed video before or after impact

** Positive residual velocity indicates perforation

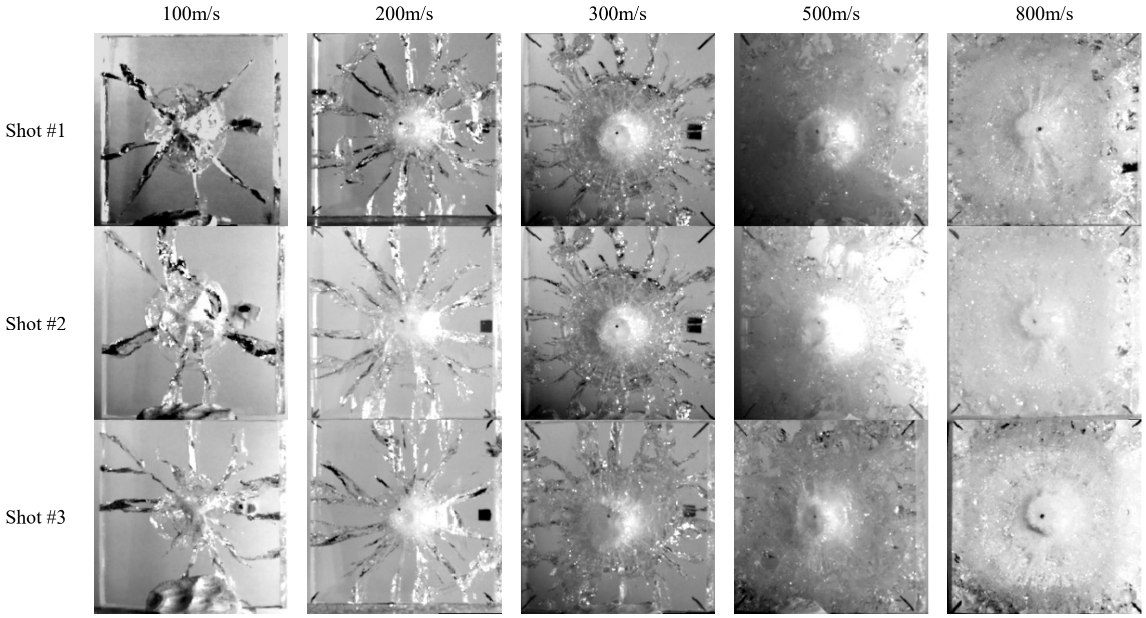

*Figure 27: Reverse side of tiles 50 µs after impact*

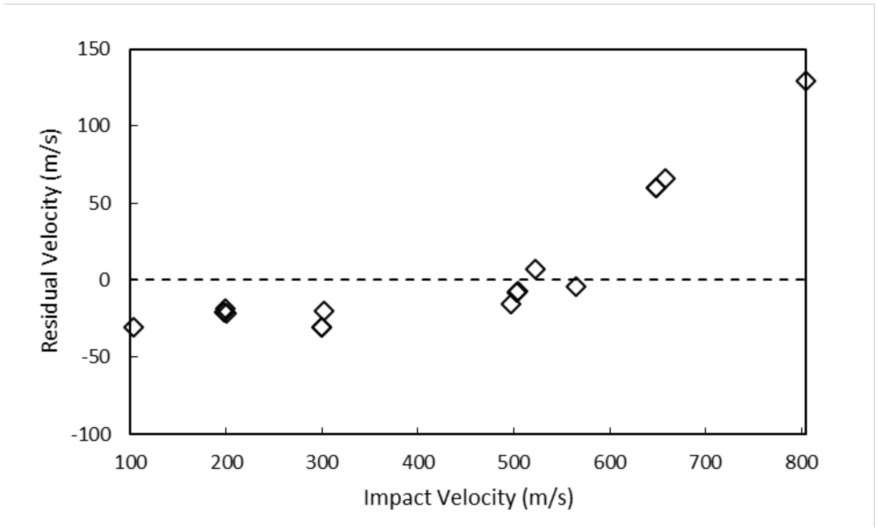

*Figure 28: Residual velocity of projectiles versus impact velocity (+ = perforation, - = rebound)*

*Table 7: Fracture features present at various impact velocities*

| Nominal Test Velocity | 100 m/s | 200 m/s | 300 m/s | 500 m/s | 550 m/s | 650 m/s | 800 m/s |
|---|---|---|---|---|---|---|---|
| Fracture Cone | Yes | Yes | No | No | No | No | No |
| Radial Cracks | Yes | Yes | Yes | Partial | No | No | No |
| Concentric Cracks | No | Partial | Yes | Yes | No | No | No |
| Comminution | Yes | Yes | Yes | Yes | Yes | Yes | Yes |
| Edge Cracks | No | No | Yes | Yes | No | No | No |
| Perforation | No | No | No | No | Yes | Yes | Yes |

A variety of planar impact features were observed in the sphere on glass tile tests (Table 7) demonstrating a transition from discrete cracks to widespread comminution with increasing impact velocity. Edge cracks were only identified at velocities in the transition from non-perforation to perforation. Many damage features such as the number of radial cracks and the radii of damage were consistent within test runs (Table 8). At a specific velocity, the damage progression was consistent between the three test repeats throughout the perforation process, demonstrating the repeatability of the test methodology. Not all planar impact features were present at every impact velocity. Different features of planar impact dominated at low (100 m/s), medium (500 m/s) and high (800 m/s) speed impacts (Figure 29).

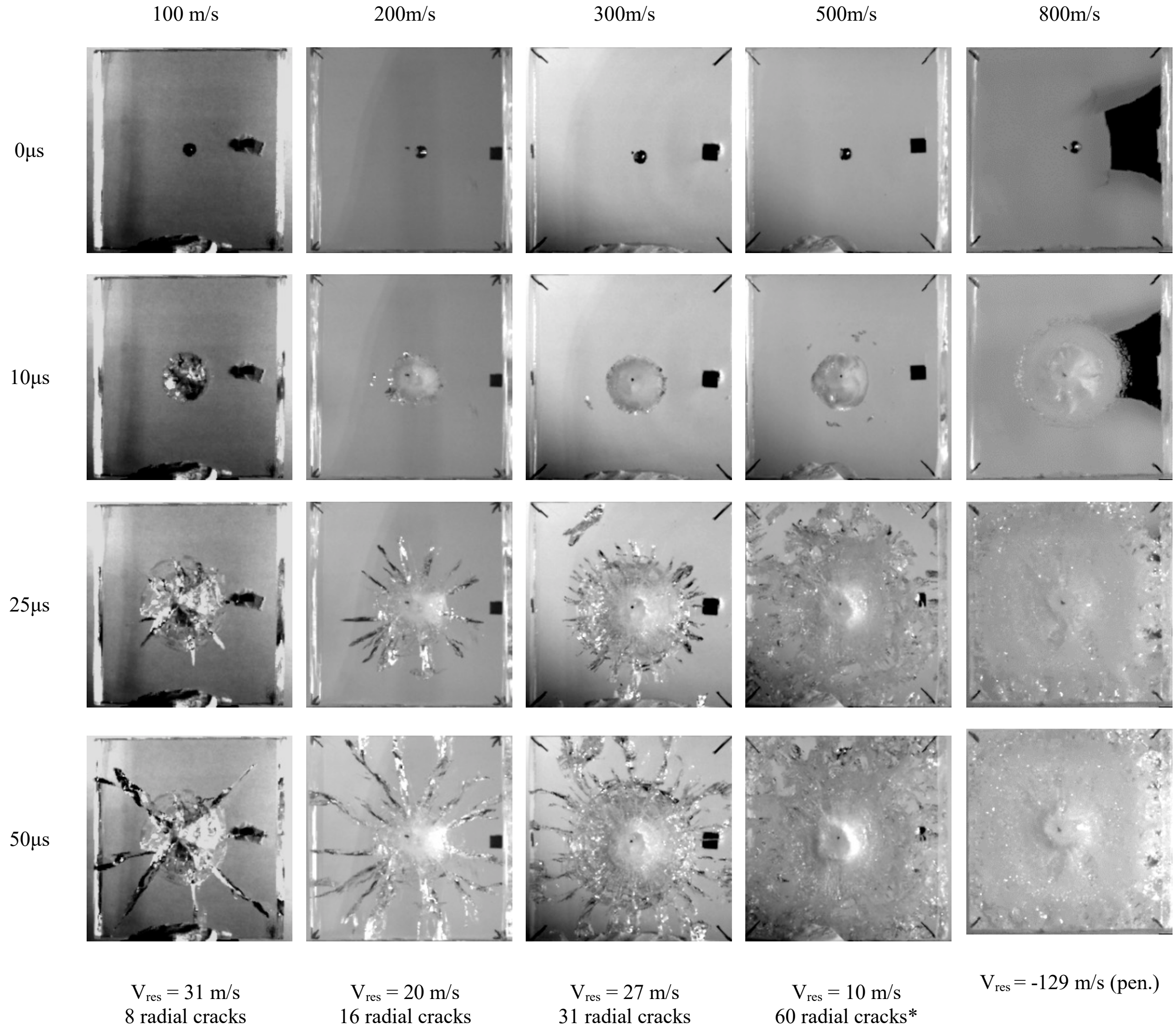

*Figure 29: Damage progression in SLG at select impact velocities*

*Table 8 : Damage front radius and number of radial cracks developed in target*
± = 1 standard deviation (coefficient of variation in brackets where applicable)

| Experimental Data | | |
|---|---|---|
| Impact Velocity *(m/s)* | Radial Cracks *(#)* | Damage Radius (Zone 3) *(mm)* |
| 103 | 8 | 26.9 |
| - | 6 | 28.2 |
| - | 10 | 21.9 |
| 200 | 17 | 21.8 |
| 199 | 16 | 21.5 |
| 198 | 15 | 18.8 |
| 299 | 31 | 33.5 |
| 300 | 29 | 29.4 |
| 302 | 34 | 29.5 |
| 497 | -* | Whole Tile |
| 504 | -* | Whole Tile |
| 503 | 60 | Whole Tile |
| 567 | -* | Whole Tile |
| 565 | -* | Whole Tile |
| 523 | -* | Whole Tile |
| 648 | -* | Whole Tile |
| 649 | -* | Whole Tile |
| 658 | -* | Whole Tile |
| 805 | -* | Whole Tile |
| - | -* | Whole Tile |
| - | -* | Whole Tile |

| Aggregate Results | | |
|---|---|---|
| Nominal Test Velocity *(m/s)* | Radial Cracks *(#)* | Damage Radius (Zone 3) *(mm)* |
| 100 | 8±2<br>(0.25) | 26±3<br>(0.12) |
| 200 | 16±1<br>(0.06) | 21±4<br>(0.19) |
| 300 | 31±3<br>(0.10) | 31±2<br>(0.06) |
| 500 | 60 | Whole Tile |
| 550 | * | Whole Tile |
| 650 | * | Whole Tile |
| 800 | * | Whole Tile |

* radial cracks not visible through comminution
**number of radial cracks estimated by counting cracks in a 60° arc

At low velocities (e.g. 100 m/s), discrete fracture was the primary mode of failure (Figure 30). A fracture cone formed over 25 μs post impact (Figure 30A-C), and radial cracks extended to the edges of the tile (Figure 30D).

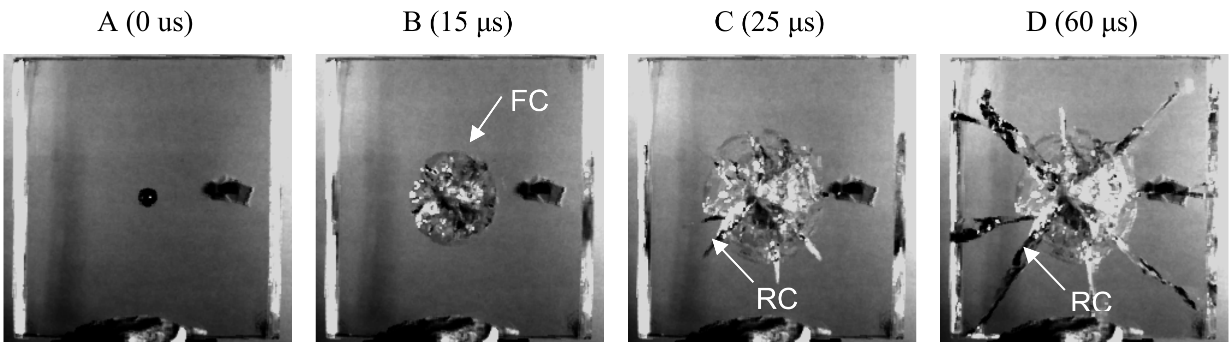
A (0 us) B (15 µs) C (25 µs) D (60 µs)

*Figure 30: Progression of a fracture cone and radial cracking at 100 m/s sphere on glass tile impact test (FC = fracture cone, RC = radial crack)*

At intermediate velocities (e.g. 500 m/s), comminution and discrete fracture were present (Figure 31). Discrete fracture preceded the damage front (Figure 31A) and acted as a point of damage initiation (Figure 9B), that eventually coalesced with the main damage front (Figure 31C).

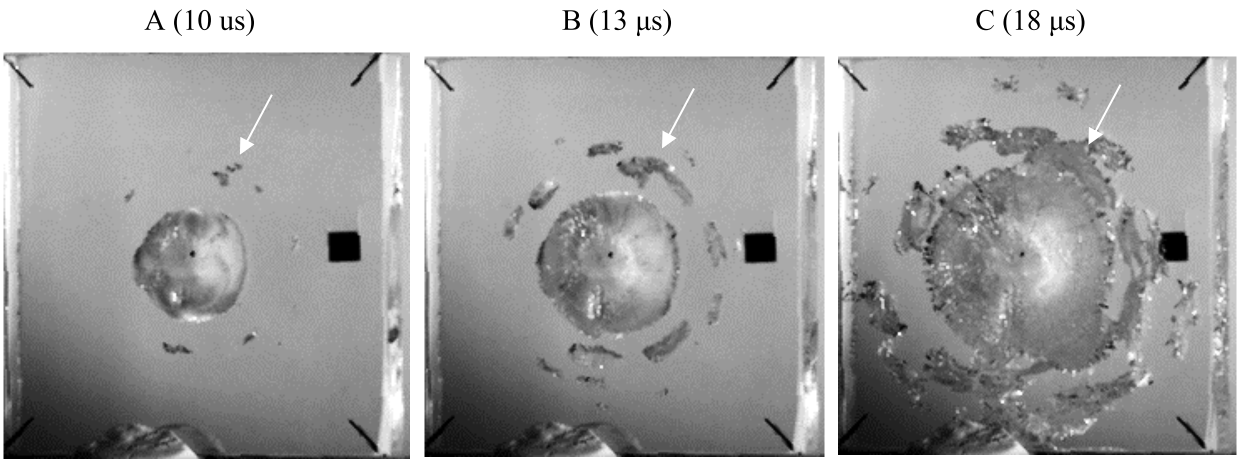
A (10 us) B (13 µs) C (18 µs)

*Figure 31: Growth of discrete fracture ahead of main front present at 500 m/s sphere on glass impact (arrow indicates growth of discrete fracture ahead of main front)*

At velocities where the projectile perforated the target (e.g. 800 m/s), bulk comminution was the dominant mode of failure (Figure 32).

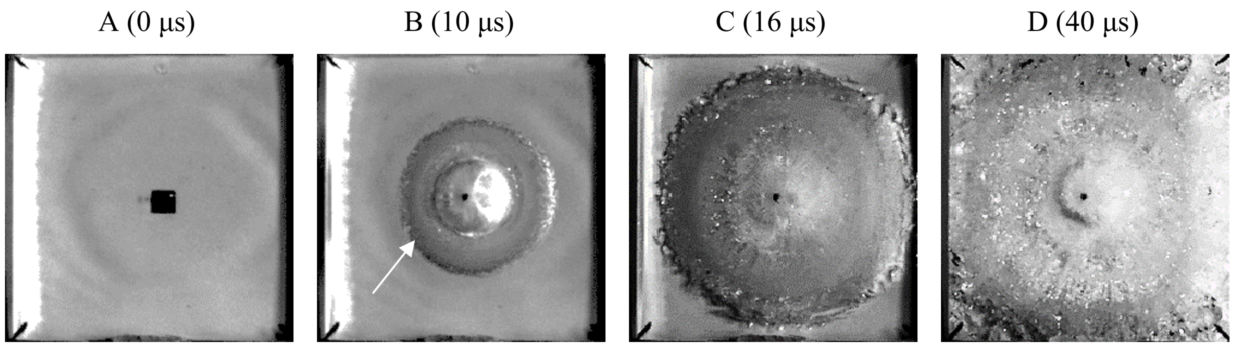
A (0 µs) B (10 µs) C (16 µs) D (40 µs)

*Figure 32: Progression of damage front for an 800 m/s sphere on glass impact (arrow indicates damage front)*

The projectile (spheres) did not fail in any impact case; however, minor plastic deformation and marring occurred at the 800 m/s impact cases (Figure 33).

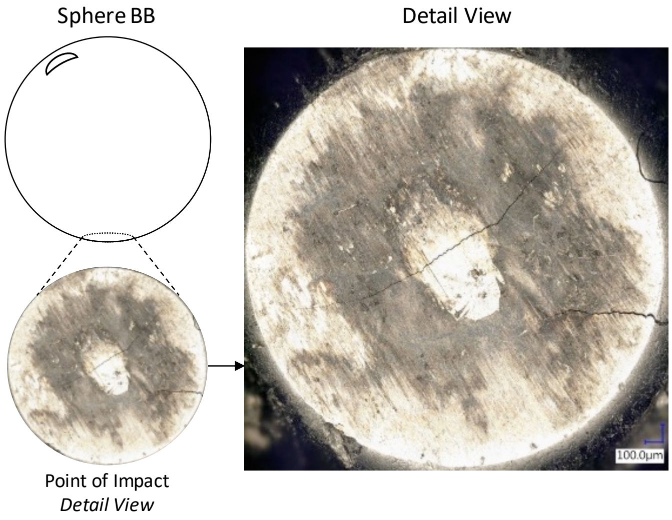

*Figure 33: Close up of steel sphere (ball bearing) after 800 m/s impact (Credit Chi-Hsiang Liao)*

The projectile kinematics camera had an adequate frame rate for projectile tracking, but at higher velocities (800 m/s) ejected material covered the projectile, making it difficult to track. The frame rate of the kinematics camera (Camera A) was too low to capture damage propagation through the thickness of the tile. The damage propagation camera was able to capture the damage progression in all tests. The resolution was limited to 240 x 240 pixels once the video was cropped to fit the target resulting in a spatial resolution of 0.4 mm per pixel. This was sufficient for single point displacement measurements; however, this resolution was too coarse for any velocity measurements. A deviation of one pixel or 0.4 mm, resulted in an error of ± 423 m/s, an error that is on the scale of crack and damage propagation velocities. A tenfold increase in spatial resolution would be required to reduce velocity measurement error within 5%.

## 4.2 Split Hopkinson Pressure Bar Test Results: Direct Compression and Diametral Splitting

Two series of tests were performed on the split Hopkinson bar apparatus: the direct compression test to assess the compressive strength of soda-lime glass at high rates, and the dynamic Brazilian test to determine the tensile strength of soda-lime glass at high rates. Due to technical issues (missing transmitter bar signal during testing), dynamic equilibrium could not be confirmed in the direct compression tests. Dynamic equilibrium in the dynamic Brazilian tests was confirmed; however, the tests showed some variability between tests with an average bar strain to failure of 3.14 x$10^{-4}$ ± 0.8 x$10^{-4}$ mm/mm. The samples did not fail in a purely tensile manner, indicating that the sample was not loaded as expected for a Brazilian splitting test. Opto-digital microscopy showed that the samples had a step offset along their width as a consequence of their manufacturing, and resulted in the samples to split orthogonal to their diameter. Due to this non-standard failure, tensile strengths could not be directly assessed from these results. The direct compression test data was not used due to the lost transmitted pulse data. Although the diametral splitting test could not provide tensile strengths, they did provide valuable insights into the tensile failure of soda-lime glass and provided a set of quantitative data (bar strains) to validate models.

### 4.2.1 Direct Compression Test Results

The direct compression tests were performed using maraging steel bars to provide the high loads required to fail soda-lime glass in compression. Due to technical issues, the transmitted bar signal was not recorded during testing. Five (5) direct compression tests were performed (Figure 34). There was little variation between tests (Figure 35).

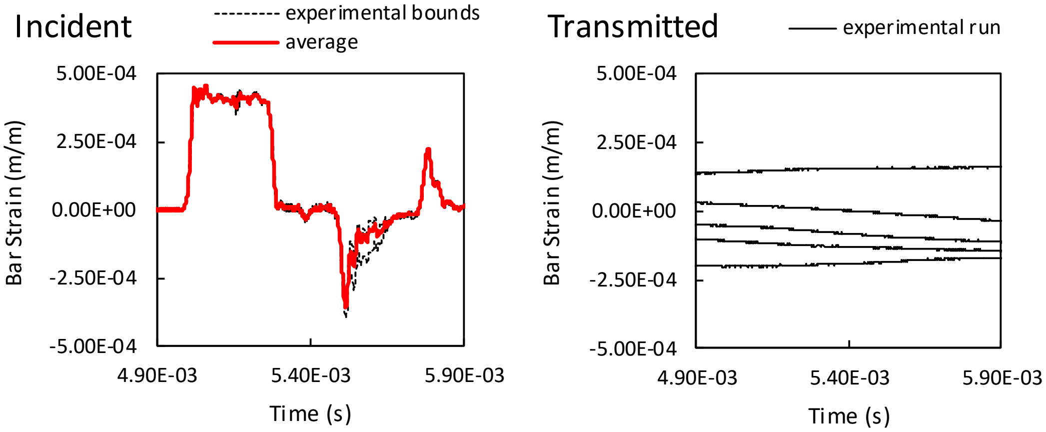

*Figure 34: Hopkinson bar strain output direct compression tests*

Due to the lost transmitted pulse, it was uncertain whether dynamic equilibrium was achieved during the direct compression tests. If dynamic equilibrium was assumed, the forces at the bar interfaces should be equal (P1 = P2). Using the bar-end force equations presented in section 2.2.3 (Equation *11*, Equation *12*) the transmitter bar strains were estimated by subtracting the incident strain from the reflected strain (Figure 35). The transmitter bar strain could then be used to estimate the forces in the sample over time using the bar-end force equations (Equation *11*, Equation *12*), bar strains, elastic properties of the bar ($E_{bar}$ = 70 GPa) and bar diameter (D = 25.4 mm) (Figure 36).

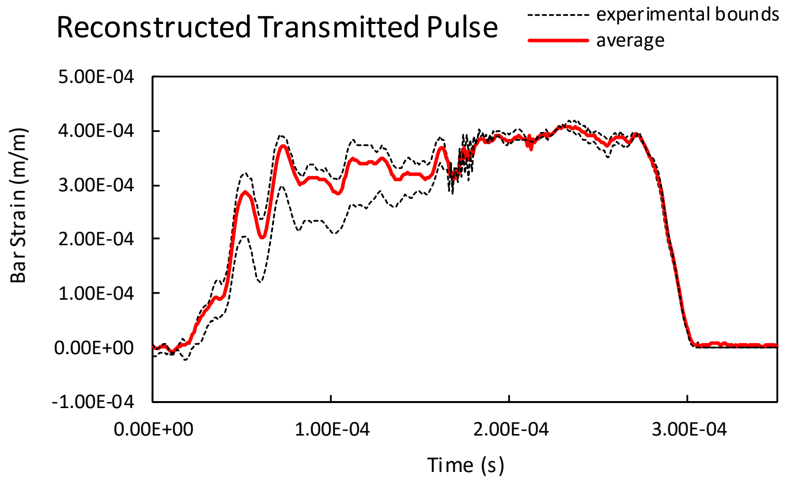

*Figure 35: Reconstructed transmitted pulse for direct compression tests*

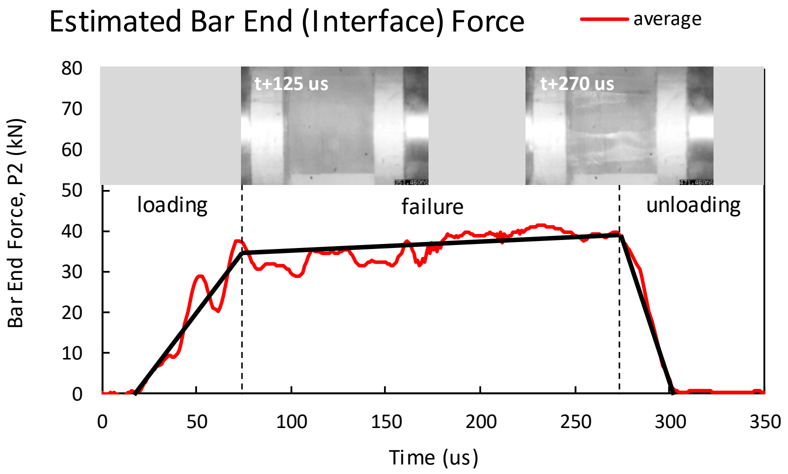

*Figure 36: Interface 2 bar-end force over time for direct compression test*

The calculated peak load on the sample was 41.4 kN resulting in a peak compressive stress of 81.7 MPa if uniaxial compressive loading was assumed. The peak force was maintained for much of the loading (from 75 – 275 us) with sample failure occurring much closer to the unloading phase in the test (around 270 μs). Although the direct compression tests provided repeatable and quantitative data, a key requirement of performing Hopkinson bar testing (achieving dynamic equilibrium) could not be verified due to the lost transmitter bar signal. Therefore, the direct compression data was not used for the rest of the study.

### 4.2.2 Diametral Splitting (Brazilian) Tests

A total of nineteen (19) dynamic Brazilian tests were conducted to assess the tensile strength of soda-lime glass at high rates. In two tests, the samples shifted during loading, resulting in spurious results and in one test the transmitter bar pulse was missing due to hardware issues. In total, three repeats were identified as outliers and were not included in the analysis. The dynamic Brazilian tests were performed using aluminum bars. Post-test analysis indicated that the incident pulses were consistent for all 16 tests, with an input strain of $6.0 \times 10^{-4}$ (Figure 37).

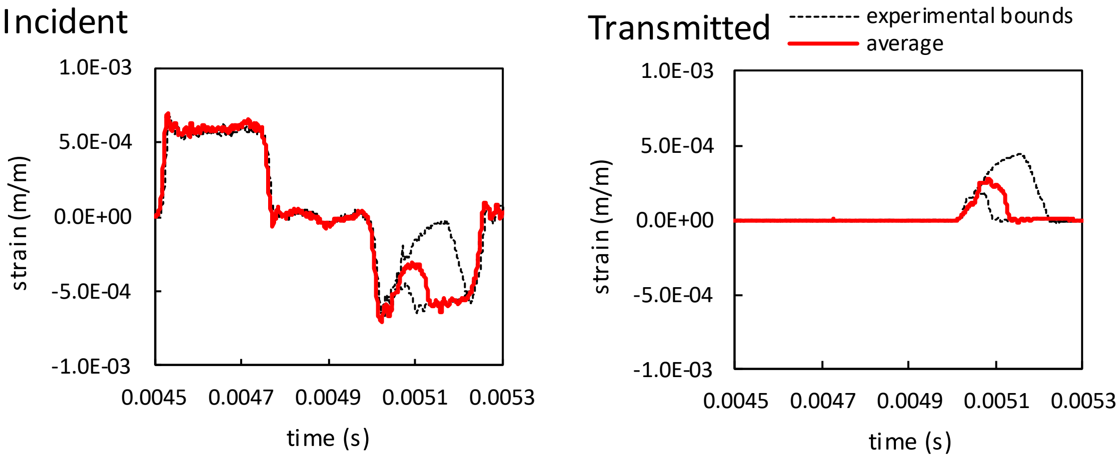

*Figure 37: Hopkinson bar strain output for Brazilian test*

For the dynamic Brazilian tests, dynamic equilibrium was confirmed by comparing the sum of the incident and reflected pulse to the transmitted pulse peak strain (Figure 38). Using the bar-end force equations presented in section 2.2.3 (Equation *11*, Equation *12*), the forces at the sample interfaces were determined. For example, in the sample D1-14, the peak strain at interface 1 and interface 2 were $3.026 \times 10^{-4}$ mm/mm and $2.788 \times 10^{-4}$ mm/mm respectively, or bar-end forces of 10.74 kN and 9.90 kN, a percentage difference of 9%. The loads resulted in a peak bar stress of 21.2 MPa, a stress that was much lower than the reported yield strength of the aluminum bars (276 MPa) (ASM International, 1995), confirming that the bars remained elastic during the test (a requirement of the Hopkinson bar analysis). Although the bars did not deform during loading, the aluminium shims did experience local plastic deformation due to the contact stresses between the shim and the sample.

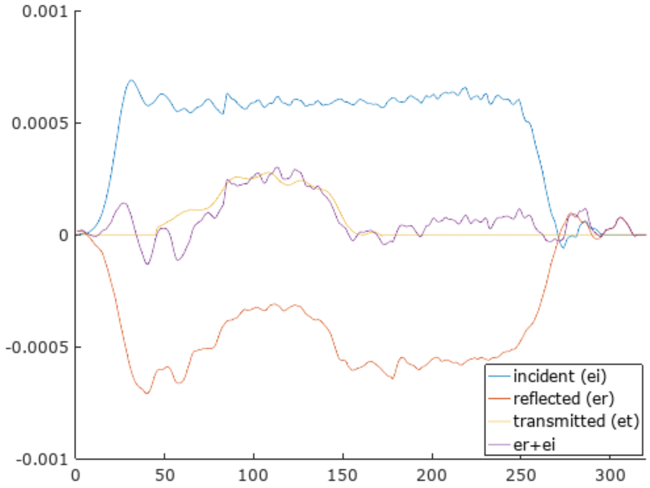

*Figure 38: Assessment of dynamic equilibrium of a representative diametral splitting test (sample D1-14)*

There was large variation in the reflected pulse, indicating a large variation in strain to failure of the samples (Figure 39). However, all the reflected traces followed a similar trend. The measured average bar strain to failure was 3.14 x$10^{-4}$ ± 0.8 x$10^{-4}$ mm/mm (coefficient of variation of 25%), or a compressive load of 11.1 kN. Using the tensile strength equation for a Brazilian test presented in section 2.3.3 (Equation 10), the average diametral tensile strength was found to be 4.19 MPa, much lower than the reported tensile strengths in literature (20-150 MPa, van der Velde, 2015).

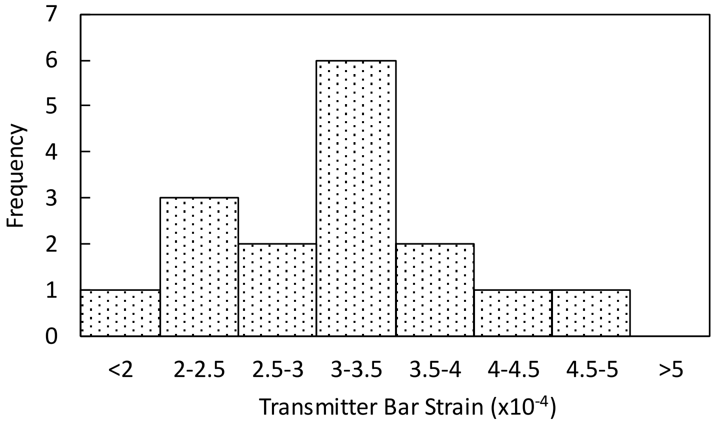

*Figure 39: Transmitter bar strain to failure histogram*

The difference in tensile strength may be accounted for by the failure mode of the sample deviating from a typical Brazilian test. In a typical Brazilian test, failure initiates at the centre of the sample forming a crack that then propagates along the diameter towards the upper and lower points of loading (Andreev, 1991). The failure in the soda-lime glass samples were more complex and could be separated into seven (7) phases (Figure 40).

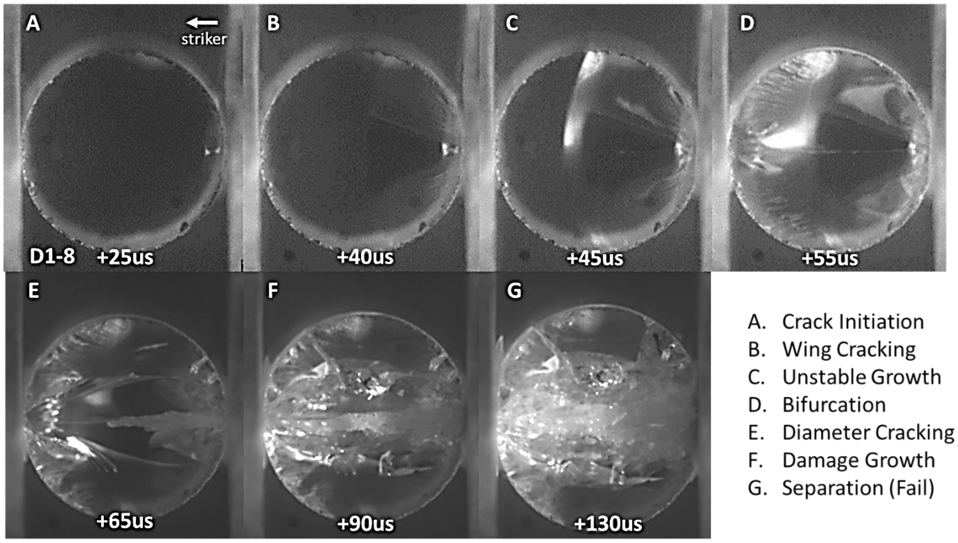

*Figure 40: Typical damage progression in a Brazilian test*

First, a crack initiated at the contact interface (Figure 40A). From this crack, two wing-like cracks propagated from the surface of the sample to the centre, running parallel to the faces of the cylindrical sample (Figure 40B). These cracks grew in a controlled manner, taking roughly 25 us to reach the centre of the samples. Once these cracks reached the midpoint of the sample, the two wing-like cracks merged and continued to propagate as a single crack, reaching the far end of the sample in 15 us and splitting the sample into two halves (Figure 40D). These halves were then loaded along the diameter, with cracks initiating from the points of contact and propagating along the diameter towards the centre until failure (Figure 40E-G). In a typical Brazilian sample, only steps E-G would be expected without bifurcation of the sample.

To determine the cause of the non-standard failure, an as-received dynamic Brazilian sample was observed under an opto-digital microscope. It was determined that the samples not only had a ridge about their circumference, but the samples were also offset by 0.2 mm (Figure 41). This was also evident in the pre-test measurement of the samples (Figure 22).

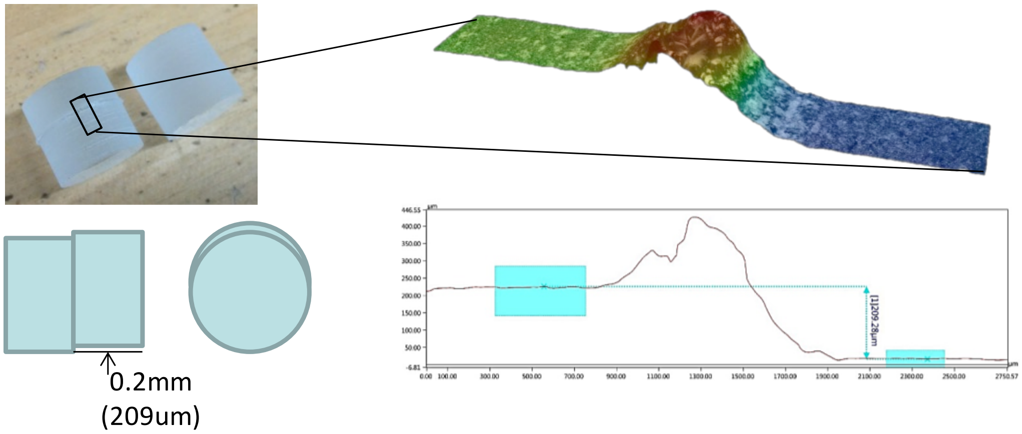

*Figure 41: Profile of unground sample along the length of the cylinder (Credit Chi-Hsiang Liao)*

This offset may have acted as a point of crack initiation and forced the sample to split transversely or parallel to the faces of the sample along the offset before failing across the diameter (diametral splitting) (Figure 42).

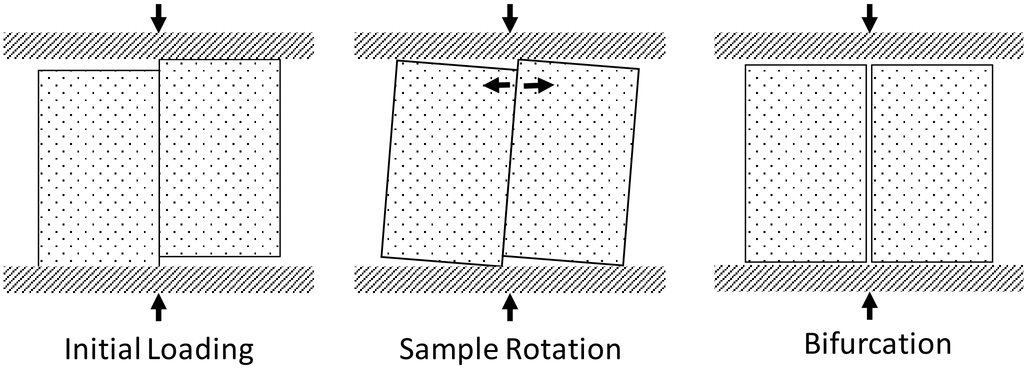

*Figure 42 : Possible mode of failure of dynamic Brazilian sample under loading*

The dynamic Brazilian tests showed some variability (coefficient of variation of 25 %) in results. The tests also failed in a non-standard manner and resulted in the tests underestimating the tensile strength of the material using the Brazilian test analysis (4.19 MPa). However, the tests were repeatable and showed a complex mode of failure that allowed for the characterization of the failure of soda-lime glass in tension. Although the tests could not be used to directly quantify the tensile strength of soda-lime glass at high rates, this set of data was used to further validate the soda-lime glass model in subsequent sections of this study using both high speed imaging for qualitative comparisons (Figure 40) and split Hopkinson bar strains for quantitative comparisons of numerical methods (Figure 37).

## 4.3 Depth of Penetration Test Results

The depth of penetration tests were repeatable for all test configurations (4 test thicknesses and 3 test velocities). The projectile fully perforated the glass tile in all tests where glass tiles were tested. Typically, the projectile penetrated the polycarbonate backing and continued to travel along a linear path. In some cases the projectiles deviated from an axial path (with respect to the cylinder). The projectile displacements were tracked over time using high speed imaging and video analysis software (Figure 43).

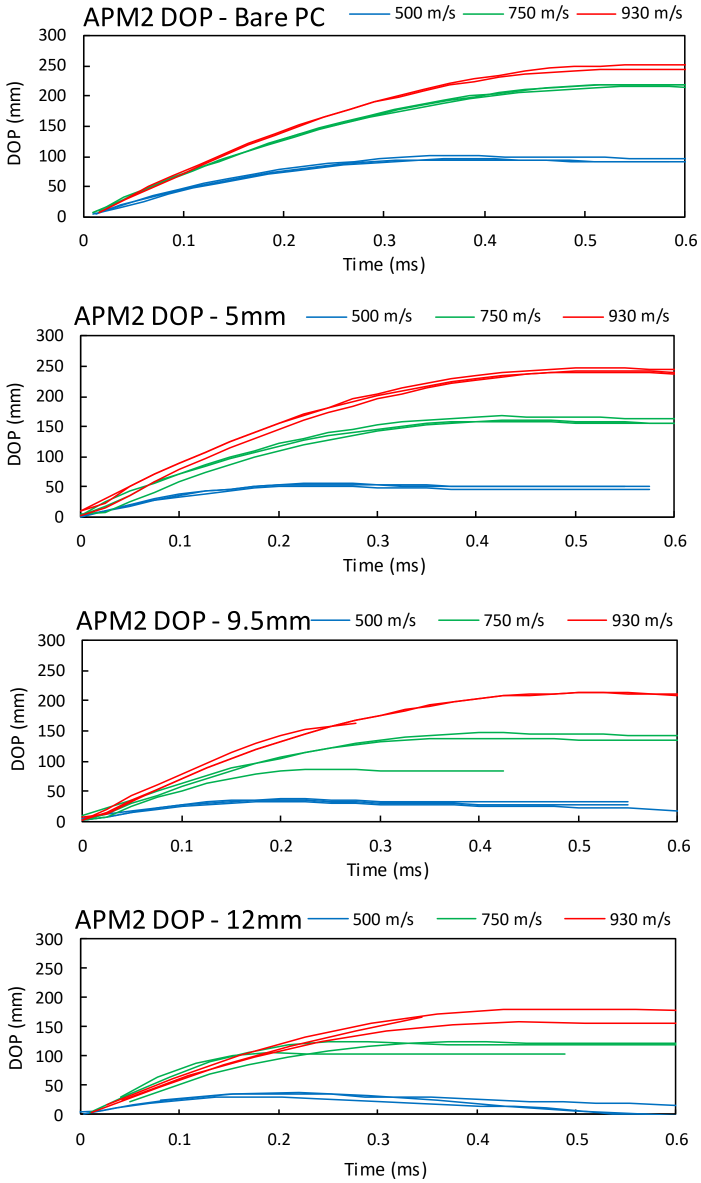

*Figure 43: Depth of penetration of AP-M2 into bare polycarbonate (top), and three SLG thicknesses versus time*

In some tests at higher impact velocities or with thicker glass material, the projectile deviated from an axial path upon entering the polycarbonate backing and left the viewing window on the test sample (Figure 44). Generally, thicker pieces of glass increased the variability in the final depth of penetration (Table 9).

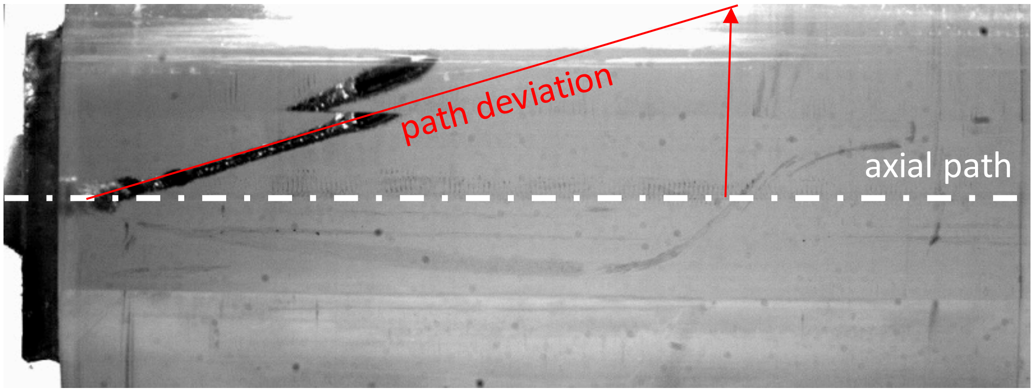

*Figure 44: Projectile path deviating from the viewing window machined onto side of DOP cylinder (test G8)*

In other cases, the AP-M2 core fractured into two pieces upon entering the polycarbonate, and resulted in lower reported depths of penetration (Figure 45). Tests like this were rare (two in entire test matrix) and were removed from the dataset as outliers.

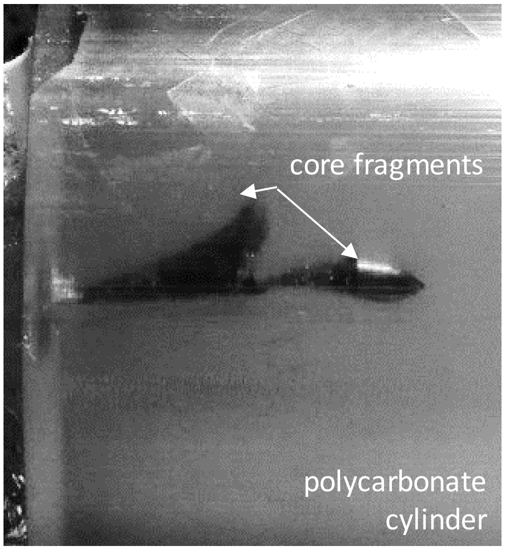

*Figure 45: Projectile core fracture upon entering the polycarbonate backing (test T19)*

*Table 9: Depth of penetration results (AP-M2 on Glass/PC)*

± = 1 standard deviation (COV in parentheses where applicable)

**red - projectile path deviation**

| | DOP (mm) | Repeat 1 | Repeat 2 | Repeat 3 | Average |
|---|---|---|---|---|---|
| 500 m/s | PC only | 95 | 95 | 101 | 97 ± 3<br>(0.03) |
| | 5 mm + PC | 52 | 54 | 56 | 54 ± 2<br>(0.04) |
| | 9.5 mm w/ PC | 33 | 35 | 38 | 35 ± 2<br>(0.07) |
| | 12 mm w/ PC | 30 | 37 | 38 | 35 ± 4<br>(0.12) |
| 750 m/s | PC only<br>[763 m/s] | 216 | 218 | 220 | 218 ± 2<br>(0.01) |
| | 5 mm<br>[765 m/s] | 159 | 160 | 167 | 162 ± 4<br>(0.03) |
| | 9.5 mm<br>[780 m/s] | **86**$^{**}$ | **138** | **147** | 124 ± 33<br>(0.27) |
| | 12 mm | **106**$^{**}$ | **124** | **125** | 118 ± 11<br>(0.09) |
| 930 m/s | PC only | 245 | **248** | 252 | 248 ± 4<br>(0.01) |
| | 5 mm | **240** | **242** | 247 | 243 ± 3<br>(0.01) |
| | 9.5 mm | **213** | * | **213** | 213 ± 0<br>(0.00) |
| | 12 mm<br>[890 m/s] | **158** | * | **181** | 170 ± 16<br>(0.10) |

$^{*}$projectile veered out of view, $^{**}$projectile failed on entry

The depth of penetration of the AP-M2 projectile was tracked in most tests, except in cases where the projectile deviated from a straight path out of view of the camera (Figure 44) or in cases where the projectile core fractured (Figure 45). The tests were repeatable with less than 12% variation in tests where the projectile penetrated the polycarbonate and continued to travel straight. Using a video tracking tool and high speed video from the tests, depth of penetration versus time curves were measured and could be used to assess the behaviour of polycarbonate models. Final depths of penetration were also recorded (Table 9) with and without glass and could be used assess the ballistic performance of glass and validate models in a quantitative manner.

# 5. Numerical Modelling Methods

The numerical model development process took place in three phases; assessment of grid convergence and robustness, constitutive model parameter identification and finally validation of a soda-lime glass ballistic model. All models were developed in an explicit dynamics finite element code (LS-DYNA) and all models were developed in version R7.1.2. All models were run in double precision to minimize round-off errors and default solver parameters were used throughout unless otherwise stated.

Three commonly used solution methods (the finite element method, smooth particle hydrodynamics and element free Galerkin) were used to model the sphere on glass tile impacts (section 4.1). The sphere on glass tile impact data set was used in the verification portion of the study since it was a readily available data set and represented a typical use case of a ballistic soda-lime glass model. The models were used to assess ballistic fidelity, convergence tendencies and robustness of the modelling techniques, using a set of literature material parameters for soda-lime glass (Johnson & Holmquist, 1995).

Once suitable numerical methods were established, a combination of literature data, experimental data and numerical models were used to identify suitable parameters for the JH-2 ceramic model. First, confined compression data of soda lime glass was used to characterize the pressure-strength relation of the JH-2 model. Limitations of using a quasi-static set of data to fit a model for a ballistic impact were discussed and the sphere on glass tile data set was introduced to improve the updated parameters. The updated JH-2 parameters predicted projectile kinematics in the sphere on glass tests well.

After appropriate constitutive model parameters were determined, the soda-lime glass model was validated against three experimental data sets; the dynamic Brazilian test data (section 4.2.2) to assess the tensile behaviour of the model, the sphere on glass tile data set used (section 4.2) as partial validation to confirm the damage propagation characteristics of the model (section 4.1) and the depth of penetration tests (section 4.3) to assess ability of the model to predict the ballistic performance of soda lime glass.

## 5.1 Assessment of Grid Convergence and Model Stability

To assess numerical methods used in ballistic impact modelling, three common solution methods (the finite element method, element free Galerkin and smooth particle hydrodynamics) used in the modelling of ballistic impact were compared with respect to their ballistic fidelity (the ability of the model to predict projectile kinematics and material damage) and convergence tendencies. The sphere on glass tile model was used extensively in the verification procedure in the study for multiple reasons. First, the tests covered a wide range of impact velocities and presented damage features commonplace in ballistic impact of ceramics. Secondly, the tests were straight forward to model due to the simplicity of the tests themselves and easy to debug due to access to the raw data collected. Finally, the sphere on glass tests were a ballistic impact test, a representative use case of the model.

To assess the finite element method, the sphere on glass (SOG) experiments were modeled in LS-DYNA as a full 3D model (Figure 46). Both the tile (target) and the sphere (projectile) were modeled with hexahedral elements. The projectile was given an initial velocity equal to the nominal impact velocity of each test series (100, 200, 300, 500, 550, 650 and 800 m/s).

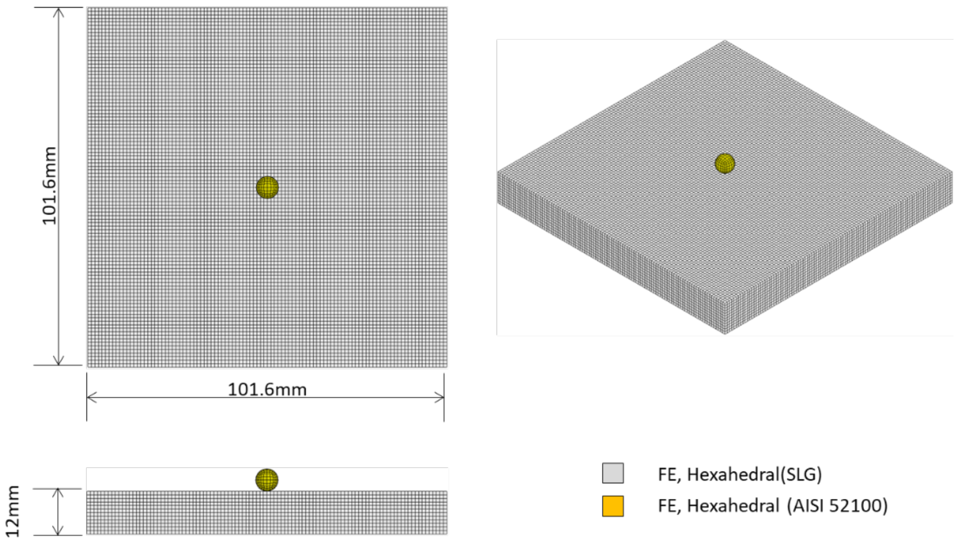

*Figure 46: Sphere on glass tile FE model.*

The projectile was modelled with elastic properties (*MAT_ELASTIC, LS-DYNA) obtained from literature ($E = 207$ GPa, $\rho = 7830$ kg/m$^3$, $\nu = 0.3$) (Guo, 2006). The hardened steel ball bearings were chosen due to their high strength to act as a non-failing projectile and were not expected to undergo significant plastic deformation during the impact as observed in section 4.1 (Figure 33). The soda-lime glass tile was modelled using the JH-2 model (*MAT_JOHNSON_HOLMQUIST_CERAMICS, LS-DYNA, Section 2.3.1). The sample was meshed with an initial element size of 0.5 mm and alternate mesh sizes were investigated to quantify the discretization error in the model. To obtain projectile kinematics, rigid body displacements, velocities and accelerations (as opposed to nodal quantities) of the projectile were extracted from the simulation via *DATABASE_MATSUM. The projectile kinematics were extracted at a frequency of 1 MHz.

To verify the model, a preliminary set of material parameters were required. Johnson & Holmquist (1995) proposed a set of JH-2 parameters for soda lime glass, with parameters determined using coupon level tests and full-scale ballistic impact tests on confined cylinders (section 2.3.2). This set of baseline parameters will be referred to as the JH-1995 parameters for the remainder of this study. The JH-1995 parameters have been shown to over-predict the strength of soda-lime glass in tension (Zhang, 2015), but they provide a good starting point for the development of a ballistic model (Table 10) and were used in the verification portion of the study.

*Table 10 : Johnson & Holmquist (1995) published parameters for SLG*

| | *Bulk* | *Fractured Strength* | | | *Damage* | | *Intact Strength* | | | *S.Rate* | *Equation of State* | | | *Shock* | | *Elastic* | |
|---|---|---|---|---|---|---|---|---|---|---|---|---|---|---|---|---|---|
| *Units* | - | - | - | - | - | - | - | - | MPa | - | GPa | | | GPa | | $kgm^{-3}$ | GPa |
| *Symbol* | β | B | m | $SF_{max}$ | D1 | D2 | A | n | T | c | K1 | K2 | K3 | HEL | PHEL | ρ | G |
| JH-1995 | 1 | 0.2 | 1 | 0.5 | 0.043 | 0.85 | 0.93 | 0.77 | 150 | 0.003 | 45.4 | -138 | 290 | 5.95 | 2.92 | 2530 | 30.4 |

The erosion parameter (FS) of the JH-2 model was determined through a sensitivity study to study the effect of erosion strain on the residual projectile velocities. The results of this study can be found in Appendix A. Element erosion was required in the numerical analysis to maintain numerical stability. An erosion strain of 5.0 was a good balance between simulation runtimes and simulation accuracy and had a negligible effect on projectile kinematics. This erosion strain was used for the remainder of the study.

It is important to quantify discretization error in computational models to identify a suitable finite element mesh size for impact analysis. A common method used to study the effect of discretization error is Richardson extrapolation, where models with three successively finer mesh sizes are solved and a parameter of interest is assessed at each level of refinement. The results allow for quantification of the discretization error through extrapolation to a converged solution. To study the effects of discretization error on the current model, three characteristic mesh sizes of 1.00 mm (coarse), 0.50 mm (medium), and 0.25 mm (fine) meshes were selected (Figure 47).

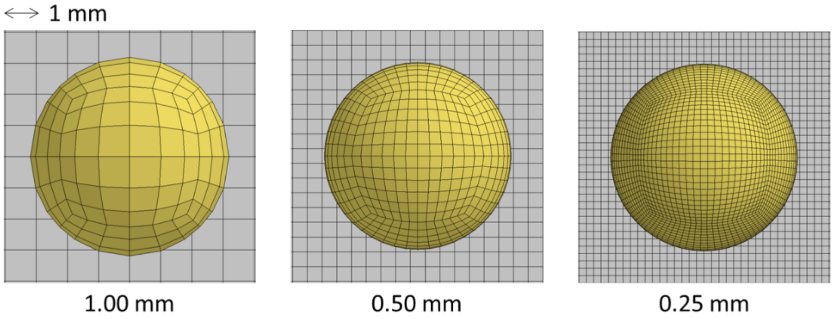

*Figure 47: Three levels of mesh refinement of the sphere on glass test used in grid convergence study.*

To assess the validity of using a Richardson extrapolation to evaluate the model, intermediate models with characteristic lengths of 0.80 mm, 0.60 mm, 0.40 mm, 0.35 mm and 0.30 mm were also run to confirm asymptotic behavior of the parameter of interest over the mesh range of the study (Table 11). The grid independence study was performed at one velocity (800 m/s) as it was representative of projectile velocities encountered in ballistic testing, referenced in the NATO AEP-55 test protocol (NATO Standards Organization, 2011). Other test velocities were not considered in this study. The simulated residual velocities were measured once projectile velocities had stabilized (i.e.: dv/dt = 0, typically 50 µs for non-perforating events and 200 µs for perforating events).

*Table 11: Grid convergence study FE mesh sizes*

| Mesh Length | Relative Length |
|---|---|
| **(C) 1.00** | **1.00** |
| 0.80 | 1.25 |
| 0.60 | 1.67 |
| **(M) 0.50** | **2.00** |
| 0.40 | 2.50 |
| 0.35 | 2.86 |
| 0.30 | 3.33 |
| **(F) 0.25** | **4.00** |

In addition to a standard hexahedral mesh finite element model, two other models were developed to study the effects of using different discretization methods including element free Galerkin (EFG) and smooth particle hydrodynamics (SPH) methods (Section 2.4.2).

The EFG simulation was modelled with quarter symmetry (Figure 48) due to computational limitations. A symmetric boundary condition was applied to the interior faces of the tile. The solver used in this analysis (LS-DYNA R712) had a ~20GB limit on memory, making full three dimensional EFG models infeasible

(Table 12). The model was also subdivided such that there was an EFG zone near the point of impact and hexahedral elements supporting the EFG zone away from the point of impact. The size of the mesh-free zone (20 x 20 mm in the quarter symmetry model) was determined by running preliminary models to determine the level of damage. The EFG zone was coupled to the hexahedral support via a tied contact.

*Table 12: List of select simulation runs and runtime statistics (hh:mm) run on 6 cores of an i7-6850 (3.60 GHz clock speed)*

| Mesh Size | FEM-FULL | SPH-QUARTER | EFG-QUARTER | EFG-FULL |
|---|---|---|---|---|
| 0.25mm | 10.93 GB<br>(06:18) | 2.20 GB<br>(02:16) | 2.82 GB<br>(02:21) | >22 GB<br>(ERROR) |
| 0.30mm | 6.42 GB<br>(02:54) | 1.29 GB<br>(01:10) | 1.66 GB<br>(01:16) | - |
| 0.35mm | 4.05 GB<br>(01:30) | 0.81 GB<br>(00:35) | 1.04 GB<br>(00:45) | - |
| 0.40mm | 2.68 GB<br>(00:48) | 0.56 GB<br>(00:16) | 0.70 GB<br>(00:21) | - |
| 0.50mm | 1.38 GB<br>(00:21) | 0.28 GB<br>(00:05) | 0.35 GB<br>(00:09) | 6.27 GB<br>(03:18) |
| 0.60mm | 0.80 GB<br>(00:09) | 0.17 GB<br>(00:03) | 0.21 GB<br>(00:04) | - |
| 0.80mm | 0.34 GB<br>(00:03) | 0.08 GB<br>(00:01) | 0.10 GB<br>(00:01) | - |
| 1.00mm | 0.18 GB<br>(00:01) | 0.04 GB<br>(00:00) | 0.05 GB<br>(00:01) | 0.79 GB<br>(00:09) |

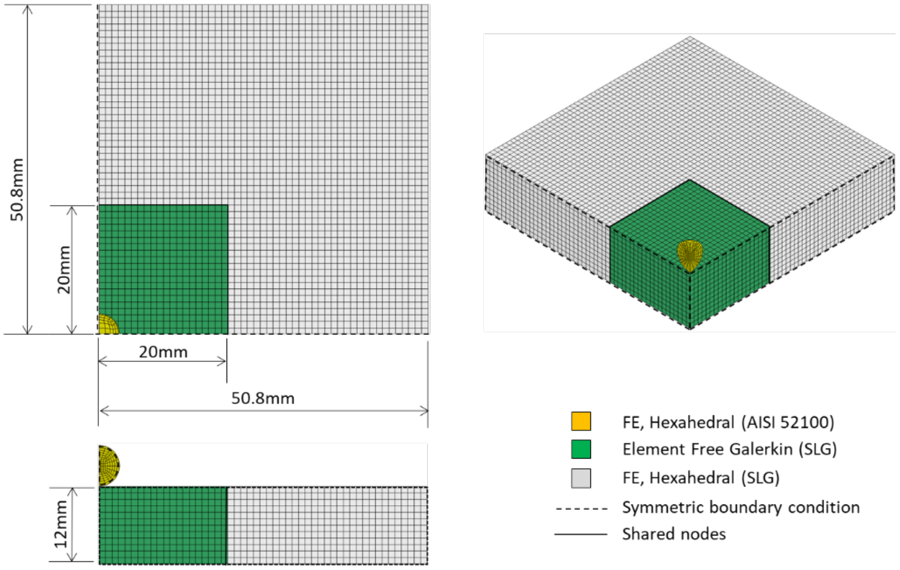

*Figure 48: Sphere on glass tile EFG model using quarter symmetry and incorporating hexahedral finite elements outside of the impact zone to address computational limitations*

The SPH model also incorporated quarter symmetry (Figure 49), utilizing a SPH zone surrounded by a hexahedral finite element mesh due to computational limitations. The SPH model was identical in setup to the EFG model, except for the contact definition between the target and the projectile. Using a projectile meshed with hexahedral elements and a SPH target resulted in large, artificial nodal displacements at the contact interface. To mitigate this, the projectile and target were both modelled in SPH.

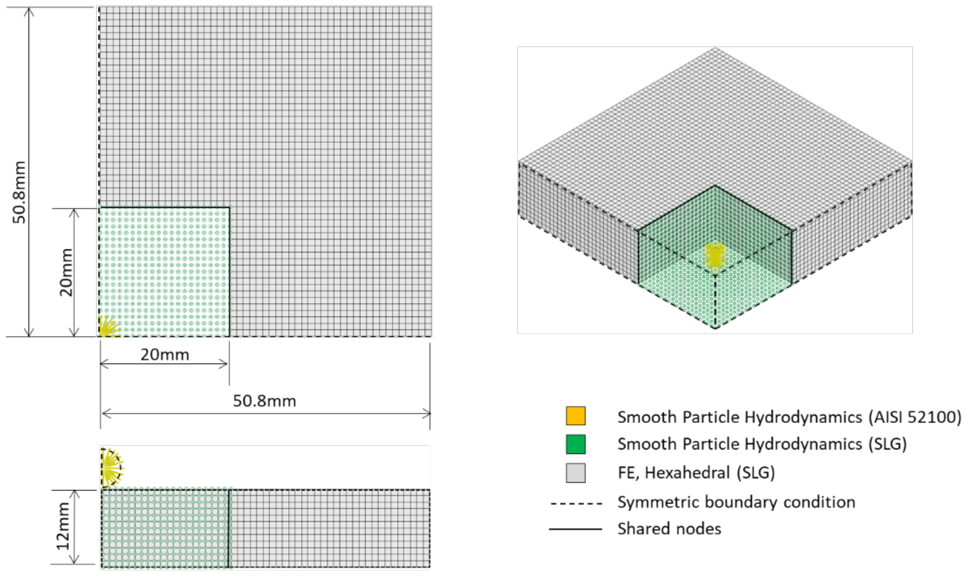

*Figure 49: Sphere on glass tile SPH model using quarter symmetry and incorporating hexahedral finite elements outside the impact zone*

To test the robustness of the model, the sphere on glass model was solved under two loading conditions; off-centre hit in the Y-axis and a multi-hit simulation (Figure 50). The off-centre models were performed at six difference eccentricities (s): 0.1 mm, 0.5 mm, 1 mm, 5 mm, 10 mm and 50 mm. An offset of 50 mm corresponded to an impact at the edge of the 100 mm wide glass tile. The multi-hit simulation was run with the spheres placed in a circle of radius 15 mm located at the geometric centre of the tile to mimic a multi-hit test. This distance was chosen so the regions of damage from each impact would overlap. The impacts occurred 50 µs apart in time to allow for the damage from each impact to progress, prior to the subsequent impact. The robustness test were performed at 800 m/s. Since no corresponding experimental data was available, the robustness test was run with the goal of assessing model stability (running to completion).

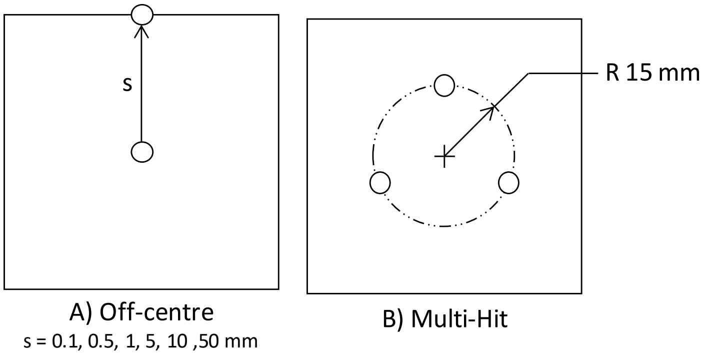

*Figure 50: Simulated configurations to test model robustness*

**The effect of numerical interfaces on wave propagation**

A numerical interface (a change the numerical media, for example, element formulation, solution method or mesh density, that is purely a consequence of the numerical analysis) can affect the propagation of waves in a numerical analysis and sometimes result in artificial wave reflections (Zukas, 2004). Ballistic impact problems are wave propagation dependent, so spurious wave reflections can produce erroneous results. Two numerical interfaces (sub-structuring a mesh and abrupt changes in mesh density) were studied using a simplified bar impact computational model to quantify the effects of these interfaces and assess whether these methods were appropriate to use when studying ballistic impact problems.

Due to the high computational cost of SPH and EFG, the sphere on glass models for both the mesh-free methods employed a sub-structuring technique where a mesh-free zone was supported by a FEM support. Since both SPH and EFG use a weighted average to determine material properties, it is possible that the interface between the mesh-free zone and finite elements may be interpreted as a free end as opposed to a continuous medium and may induce spurious local wave reflections. To quantify the magnitude of the wave reflections that may result due to this interface, an “end-to-end” bar impact simulation was run, where the tip of the bar (20 mm) was replaced with either EFG cells or SPH nodes (Figure 51). A model with hexahedral elements was also run to use as a reference case. The model was a simplification of the Hopkinson bar model described in section 5.3. In an ideal “end-to-end” bar test, the incident and reflected bar are placed in contact with no sample between the bars. 100% of the incident pulse should be transmitted to the transmitter bar without any reflection; however, some reflections occur due to imperfection in the bars. The peak stress between the incident and reflected pulses were compared to determine whether significant reflection occurred at the interface, using the finite element model as a baseline.

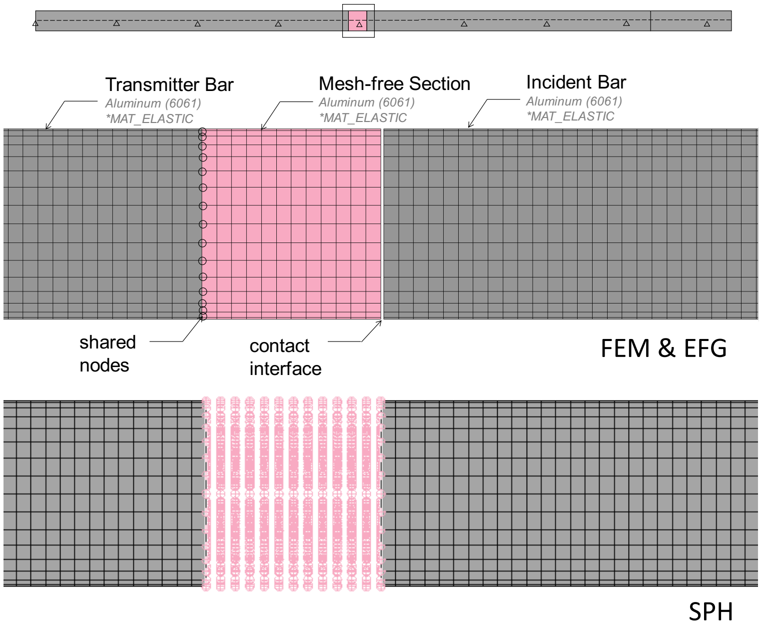

*Figure 51: End to end bar impact model to study internal wave reflections due to mesh-free interfaces*

For a given incident bar peak stress of 51 MPa, both the FEM and EFG models had a reflected peak bar stress of 2.70 MPa (5% reflection). The SPH model had a peak reflection of 9.13 MPa (18% reflection), a reflected stress that was much higher than the baseline (FEM) model (Figure 52), indicating that spurious wave reflections may occur at the mesh free interface of the SPH model. The sub structuring method used in this study may have some limitations when implemented with SPH to model ballistic impact, but is required due to computational limitations.

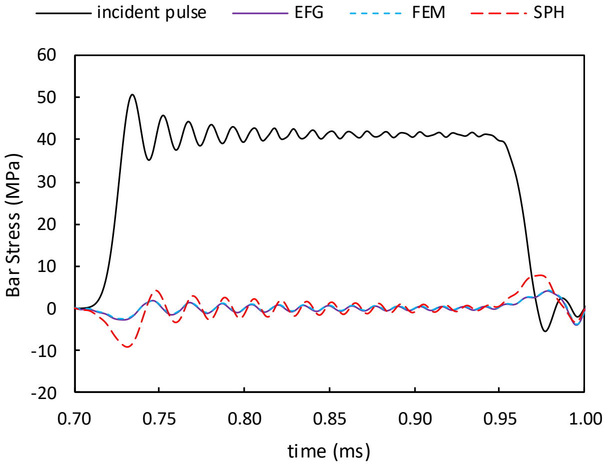

*Figure 52: End to end reflection simulation of various mesh-free interfaces (reflected bar stress)*

Abrupt changes in mesh size can also result in artificial wave reflections (Zukas, 2004). In this study, differing meshes were used either to facilitate proper contact or due to computational constraints. To quantify the magnitude of the wave reflections that may result due to an abrupt mesh change (transition from 1 mm to 0.5 mm), another "end-to-end" bar impact simulation was run, where the tip of the bar (20 mm) was replaced with finite elements of a finer mesh (0.5 mm) than the rest of the model (Figure 53).

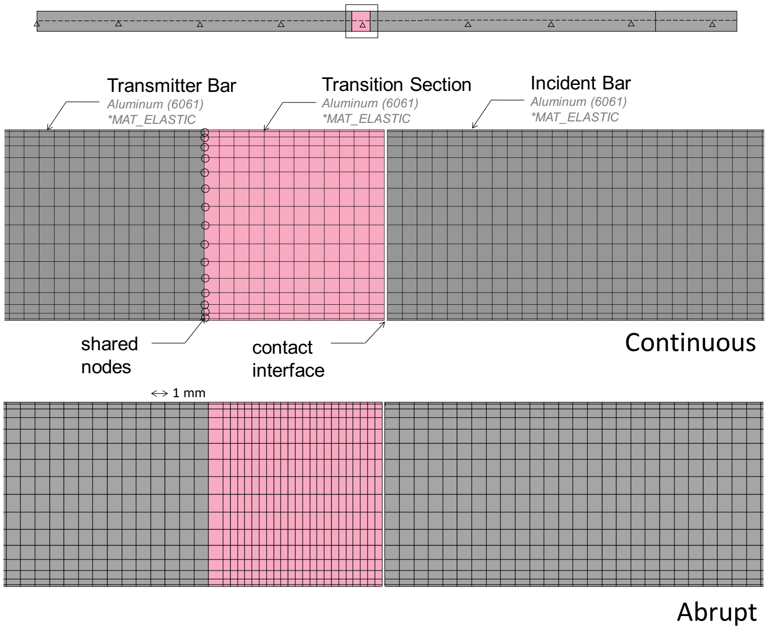

*Figure 53: End to end bar impact  model to study internal wave reflections due to an abrupt mesh change*

For a given incident bar peak stress of 51 MPa, both the continuous mesh (1 mm mesh throughout) and the abrupt mesh (1 mm to 0.5 mm to 1 mm) had a reflected peak bar stress of 2.70 MPa (5% reflection) (Figure 54). In the "end-to-end" bar impact, there was a negligible effect of an abrupt change in mesh on wave reflections.

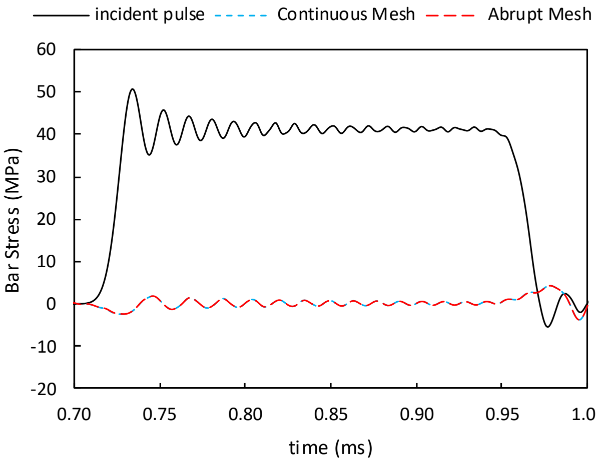

*Figure 54: End to end reflection simulation of for an abrupt mesh change (reflected bar stress)*

The “end-to-end” bar impact models were a useful tool in studying the propagation of waves through various numerical interfaces and quantifying the effects numerical features on wave propagation. However, the bar end impacts differ from ballistic impacts since the bar impacts occur at low speeds and at low deformation (as opposed to ballistic impacts that occur at high speed and result in large deformations), but these models allowed for some quantification of these effects.

## 5.2 Constitutive Model Parameter Identification

Once suitable numerical methods were identified and implemented, the methods were used to determine suitable parameters for the JH-2 model. The literature parameters used in the verification section were used to as a starting point in the parameter identification process. This study focused on the determination of the strength (A,N,T,B,M,$SF_{MAX}$, Equation 4 & Equation 5) and damage accumulation (D1,D2, **Error! Reference source not found.**) parameters. The parameter identification process was performed in three steps. First, confined compression data from literature was used to determine the pressure-strength relation of soda-lime glass. The hydrostatic tensile pressure to failure (T, Equation 4) was determined using analytical methods and literature data. Finally, the sphere on glass dataset was used to determine the fractured strength curve and the accumulation of damage in the model.

First, pressure-strength data was taken from literature (Dannemann et al., 2011) and the strength curves were fit using least squares regression fitting techniques implemented in MATLAB. The literature parameters used in this study have been shown to over predict the tensile strength of glass, so a lower tensile strength (30 MPa) was enforced during the fitting process (Zhang, 2015).

Since the publication of the JH-1995 parameters, many experiments have been performed in an attempt to characterize the pressure dependence of the strength of glass, most notably, the work of Dannemann et al. (2011). To determine the intact strength parameters, the intact pressure-strength data reported by Dannemann (2011) was fit using non-linear least squares regression tool in MATLAB (see Appendix A for code). To account for the tensile strength, the regression was weighted such that equal weight was assigned to fitting the compressive and tensile regions of the curve.

Due to the piecewise nature of the fractured strength curve (due to the $SF_{max}$ term), the parameters for the fractured strength curve were fit using an EXCEL file. $SF_{max}$ was determined by taking the average of the constant stress portion of the curve. The fractured strength equation was linearized such that the parameters could be obtained via a linear regression fit (see below).

$$\sigma_f^* = B(P^*)^m$$
$$\ln(\sigma_f^*) = \ln(B(P^*)^m)$$
$$\ln(\sigma_f^*) = \ln(B) + \ln((P^*)^m)$$
$$\ln(\sigma_f^*) = \ln(B) + m\ln(P^*)$$

Single element models with bulking enabled (beta = 1) showed oscillations in stress and pre-mature damaging of material (Figure 55). The single element tests used a pressure boundary condition (as opposed to a displacement controlled boundary condition) to simulate the hydraulic confinement used in the confined compression tests (Dannemann et al., 2011) and may have resulted in the oscillations. Bulking is a phenomenon seen in ceramic materials where cracking results to an expansion in material volume (Bless & Rajendran, 1996). If the ceramic is confined, the material experiences an increase in pressure (Bless, 2010), and therefore in increase in material strength (Johnson & Holmquist, 1994). The magnitude of the bulking phenomenon varies from material to material (Brace et al., 1966), and the bulking effect in amorphous glasses such as soda-lime glass are generally not well quantified (Gofrain et al., 2016). Attempts to quantify volumetric expansion in borosilicate glass (another amorphous glass used in transparent armour) have shown the bulking effect to be negligible (Dannemann et al., 2008).

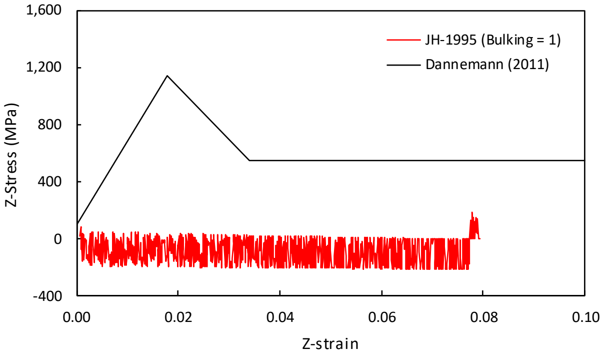

*Figure 55: Stress oscillations due to pressure boundary constraint and bulking effects.*

The parameters developed by Johnson & Holmquist (1995) set the bulking parameter to 1, but this behaviour was not confirmed through experimental testing. It has been shown that increasing the bulking parameter can result in artificially high rates of damage accumulation and can result in poor predictions of projectile kinematics (Taylor et al., 1999). Since the effects of bulking in soda-lime glass were not well quantified (Gofrain et al., 2016), and excessive bulking has been shown to lead to spurious projectile kinematics (Taylor et al., 1999), bulking effects were not included in the updated material model parameters. Bulking effects should be investigated further in future studies.

To determine the fractured strength (B) and damage accumulation (D1) terms of the JH-2 model, the sphere on glass tile finite element mode developed in section 5.1 was used. To study the effects of the fractured strength on residual velocity, the sphere on glass tile simulations (previously developed) were run with varying fractured strengths (B) for all tested impact velocities were measured. To illustrate the effects of the damage coefficient on the mode of failure, two sphere on glass tile models were run with varying damage coefficient. The effects of interactions between parameters were quantified and suitable parameters were determined such that the developed parameters predicted projectile kinematics and material damage.

To determine suitable values of B and D1 such that they accurately predicted residual velocities, a linear model of the sphere on glass tile simulations was generated such that residual velocities (V) were a function of fractured strength (B) for a given value of the damage coefficient (D1, held constant) The residual velocities and values of B were used to generate a linear model of the sphere on glass impact simulation at the three impact velocities ($V_{100}$, $V_{500}$, $V_{800}$) such that the residual velocity was a function of the fractured strength (B):

$$V_{100} = m_1 B * b_1$$

$$V_{500} = m_2 B * b_2$$

$$V_{800} = m_3 B * b_3$$

Using the set of linear models, the sum squared error (E) of the predicted velocities was minimized using MATLAB to determine the fractured strength, B:

$$E = (V_{100} - V_{exp,\,100})^2 + (V_{500} - V_{exp,\,500})^2 + (V_{800} - V_{exp,\,800})^2$$

## 5.3 Validation of the Soda-Lime Glass Ballistic Model

Once constitutive parameters were finalized, three numerical models based on experimental tests were compared to three sets of experimental data (dynamic Brazilian split Hopkinson bar tests, the sphere on glass tile tests, and the depth of penetration test) to assess the ability of the model to predict various phenomena. The dynamic Brazilian tensile test was used to assess the tensile failure characteristics of the model. The sphere on glass tile ballistic impact experiment was used to verify that the damage development characteristics, since part of the data was used in the parameter identification phase. Finally, the depth of penetration model was used to assess the ability of the model to predict the ballistic performance of soda-lime glass in a complex impact environment.

### Dynamic Brazilian Split Hopkinson Bar Model to Assess Tensile Failure

To assess the tensile behaviour of the model, the split Hopkinson pressure bar model was used to simulate the dynamic Brazilian tests (Figure 56). The split Hopkinson pressure bar apparatus was modelled as a full, 3D model due to the asymmetry of the sample produced by the geometric offset (Figure 41). The incident, transmitter and striker bars were modeled, along with the shims and test sample. The support bearings for the bars were not modeled and the bars were constrained such that the central nodes of both the bars and shims would only translate along the z-axis.

The bars were not expected to undergo plastic deformation and were therefore modelled as elastic (*MAT_ELASTIC) using aluminum elastic properties obtained from literature ($E = 70$ GPa, $\rho = 2703$ kg/m$^3$, $\nu = 0.33$) (Table 13), with a mesh size of 1 mm. Unlike the bars, the shims underwent plastic deformation during testing due to the contact between the sample and the shim. To capture the plastic deformation, the shims were modelled using a Johnson Cook constitutive relation (*MAT_JOHNSON_COOK), with parameters obtained from Kaufmann (2004) (Table 13). The shims were meshed with a 0.5 mm mesh such that the shim mesh matched the mesh of the sample to facilitate contact.

*Table 13: Johnson-Cook parameters for 6061-T6 (Kaufmann, 2004)*

| Johnson-Cook Parameter | *[kg/m³]* | *[GPa]* | *[GPa]* | | | | | | | | | | | | |
|---|---|---|---|---|---|---|---|---|---|---|---|---|---|---|---|
| | Density | Shear Modulus | Young's Modulus | Poisson's Ratio | A | B | n | C | m | $T_m$ | $d_1$ | $d_2$ | $d_3$ | $d_4$ | $d_5$ |
| 6061-T6 | 2703 | 27.6 | 70 | 0.33 | 289.6 | 203.4 | 0.35 | 0.011 | 1.34 | 925.37 | 0 | 0 | 0 | 0 | 0 |

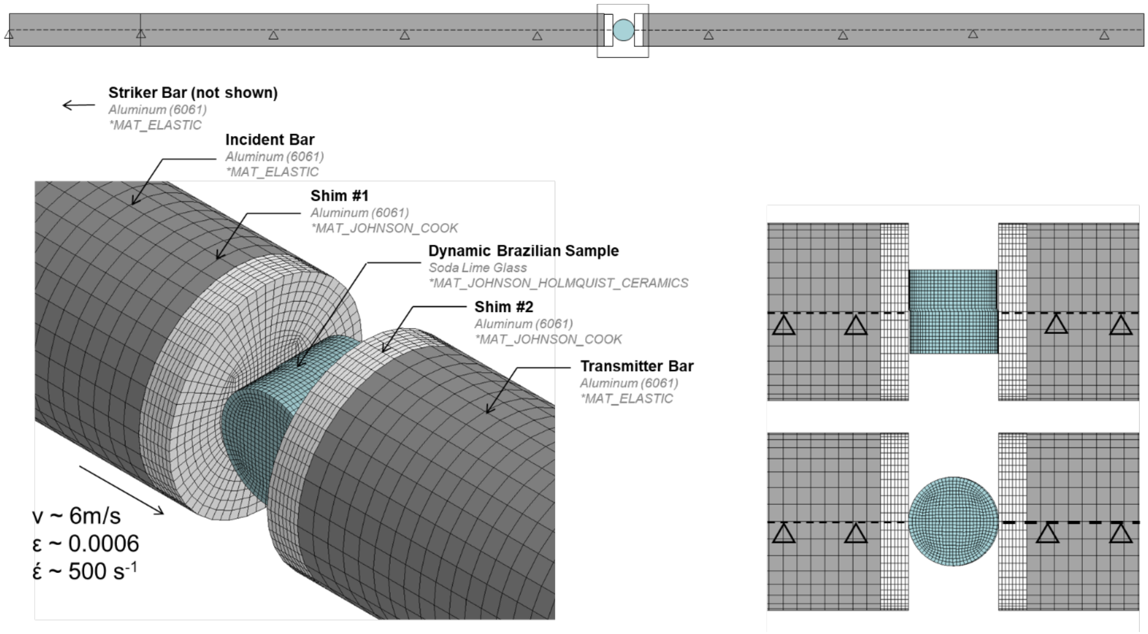

*Figure 56: Split Hopkinson pressure bar apparatus finite element model*

The glass test specimen was modelled with a JH-2 model with a 0.5 mm mesh. A 0.2 mm offset was incorporated into the sample model geometry, to correspond with the sample offset observed in the experiments (Section 4.2).To obtain the bar strains, element strains at elements on the surface of the bar corresponding to the position of the strain gauges were measured at the same sampling frequency used in the tests (1 MHz).

### Sphere on Glass Tile Impact Model to Assess Damage Progression

The sphere on glass tile model used in the validation phase was developed in the previous sections (details of the model can be found in section 5.1). To quantify the progression of the damage front with respect to time in the numerical models, the material damage variable (history variable 2) in a row of elements running from the point of impact to the edge of the target was extracted using a script and post-processed using MATLAB. The damage front was defined as the edge of damaged material (the boundary between visibly damaged and undamaged material) that originated from the point of impact (Figure 57).

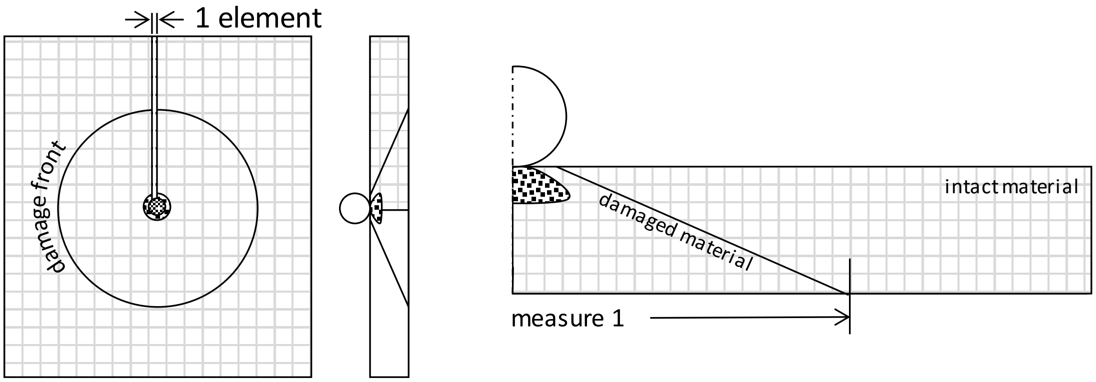

*Figure 57: Schematic of the sphere on glass model showing the comminution and fracture measures*

**Depth of Penetration Test Model to Assess Ballistic Fidelity**

The depth of penetration tests were used to assess the ability of the model to predict the ballistic performance of soda lime glass and combined the numerical methods identified in section 5.1 and the material properties developed in section 5.2. Projectile displacements over time were extracted in experiments using high speed video and video analysis tools and compared to projectile displacements from simulations. Final projectile depths of penetration into the backing material were used as the metric of validation. The simulations were modelled using quarter symmetry due to size of the backing (152.4 mm (6”) in diameter and 304.8 mm (12”) deep) (Figure 58). The geometry near the point of impact (20 mm from the centre) was meshed with a mesh length of 1.0 mm. Outside of this, the mesh was biased radially, transitioning from 1x1x1 mm mesh in the centre to a 4x4x1 mm mesh at the outer edge of the tile (D. Singh, personal communication, 2019).

The projectile model used was previously developed for ballistic impact simulations (Cronin, 2013). The projectile was modelled using quarter symmetry. The AP-M2 projectile model had been previously validated by simulating impacts into aluminum plates and comparing the residual velocity of the projectile in simulation to that of experiments performed by Forrestal et al. (2009).

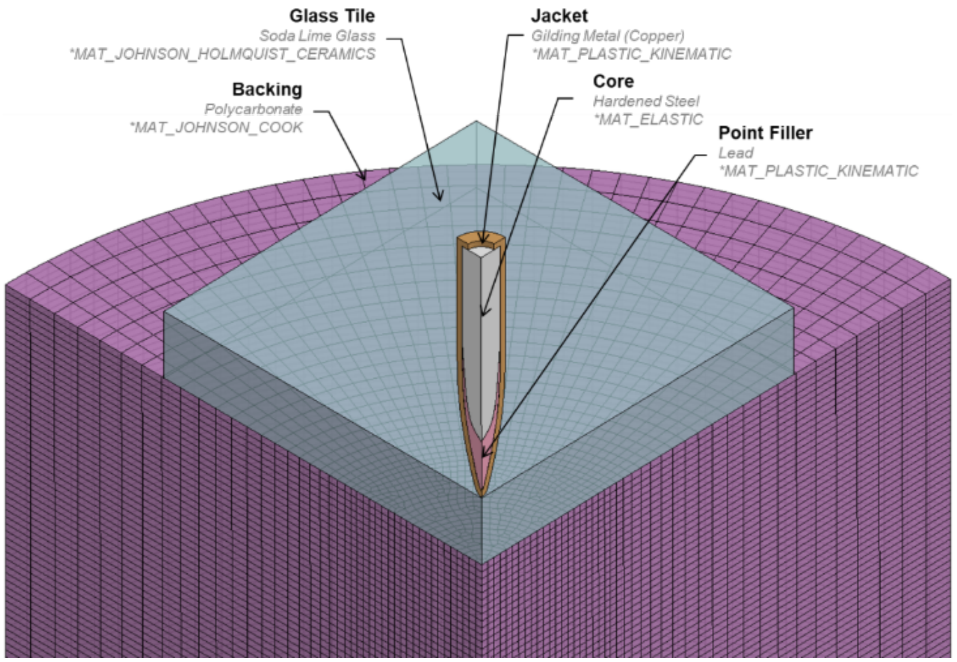

*Figure 58: Depth of penetration quarter model with glass and AP-M2 projectile*

The polycarbonate model was developed in parallel with the soda-lime glass model tile (D. Singh, personal communication, 2019). The polycarbonate model used a Johnson-Cook constitutive model and parameters were determined using coupon level stress-strain data at various rates of deformation and temperatures and validated using the depth of penetration data from bare polycarbonate tests (D. Singh, personal communication, 2019) (Table 14).

*Table 14: Johnson-Cook parameters for polycarbonate (D. Singh, personal communication, 2019)*

| Johnson- Cook Parameter | [kg/m³] Density | [GPa] Shear Modulus | [GPa] Young's Modulus | Poisson's Ratio | A | B | n | C | m | $d_1$ | $d_2$ | $d_3$ | $d_4$ | $d_5$ | $T_m$ | Cp |
|---|---|---|---|---|---|---|---|---|---|---|---|---|---|---|---|---|
| Polycarbonate | 1190 | 0.986 | 2.38 | 0.344 | 72.5 | 78.9 | 2.0 | 0.04 | 1.05 | 0 | 0 | 0 | 0 | 0 | 443 | 1250 |

Due to computational constraints, the polycarbonate backing material could not be meshed finer than 1.0 mm and mesh convergence at this mesh resolution could not be verified. The purpose of the polycarbonate backing material in this study was to act as a witness material (i.e.: provide an indication of the energy absorbed by the facing material in a consistent manner) and provide some level of confinement for the glass tile. To this end, a combination of element mesh size (1.0 mm) and erosion criteria were determined and verified against experimental data to ensure that the model predicted the depth of penetration with reasonable accuracy (Figure 59) over the velocity range used in this study. The polycarbonate model predicted depths of penetration within 10% for both the 500 m/s and 930 m/s impact cases, but under predicted depth of penetration in the 750 m/s impact case by a larger margin (14% difference) (Figure 60).

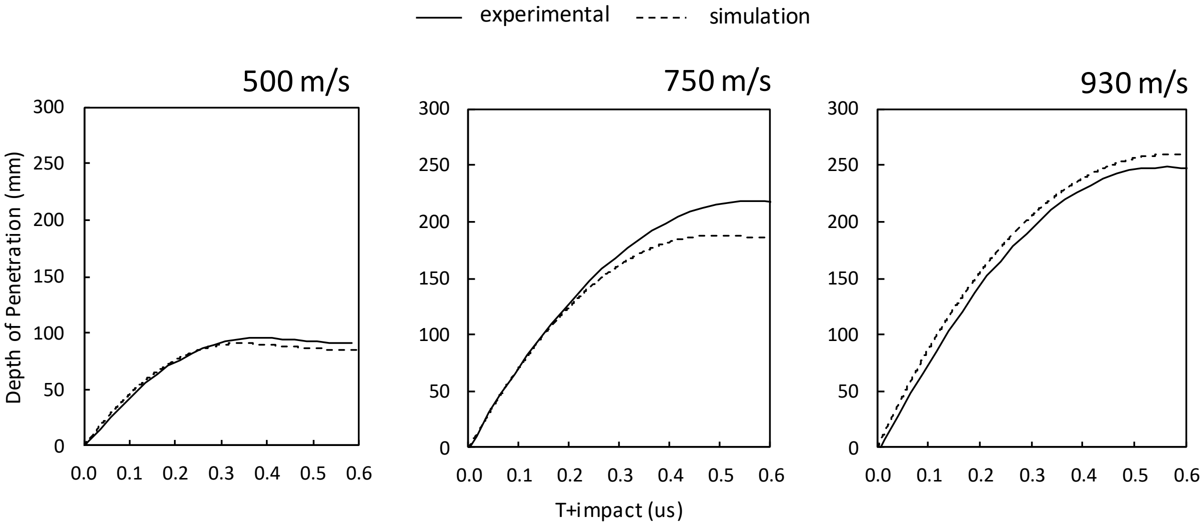

*Figure 59: Depth of penetration versus time at three impact velocities of bare polycarbonate (experiment and simulation)*

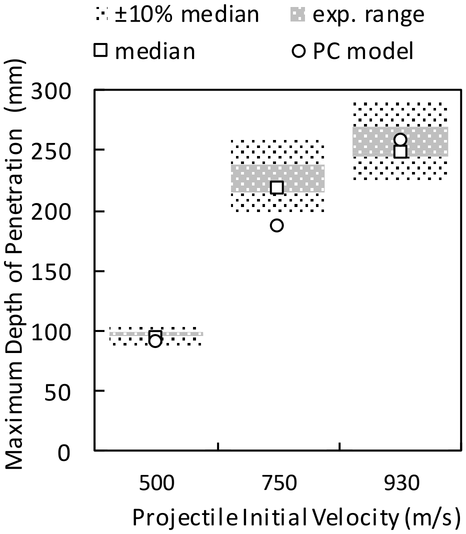

*Figure 60: Bare polycarbonate impacts with APM2 projectiles at three velocities, final depth of penetration experimental ranges versus simulated*

The glass tile was modelled using a JH-2 model with material parameters determined through the parameter identification process (section 5.2). The sample was meshed with a 0.5 mm mesh as determined from the SOG mesh convergence study (section 6.1.1). In cases where glass tiles were being tested (as opposed to polycarbonate only tests), the glass tile was affixed to the polycarbonate backing via cohesive elements to simulate the film adhesive (D. Singh, personal communication, 2019). The backing material was not supported. The three test velocities (500, 750, 930 m/s) were simulated and the depth of penetration was measured by extracting the displacement of the projectile core from the simulation (*DATABASE_MATSUM) and offsetting by the initial distance of the core from the surface of the polycarbonate backing, corresponding to the experimental measurement methodology. The core displacements were extracted at a frequency of 1 MHz. At the maximum test velocity of 930 m/s, a sampling frequency of 1 MHz would provide displacement samples under one millimeter apart providing adequate resolution to measure depths of penetration into the polycarbonate backing and greater than the 50 kHz sampling frequency provided by the depth of penetration high speed video analysis.

# 6. Numerical Results and Discussion

## 6.1 Assessment of Grid Convergence and Model Stability

Verification of the model was performed three phases. First, the discretization error of the sphere on glass finite element model was estimated using the grid convergence index and published glass properties from Johnson and Holmquist (1995). The finite element model was compared to two models that utilized mesh-free methods (SPH, EFG) with respect to their ability to predict projectile kinematics and damage development (ballistic fidelity) as well as their convergence tendencies. Lastly, a more aggressive impact with multiple projectile impacts was run to assess the robustness of the model under a multi-hit impact.

### 6.1.1 Assessment of Discretization Methods Used to Model Ballistic Impact

The sphere on glass tile impacts were used to assess the predictive capability of the numerical methods. Using a medium mesh density (0.5 mm element length), all three solution methods behaved similarly to the sphere on glass experiments, showing two distinct regimes: non-perforating where the projectile rebounded off the target and perforating where the projectile passed through the target (Figure 61) using published material properties. Both SPH and EFG predicted a perforation velocity similar to the experimental tests (550 m/s), while the finite element model over-predicted the perforation velocity (closer to 650 m/s). All models under-predicted the residual velocity of glass when the projectiles rebounded and over-predicted the residual velocities when the projectile.

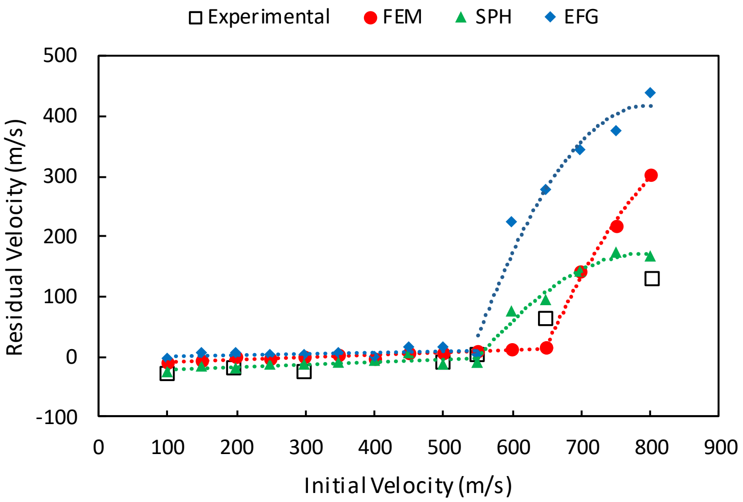

*Figure 61: SOG projectile kinematics for three discretization methods, using 0.5mm mesh and published glass material properties*

All simulations showed some features of planar impact such as material comminution and partial penetration of the target. All solution methods under predicted the amount of damage accumulated during impact over all velocities (100 m/s – 800 m/s), when compared to the corresponding experiments. The three simulations were compared at 300 m/s, where most of the discrete fracture features were present in the sphere on glass tile experiments (Figure 62). In the experiments, the impacts at 300 m/s produced 31 radial cracks, partial concentric cracking, edge cracks, and resulted in a damaged zone 62 mm in diameter (more than half the width of the tile).In contrast, all simulation methods predicted some comminution at the point of impact, but only SPH predicted the ejection of material and tensile cracking at 300 m/s, and even then, the damage was localized and did not extend past the mesh-free zone.

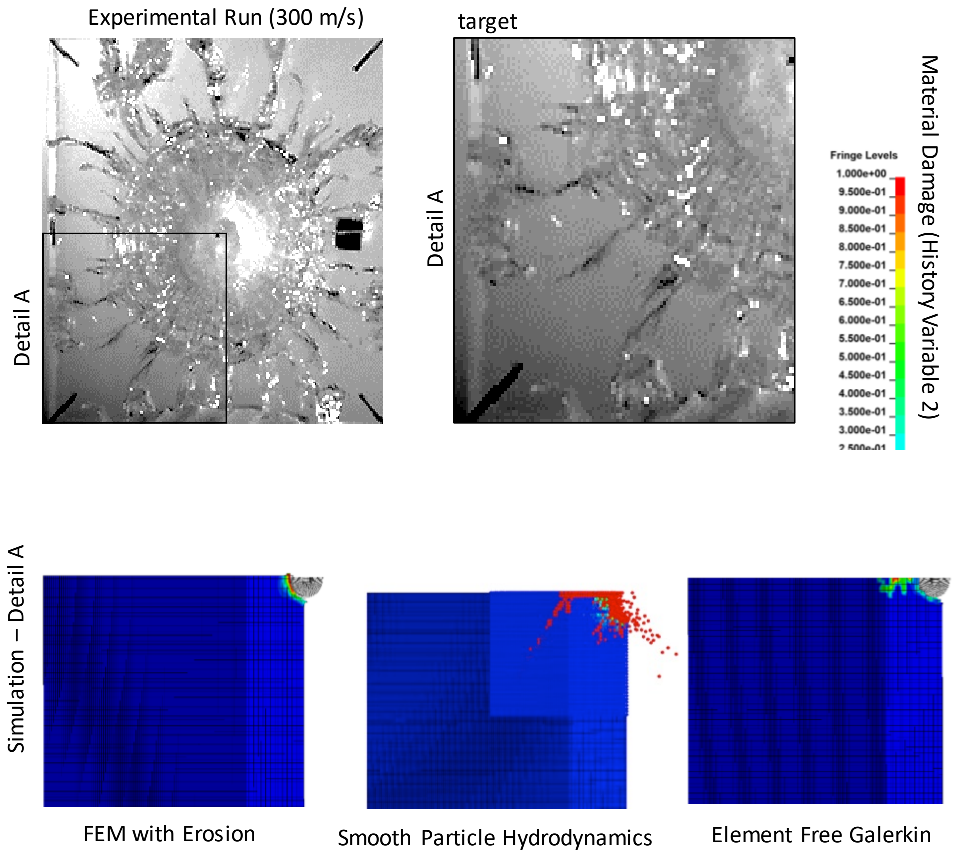

*Figure 62: Predicted material damage for three solution methods at 300 m/s impact velocity*

## Mesh Convergence of the Finite Element Model

The residual velocities from the coarse (1.00 mm), medium (0.50 mm) and fine (0.25 mm) meshes were used to perform the Richardson extrapolation to estimate the residual velocity of a converged solution (mesh size approaching 0). For the sphere on glass finite element model the Richardson extrapolated (RE) residual velocity at 800 m/s was calculated to be 351 m/s (Table 15). The calculated order of convergence was 1.88, lower than theoretical rate of convergence of 2.0 (for displacements) for a linear hexahedral element (Braess, 1997), but expected due to the discontinuities present in ballistic impact simulations (cracking, contact, shock) (Roache, 1993). The extrapolated residual velocity was used to compare the residual velocity at each mesh size to determine how close it was to the extrapolated solution.

The medium mesh (characteristic length of 0.5 mm) of the finite element model predicted a residual projectile velocity of 313 m/s (11% lower than the RE solution of 350 m/s). The percentage difference between the residual velocity of the extrapolated solution and the simulated residual velocities converged at increasing mesh densities. There was a trade-off between solver time and level of mesh refinement (Figure 63), for simulations run on 6 cores of an Intel i7-6850 (3.60 GHz clock speed). The medium mesh provided a good balance between simulation runtimes and discretization error, resulting in an estimated discretization error of less than 10% and runtimes of under one hour. At a mesh size of 0.35 mm (2.86 relative mesh size), the relative error reduced to less than 5%.

*Table 15: Simulated residual velocity of SOG models at 800 m/s impact velocity at varying mesh densities*

| Mesh Length | Relative Length | Residual Velocity (m/s) | Percentage Difference (vs. RE) |
|---|---|---|---|
| **(C) 1.00** | **1.00** | **210.2** | 40% |
| 0.80 | 1.25 | 190.0 | 46% |
| 0.60 | 1.67 | 253.8 | 28% |
| **(M) 0.50** | **2.00** | **312.6** | 11% |
| 0.40 | 2.50 | 311.4 | 11% |
| 0.35 | 2.86 | 336.9 | 4% |
| 0.30 | 3.33 | 371.3 | 6% |
| **(F) 0.25** | **4.00** | **340.3** | 3% |
| Richardson Extrapolation (RE) | - | 350.6 | - |
| Experimental | - | 129 | - |

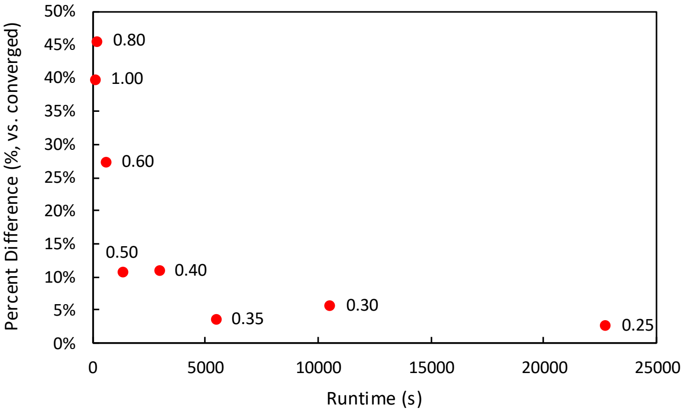

*Figure 63: Percentage difference from convergend solution versus simulation runtimes (6 cores, Intel i7-6850 @ 3.60GHz)*

### Comparing Convergence Tendencies of All Solution Methods

A mesh convergence study was also performed to assess convergence of the different solution methods (Figure 64). Orders of convergence and grid convergence indices were calculated based on the Richardson extrapolation at 1.00 mm, 0.50 mm and 0.25 mm solutions (Table 16).

SPH predicted projectile residual velocities with some accuracy (difference in residual velocities as low as 15% at lower impact speeds) but had a low rate of observed convergence (p = 1.1). For comparison, a similar convergence study performed by Schwer (2009) of an aluminum projectile impacting an aluminum target had an observed rate of convergence of 1.65. In some cases, the relative error (with respect to the Richardson extrapolated solution) increased with increasing mesh refinement, indicating that discretization error was not the main source of error in the SPH simulations. One source of numerical error that may have caused the poor convergence are contact errors. However in the explicit solver used in this study, SPH to SPH contact was handled internally (as opposed to a dedicated *CONTACT definition), so contact statistics (like contact force, and sliding interface energy) could not be extracted. Unlike SPH, EFG presented higher rates of convergence (p = 2.1) but did not predict residual velocities accurately (differences as high as 348%). FEM showed acceptable convergence tendencies with a rate of observed convergence of 1.88. Although SPH predicted ballistic performance more accurately than FEM or EFG using literature parameters, the SPH did not converge over the mesh range of study indicating discretization error was not the main source of numerical error. The finite element model with erosion provided a good balance between simulation accuracy and runtimes in the sphere on glass tile models, provided that a sufficiently fine mesh was used (determined to be less than 0.5 mm).

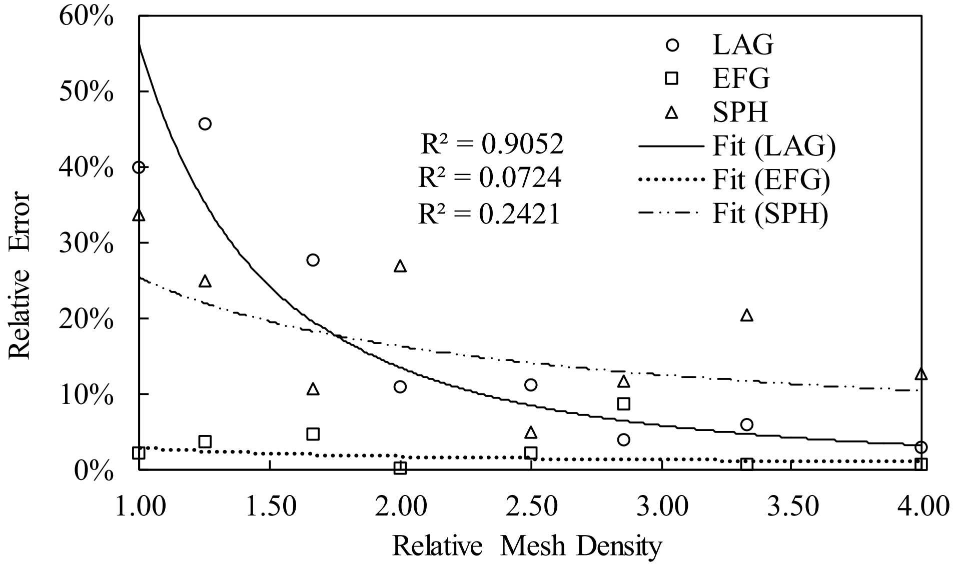

*Figure 64: Discretization error of three solution methods with respect to converged solution*

*Table 16: Richardson extrapolation for each discretization method at 800 m/s*

| | | FEM | EFG | SPH* | |
|---|---|---|---|---|---|
| projectile residual velocity | coarse (3) | 210 | 438 | 166 | [m/s] |
| | medium (2) | 313 | 447 | 183 | |
| | fine (1) | 340 | 445 | 219 | |
| | p | 1.883 | 2.1 | 1.1 | |
| | $e_{12}$ | -0.082 | 0.005 | -0.196 | |
| | $e_{23}$ | -0.327 | -0.021 | -0.093 | |
| | $GCI_{12}$ | 0.030 | 0.001 | 0.175 | |
| | $GCI_{23}$ | 0.122 | 0.006 | 0.083 | |
| | Richardson Extrapolation (residual velocity) | 351 | 444 | 252 | [m/s] |

**SPH diverges between the three grid sizes*

### 6.1.2 SOG Model Robustness Assessed by Varying Impact Location and Multi-Hit Simulation

Up to this point, the sphere on glass model had only been run with the projectile impacting at the geometric centre of the tile that resulted in a node-node correspondence of the sphere and tile meshes. However, a ballistic model may be impacted anywhere along the tile and should be able to provide consistent results without numerical instabilities. The off-centre produced some variability in the predicted projectile velocities of the sphere on glass model. At very small eccentricities (0.1 mm), the residual velocity was much lower than a central impact (at the origin, Table 17). After some investigation, it was determined that the small imposed offset produced an irregularity in the contact, resulting in uneven element loading. This error was reduced by turning on the consistency flag in the *CONTROL_PARALLEL card in SMP DYNA, a setting that is recommended by the user manual (LSTC, 2014), but not the default option. This discrepancy was only present in the 0.1 mm test case, with the other eccentricities showing percentage differences of less than 5% of the measured residual velocity.

*Table 17: Off-centre hits test results*

| eccentricity *[mm]* | Y-axis *[m/s]* | Y-axis CONSISTENTCY FLAG OFF *[% diff]* | Y-axis CONSISTENTCY FLAG ON *[% diff]* |
|---|---|---|---|
| 0 | -313 | 0% | 0% |
| 0.1 | -290 | **7%** | **2%** |
| 0.5 | -305 | 2% | 4% |
| 1 | -310 | 1% | 1% |
| 5 | -306 | 2% | 3% |
| 10 | -308 | 2% | 4% |

A multi-hit simulation was run to assess the model over longer runtimes and with a more aggressive impact (Figure 65) to confirm simulation stability (no error termination due to highly distorted elements or other numerical instabilities). The model was run for 500 μs to assess model stability at longer runtimes. The simulation ran to completion successfully. No experimental multi-hit tests were available to assess the accuracy of this model.

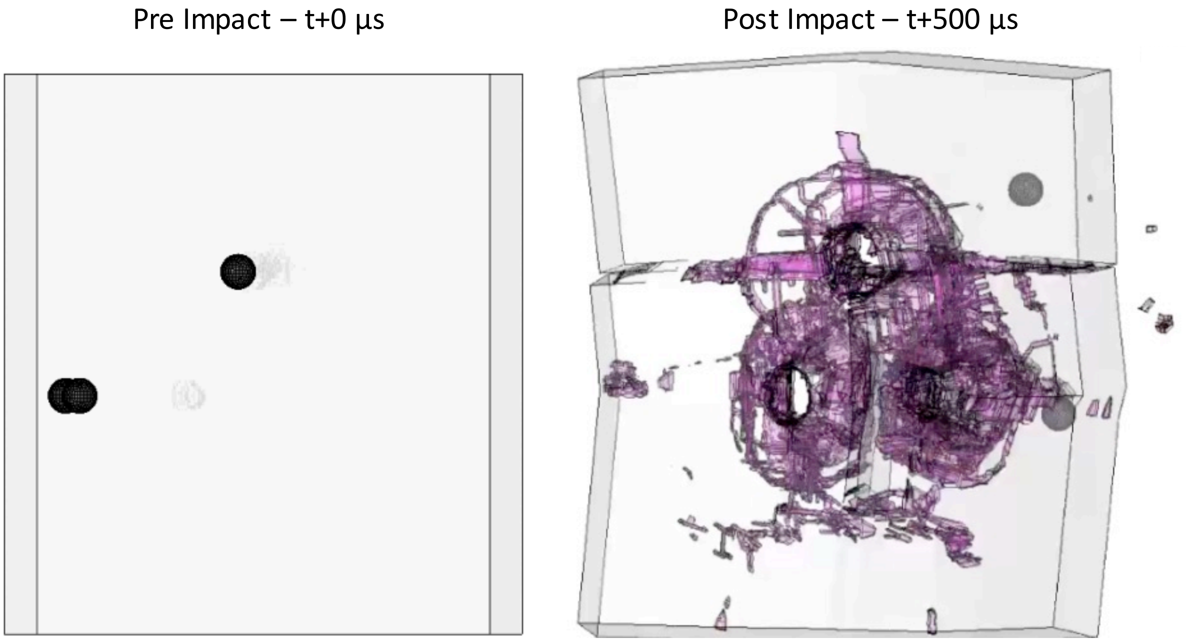

Pre Impact – t+0 µs

Post Impact – t+500 µs

*Figure 65: Multi-hit simulation, three spheres impacting single glass tile at 800 m/s at 500 µs after impact (impact side shown), material damage (history variable 2) greater than 0.5 plotted in purple*

All solution methods predicted projectile kinematics with some accuracy. SPH predicted projectile residual velocities with difference in residual velocities as low as 15% at lower impact speeds but had poor convergence tendencies (p = 1.1). EFG had much higher rates of observed convergence (p = 2.1) but did not predict residual velocities well, with projectile velocity differences as high as 348% using literature parameters. FEM showed a rate of observed convergence (p) of 1.88, a value lower than the theoretical rate of convergence for the hexahedral elements used in this study (p = 2) but expected due to the discontinuities (contact, fracture, shock) present in ballistic impact modelling. Although other solution methods predicted ballistic performance more accurately using literature parameters, the methods showed poor convergence tendencies (SPH) or too computationally expensive (EFG) to use effectively. A finite element model with erosion provided a good balance between simulation accuracy and runtimes, provided that a sufficiently fine mesh was used (determined to be less than 0.5 mm). FEM was also shown to be numerically robust, and able to handle a multi-impact simulation over an extended period of time.

## 6.2 Soda-lime Glass Constitutive Model Parameter Identification

Following an initial assessment of discretization methods using published material properties, the constitutive model strength parameters (A,N,T,B,m,$SF_{MAX}$, Equation 4 & Equation 5) and damage evolution parameters (D1,D2, **Error! Reference source not found.**) were updated with the goal of improving the ability of the soda-lime glass model to predict projectile kinematics and material damage. The parameter identification process was performed in two steps. Initially, least square regression were used to fit experimental pressure-stress data (Dannemann et al., 2011) to the JH-2 strength model. Once an initial fit was assessed, a combination of analytical methods and experimental data (sphere on glass tile tests) were used to improve the ability of the model to predict projectile kinematics and material damage. The parameter calibration process produced a model that could accurately predict both projectile kinematics and damage progression in the sphere on glass tile tests.

To better assess the fractured strength behaviour (B) and damage evolution parameters (D1) of the JH-2 model, the sphere on glass tile impacts were used. Projectile kinematics (residual projectile velocities) were used to study the effects of the fractured strength behaviour (B). Damage progression in the 100 m/s sphere on glass impact (initial velocity 100 m/s) was used to assess the effects of the rate of damage accumulation (D1) on the damage mechanisms that the model predicted. It was determined that slower rates of damage accumulation (D1 = 0.08) allowed the material directly under the projectile to comminute and allowed for a fracture cone to form (as seen in experiments). Faster rates of damage accumulation (D1 = 0.00) resulted in sudden failure of material through discrete cracking and resulted in the target to fail in an unrealistic manner. A parametric study was performed to study the effects of the interactions of these two parameters on the residual velocity of the projectile and to determine suitable values of B and D1. The final model accurately predicted projectile kinematics and damage progression in soda-lime glass in the sphere on glass tile impact experiments.

### 6.2.1 Least Squares Regression Fitting of JH-2 Strength Parameters

Least squares regression techniques were used to fit the pressure-strength data (Dannemann et al., 2011) to the intact (A,N,T) and fractured strength curves (B,M,$SF_{max}$) of the JH-2 model. The updated curves fit the pressure-strength data were in good agreement with the experimental data ($r^2 = 0.921$ for the intact strength curve, $r^2 = 0.996$ for the fractured strength curve) (Figure 66).

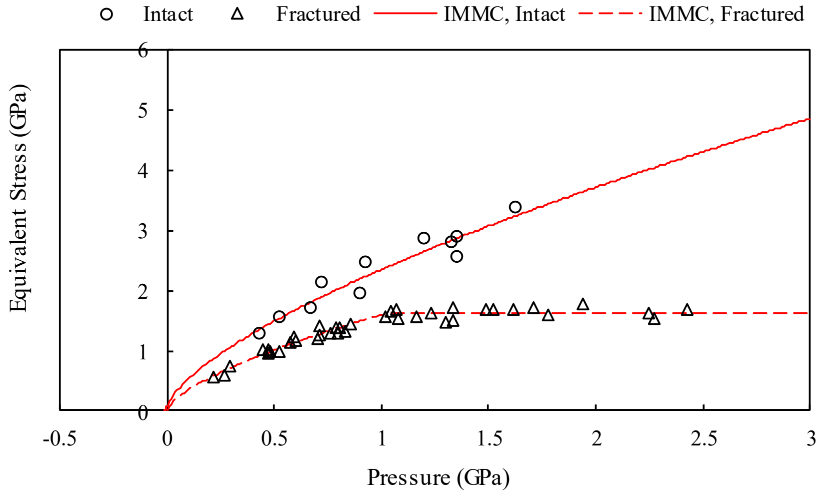

*Figure 66: Updated pressure-strength curves compared to literature data.*

*Table 18: Updated model parameters (IMMC-V1) based on least square fitting*

| | *Bulk* | *Fractured Strength* | | | *Damage* | | *Intact Strength* | | | *S.Rate* | *Equation of State* | | | *Shock* | | *Elastic* | |
|---|---|---|---|---|---|---|---|---|---|---|---|---|---|---|---|---|---|
| *Units* | - | - | - | - | - | - | - | - | MPa | - | | GPa | | GPa | | $kgm^{-3}$ | GPa |
| *Symbol* | β | B | m | $SF_{max}$ | D1 | D2 | A | n | T | c | K1 | K2 | K3 | HEL | PHEL | ρ | G |
| JH-1995 | 1 | 0.2 | 1 | 0.5 | 0.043 | 0.85 | 0.93 | 0.77 | 150 | 0.003 | 45.4 | -138 | 290 | 5.95 | 2.92 | 2530 | 30.4 |
| V1 | 0 | **0.77** | **0.66** | **0.36** | 0.043 | 0.85 | **1.05** | **0.66** | **6.7** | 0 | 45.4 | -138 | 290 | 5.95 | 2.92 | 2530 | 30.4 |

### 6.2.2 Limitations of Using Coupon-Level Testing to Fit Parameters for a Ballistic Impact Model

The IMMC-V1 set of parameters were used in the sphere on glass tile ballistic model to assess the fit parameters in a ballistic impact test case. Both simulated damage propagation at a single test velocity and residual velocities were compared to experiments. The IMMC-V1 parameters over-predicted the extent of damage in the glass tile, even at low impact velocities (Figure 67). The model also over-predicted projectile velocities across the entire test range (impacts ranging from 100 m/s to 800 m/s) (Figure 68).

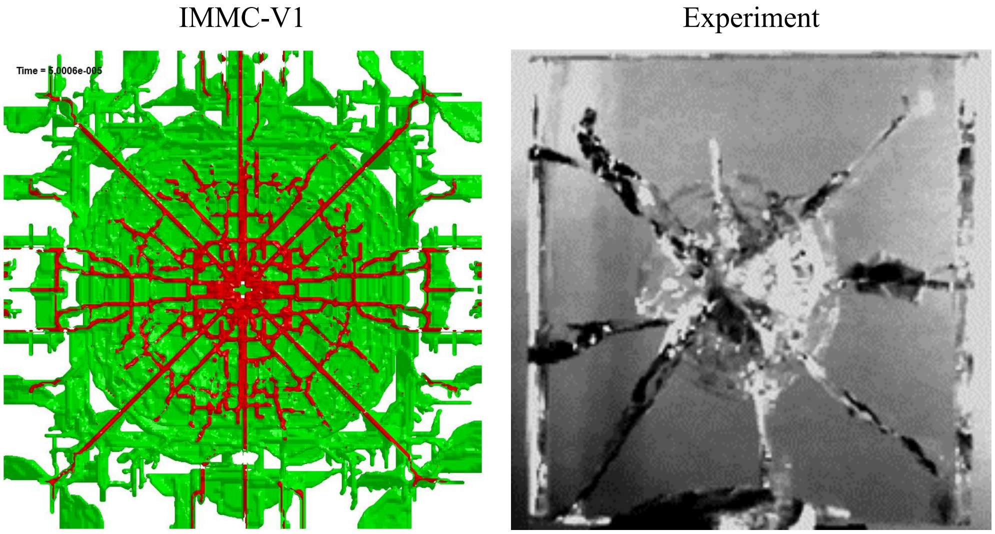

*Figure 67: Damaged glass tile simulation, 100 m/s sphere impact (reverse side pictured, IMMC-V1).*

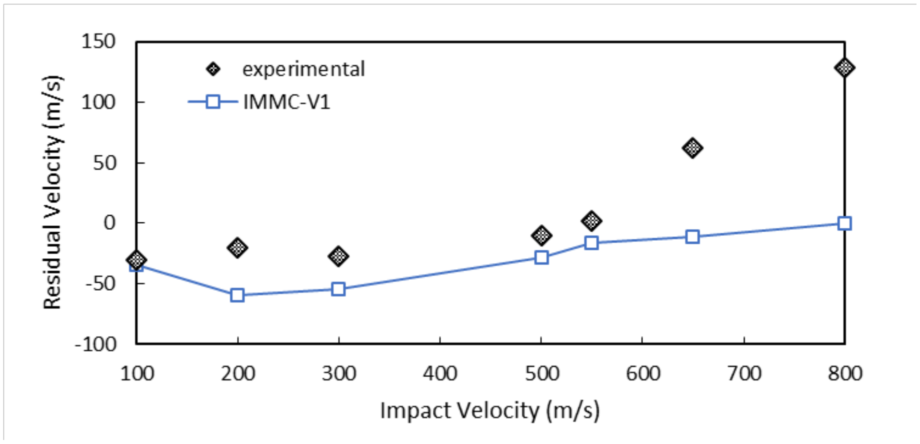

*Figure 68: Sphere on glass projectile kinematics simulation (IMMC-V1) versus experiments.*

Using quasi-static data to fit the fully fractured strength terms (B,M,$SF_{max}$), tensile strength (T) and the damage terms (D1, D2) is not typically performed, since the comminution process is strain rate dependent (section 2.2) and is usually determined through dynamic testing. Johnson and Holmquist (1995) state in their work that they did not use direct experimentation to determine the fractured strength and damage terms. In their words:

> *"Different techniques have been investigated by various researchers, but questions remain as to their validity {...}. Here, a computational iterative technique has been developed to obtain the hydrostat, damage model, and fractured material strength using results from flyer plate impact tests and ballistic tests."*

Although the fitting process alone was not enough to determine the JH-2 parameters for a ballistic impact model of soda-lime glass, IMMC-V1 parameters provided an experimentally based foundation for model development. From here, parameters could be updated such that they could model a ballistic impact event. The sphere on glass tests above identified two limitations in the IMMC-V1 set of parameters. First, the IMMC-V1 parameters over-predicted the amount of tensile damage sustained in the tile during impact. Second, the IMMC-V1 set of parameters over-predicted the residual velocities in the sphere on glass impacts and therefore under-predicted the energy absorbed in the simulation. An element under confined compression would undergo three phases of loading (elastic loading, material damage and fully comminuted, Figure 7). To decrease the energy absorbed in the loading process, the rate of damage accumulation can be increased or the fully fractured strength can be decreased (B). Damage accumulation is controlled by two terms D1 (damage coefficient) and D2 (damage exponent). To simplify the model development process, D2 or the pressure dependence of damage accumulation was assumed to be zero and D1 was used to control the rate of material damage accumulation in the model (Figure 69).

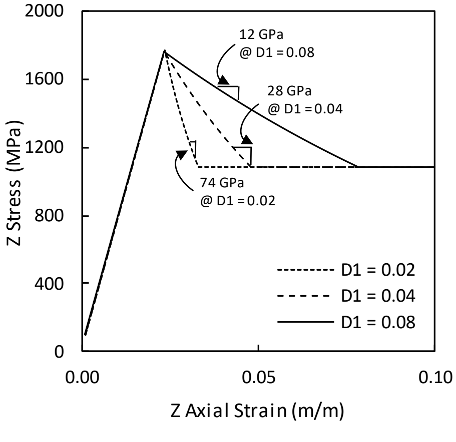

*Figure 69: The effect of damage coefficient (D1) on the rate of damage accumulation in confined compression*

### 6.2.3 Tensile Strength Correction Using Conservation of Energy

One issue identified with the fit parameters was the handling of tensile fracture in the model. It was determined that IMMC-V1 parameters over-predicted the level of tensile damage sustained by the tile, and the energy absorbed during tensile fracture was not consistent with the energy constraints proposed by Grady (1973). Consider a finite element of 0.5 x 0.5 x 0.5 mm placed under uniaxial tension. Under increasing tension, the element will eventually fail at a time, $t_{fail}$. If energy is conserved in the element, the energy in the element before fracture (strain energy) should equal the energy in the element after fracture (surface energy) (Figure 70).

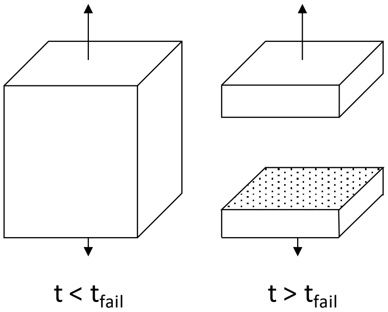

*Figure 70: Element before and after fracture*

Assuming the element behaves in a linear-elastic manner, constant stress throughout the element and no damage up until fracture, the strain energy in the element is equal to the following (Hibbeler, 1997):

$$U = \frac{1}{2}\frac{V}{E}\sigma^2 \qquad \text{Equation 13}$$

where U is the strain energy in joules, V is the element volume in meters cubed, E is the Young's modulus in Pascals, and $\sigma$ is the equivalent stress in the element. Given the properties of glass (E = 70 GPa, $\sigma_Y$ = 30 MPa) and the volume of the element ($V = L^3 = (0.5\text{x}10^{-3}\text{ m})^3 = 1.25\text{x}10^{-10}\text{ m}^3$) the strain energy to fracture was calculated to be 0.36 μJ (Equation 13). This is the strain energy in the element just prior to fracture.

Using Grady's (1983) surface energy equation (Equation 1), the energy after fracture (energy required to produce the fracture surfaces) can be determined. Given the properties of glass ($K_{IC}$ = 0.7 MPa $m^{1/2}$, ρ = 2530 kg/$m^3$, c = 5450 m/s) and the fact that two (2) surfaces of area $2.5\text{x}10^{-7}\text{ m}^2$ are produced upon fracture, the calculated energy associated with the production of the two surfaces is 2.11 μJ.

Therefore, the current parameters under-predict the amount of energy required to produce a crack by almost five fold (x 5.86), an over-prediction is consistent with the observations made in the sphere on glass tile models. By using the amount of energy required to form two free surfaces (2.11 μJ), the corresponding yield strength can be solved using the strain energy equation, the JH-2 pressure strength relation and the fit parameters such that it conserves energy. The calculated strain energy at fracture (2.11 μJ) can be substituted into the strain energy equation (with the elastic properties of glass) and results in a tensile strength of 48.6 MPa. In uniaxial tension, the hydrostatic pressure is one third the uniaxial stress, or 16.2 MPa. The yield strength and the hydrostatic pressure can then be substituted into the JH-2 intact strength curve and the hydrostatic tensile pressure (T) to failure can be determined. If the current values of strength are used ($A = 1.0492$, $n = 0.6965$), the tensile pressure (T) equals 28.2 MPa. However, changing the hydrostatic tensile pressure parameter (T) without simultaneously changing A and n will affect the intact strength fit of the JH-2 model by shifting the curve on the pressure axis. To conserve energy and maintain the fit to experimental pressure-strength data, a single element test was placed in uniaxial tension and loaded until fracture. Different models with increasing values of T and the corresponding A and n values (determined through fitting) were run until the maximum strain energy in the model equaled the theoretical strain energy at fracture (2.11 μJ). Using this procedure, T was found to be 21 MPa. The resulting strength (A,N,T,B,M,$SF_{max}$) and damage (D1, D2) terms were identified as material model coefficients IMMC-V1 (Table 19).

### 6.2.4 Determining Fractured Strength (B) and Damage Evolution (D1) Terms through Sphere on Glass Tile Impacts

Once an initial set of JH-2 parameters (IMMC-V1) were fit and assessed using single element models, the sphere on glass tile data set was used to improve the ability of the model to predict projectile kinematics by modifying the fractured strength (B) and damage accumulation rate (D1) in the model. For the given set of intact strength, fractured strength and damage terms (IMMC-V1), the fractured strength (B) primarily affected the residual projectile velocities. The damage accumulation term (D1) affected the mode of failure in the sample. There was some interaction between fractured strength (B) and damage accumulation (D1) on the projectile velocity. To determine a B and D1 such that the model predicted projectile kinematics accurately, a parametric study was used generate a linear model of the residual velocities in the sphere on glass tests with respect to fractured strength. The predicted error in the model was minimized to determine a suitable combination of B and D1.

### The Effect of Fractured Material Strength (B) on the Sphere on Glass Tile Model Residual Velocity

To assess the effects of the fractured strength on projectile residual velocities, the sphere on glass tile models were run at all tested impact velocities (100 to 800 m/s) and residual velocities were compared to experiments. The IMMC-V1 set of parameters over predicted projectile velocities of the entire range of the sphere on glass impact study (Figure 71). Previous results (single element testing, section 6.2.2) indicated the IMMC-V1 set of parameters over predicted the fully fractured strength (strength when material damage or D = 1) of the material. Reducing the fractured strength of the material (B) improved the ability of the model to predict projectile kinematics (Figure 71).

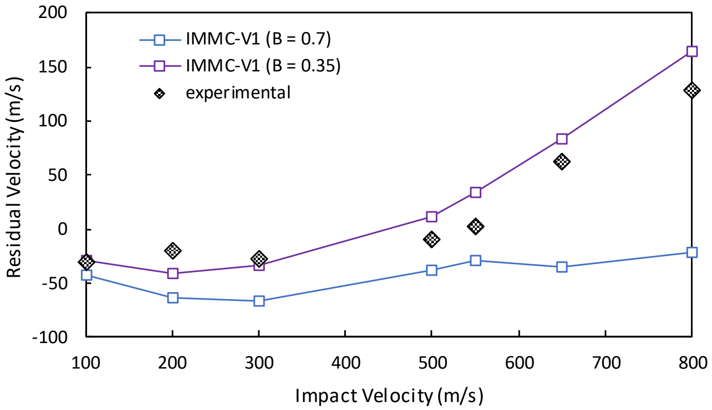

*Figure 71: Simulated (IMMC-V1) versus experimentalresidual velocities at varying fractured strength (B)*

### Effect of the Damage Coefficient (D1) on the Sphere on Glass Tile Model Damage Propagation

To illustrate the effects of the damage coefficient on the accumulation of material damage in the sphere on glass model, two sphere on glass impact models were run at an impact velocity of 100 m/s; one model with damage accumulation turned off (D1 = 0.00, Case A) and one model with slower rate of damage accumulation (D1 = 0.08 or twice the rate of damage accumulation in the JH-1995 case, Case B). By turning off damage accumulation in case A (D1 = 0.00), the material immediately assumes a fully fractured state once the intact strength of the material was exceeded. To assess the effects of these models, a cross-section of the model was taken and damage progression at the point of impact was examined over 3 µs (Figure 73).

Changing the rate of damage accumulation from 0.00 to 0.08 resulted in two distinct modes of failure. These different failure modes also affected projectile kinematics (Figure 72). The initiation of failure (either through comminution or tensile failure) was visible in the acceleration versus time graphs, making these graphs a potentially useful tool in the future development of models.

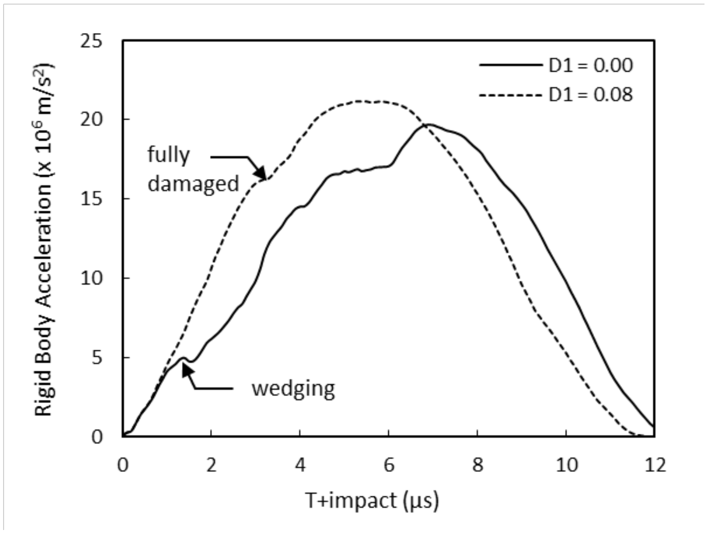

*Figure 72: Acceleration versus time profiles of projectile for case A (D1 = 0.00) and B (D1 = 0.08)*

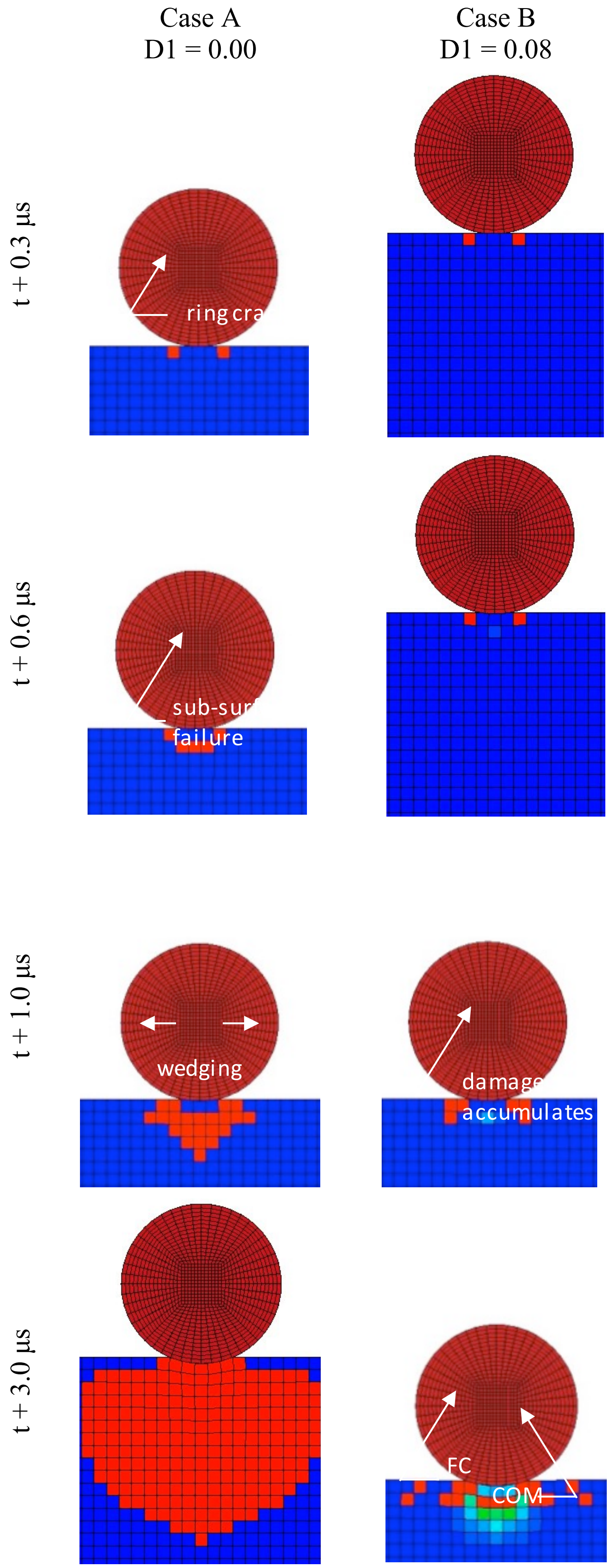

*Figure 73: Damage accumulation during impact phase with varying D1 (Vo = 100 m/s)*

In case A (D1 = 0.00, Figure 73, left) , a ring crack formed early on in the impact (t + 0.3 µs). At t + 0.6 µs, subsurface failure initiated as a result of internal compressive stresses. The material under the projectile failed immediately, and acted as a point of crack initiation. At t + 1.0 µs radial cracks formed from the initial subsurface crack. The projectile continued to penetrate into the target, effectively wedging the target apart (t + 3.0 µs). The cracks relieved any tensile stresses in the material caused by the contact and disrupted the formation of a fracture cone.

In case B (D1 = 0.08, Figure 73, right), a ring crack formed early on in the impact (t + 0.3 µs). At t + 0.6 µs, subsurface failure initiated as a result of internal compressive stresses. The material did not fail immediately. Instead, the material under the projectile pulverized (t + 1.0 µs) and formed a bulb of comminuted material (COM) (t + 3.0 µs). A series of ring cracks extended outward around the bulb of comminution, forming a fracture cone (FC).

### Combined Effect (Interactions) of B and D1 on the Sphere on Glass Tile Impact Model

To study the effects of B and D1 (and their interactions) on the projectile kinematics in the sphere on glass impacts, a parametric study was performed. Combinations of three fractured strength coefficients (B) and two damage coefficients (D1) were studied at three impact velocities using the sphere on glass tile model. The two damage coefficients (D1) used were 0 (no damage accumulation) and 0.08 (roughly half the rate of damage accumulation used in JH-1995). The three fractured strength coefficients (B) used were 0 (no strength at a fully damaged state), 0.5 (an intermediate strength) and 1 (effectively as strong as intact glass). Three projectile velocities (100 m/s, 500 m/s and 800 m/s) were used to study the effects of these parameters at a non-penetrating, transition and penetrating case, respectively. In total 18 simulations were run (Figure 74).

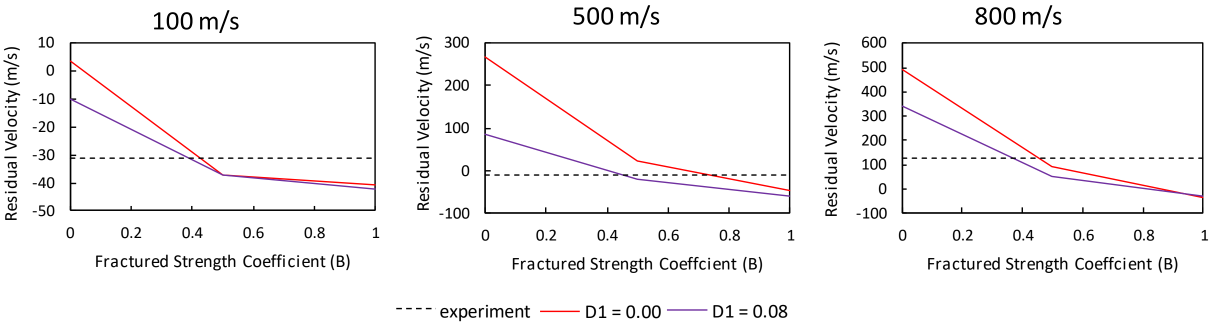

*Figure 74: Parametric study to assess the effects of B and D1 on SOG residual velocities.*

The effect of the damage coefficient (D1) on residual velocity changed with increasing fractured strength (B). The damage coefficient (D1) controlled the rate of the transition from the fully intact material (D = 0) to the fully fractured strength (D = 1) of the material. With increasing fractured strength (B), the intact and fractured strength curves converged so that the intact and fractured strengths were similar for B=1.

Using the parameter study (Figure 74), there was likely a range of possible fractured strengths (B) and accompanying damage coefficients (D1) that would predict the residual velocities seen in the sphere on glass impact experiments. However, without adequate experimental data, fitting both B and D1 using the sphere on glass data alone would be a calibrated solution using inverse methods. Since the upper bound of the damage coefficient used in this investigation (D1 = 0.08) was able to predict the mode of failure in the sphere on glass targets at 100 m/s (Figure 73), this higher damage coefficient was considered. Using the parametric study above, a test range for B was identified (Figure 74, right) (B = 0.3 to 0.4) for a damage coefficient of 0.08. By minimizing the residual velocity error in the three test cases, the fractured strength was found to be 0.307 and agreed well with experimental observations (Figure 75). These set of parameters were used for the remainder of the study and will be referred to as IMMC-V2 (Table 19).

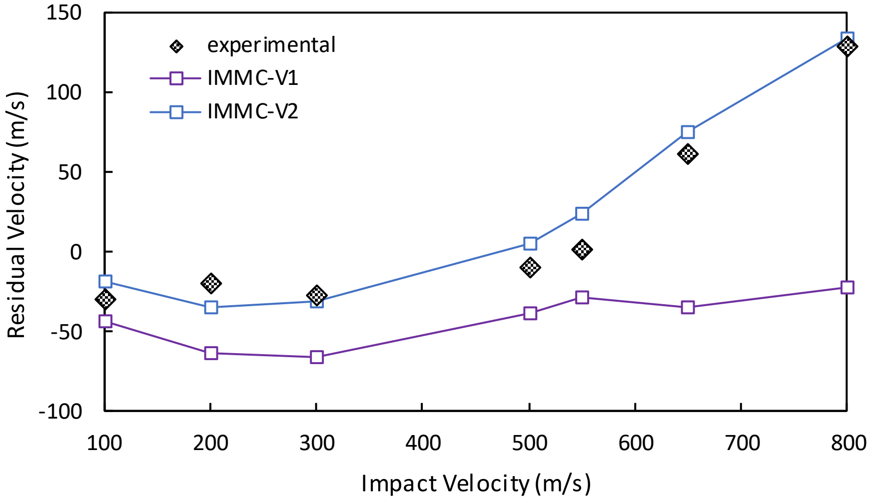

*Figure 75: Simulated projectile residual velocities versus experimental residual velocities (IMMC-V1 and IMMC-V2)*

*Table 19: Updated model parameters (IMMC-V2) based on sphere on glass residual velocities*

| | *Bulk* | *Fractured Strength* | | | *Damage* | | *Intact Strength* | | | *S.Rate* | *Equation of State* | | | *Shock* | | *Elastic* | |
|---|---|---|---|---|---|---|---|---|---|---|---|---|---|---|---|---|---|
| *Units* | - | - | - | - | - | - | - | - | MPa | - | GPa | | | GPa | | $kgm^{-3}$ | GPa |
| *Symbol* | β | B | m | $SF_{max}$ | D1 | D2 | A | n | T | c | K1 | K2 | K3 | HEL | PHEL | ρ | G |
| JH-1995 | 1 | 0.2 | 1 | 0.5 | 0.043 | 0.85 | 0.93 | 0.77 | 150 | 0.003 | 45.4 | -138 | 290 | 5.95 | 2.92 | 2530 | 30.4 |
| V1 | 0 | 0.77 | 0.66 | 0.36 | 0.038 | 0.001 | 1.05 | 0.69 | 21 | 0 | 45.4 | -138 | 290 | 5.95 | 2.92 | 2530 | 30.4 |
| V2 | 0 | **0.307** | 0.66 | 0.36 | **0.08** | 0.001 | 1.05 | 0.69 | 21 | 0 | 45.4 | -138 | 290 | 5.95 | 2.92 | 2530 | 30.4 |

## 6.3 Validation of the Soda-Lime Glass Ballistic Model

Once a suitable set of JH-2 model parameters were determined, the model was validated using three sets of experimental data: the split Hopkinson pressure bar experiments, the sphere on glass tests, and the depth of penetration tests (see chapter 3). Validation of results required quantitative comparisons between experiments and the model. Quantitative metrics from each test were used in the validation process (Table 20). The final set of parameters (IMMC-V2) were compared to Johnson and Holmquist's original set of parameters (JH-1995). It should be noted that the sphere on glass tile impact residual velocities were already used in the parameter identification portion of this study (section 6.2.3) and using a calibration data set to validate a model not typical. However, this study used two different aspects of the data set for parameter identification and validation. Also this study uses another independent dataset (depth of penetration) to validate the ability of the model to ballistic performance and uses the sphere on glass tests to validate a secondary aspect of the model performance.

*Table 20 : Validation matrix (* indicates partial validation)*

| Test | Validation Metric | Units |
|---|---|---|
| Dynamic Brazilian | Peak Sample Strain | - |
| Sphere on Glass Tile* | Damage Front Development | mm |
| Depth of Penetration | Depth of Penetration | mm |

### 6.3.1 Dynamic Brazilian Tests

The dynamic Brazilian tests were used to validate the tensile behaviour of the model. The offset in the samples produced some variability in the results, but a majority of the samples failed through the seven step failure process described in section 4.2.2 (Figure 40). Using maximum transmitter bar strain as a metric of validation, IMMC-V2 was able to predict peak strains closer to the experiments than the original JH-1995 parameters (Table 21).

*Table 21: Experimental vs. simulated transmitter bar maximum strain*

| Case | Maximum Transmitter Bar Strain | % Difference |
|---|---|---|
| Experimental | $3.14\text{x}10^{-4} \pm 0.8\ \text{x}10^{-4}$ | - |
| IMMC-V2 | $2.50\text{x}10^{-4}$ | -20 |
| JH-1995 | $5.59\text{x}10^{-4}$ | 44 |

The IMMC-V2 predicted peak strain was within one standard deviation of the experimental average ($2.3 \times 10^{-4} - 3.9 \times 10^{-4}$ mm/mm), and the prediction was within the range of experimental observations (Figure 76), whereas the JH-1995 parameters were not. The JH-1995 parameters predicted transmitter bar strains that were higher than seen in experiments suggesting that the original parameters over predicted the tensile strength of soda-lime glass.

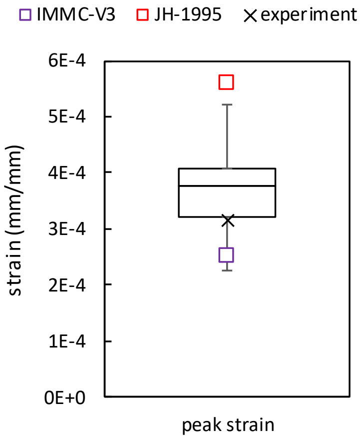

*Figure 76: Box and whisker plot of dynamic Brazilian tests with simulated bar peak strains*

The IMMC-V2 set of parameters also predicted bar strains more accurately than the original parameters (Figure 77). One difference between the experimental and simulated transmitted bar strains occurs after the peak load. In experiments, the transmitter bar strain drops to zero, indicating complete failure of the sample. However, in the simulations, the strains took longer to reach zero strain likely due to the perfectly plastic tensile behaviour of the model explored in section 6.2.2.

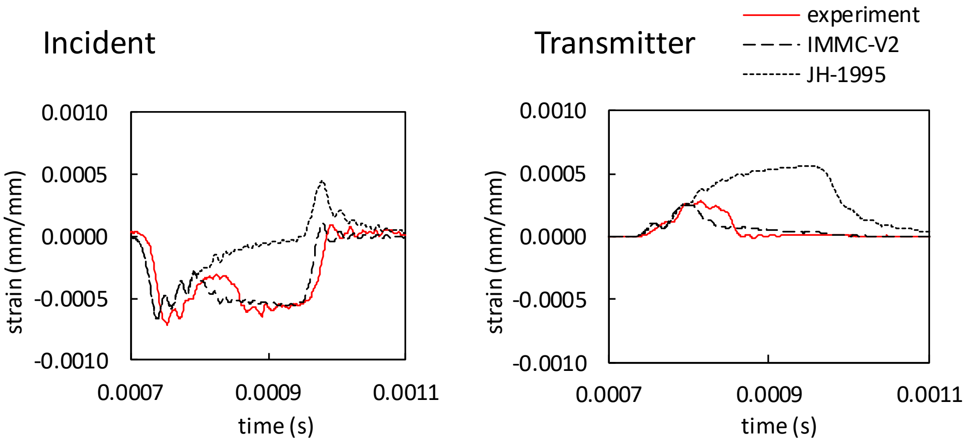

*Figure 77: Simulated and experimental dynamic Brazilian incident and transmitter bar strain versus time*

The updated parameters (IMMC-V2) also predicted the mode of failure in the tensile samples more accurately (Figure 78). In the models using the IMMC-V2 set of parameters, the simulated and experimental samples showed crack initiation (Figure 78A) and the extension of wing cracks (Figure 78B). The initial region of damage (Figure 78A) was much larger in simulation than it was in experiments. Unlike in experiments, the simulated samples did not fully bifurcate (Figure 78C-D,). However, once the samples were sufficiently loaded, the sample did form diameter cracks (Figure 78E) that eventually coalesced and resulted in failure of the sample (Figure 78F-G). The timing of each event also followed the experimental tests.

Unlike the updated IMMC-V2 parameters, the baseline JH-1995 parameters did not initiate damage until well into loading process. Although the sample damaged locally at the point of contact, the sample did not fail until reaching a peak transmitter bar strain of $5.6x10^{-4}$ mm/mm (44% higher than experimental bar strains). This is likely due to the higher tensile pressure to failure (T) used by the JH-1995 model. IMMC-V2 showed a quantifiable improvement over the JH-1995 model with respect to the prediction of tensile failure. Damage propagation in the samples were not quantified, but the updated parameters did predict failure that was more consistent with experiments than the baseline parameters (JH-1995).

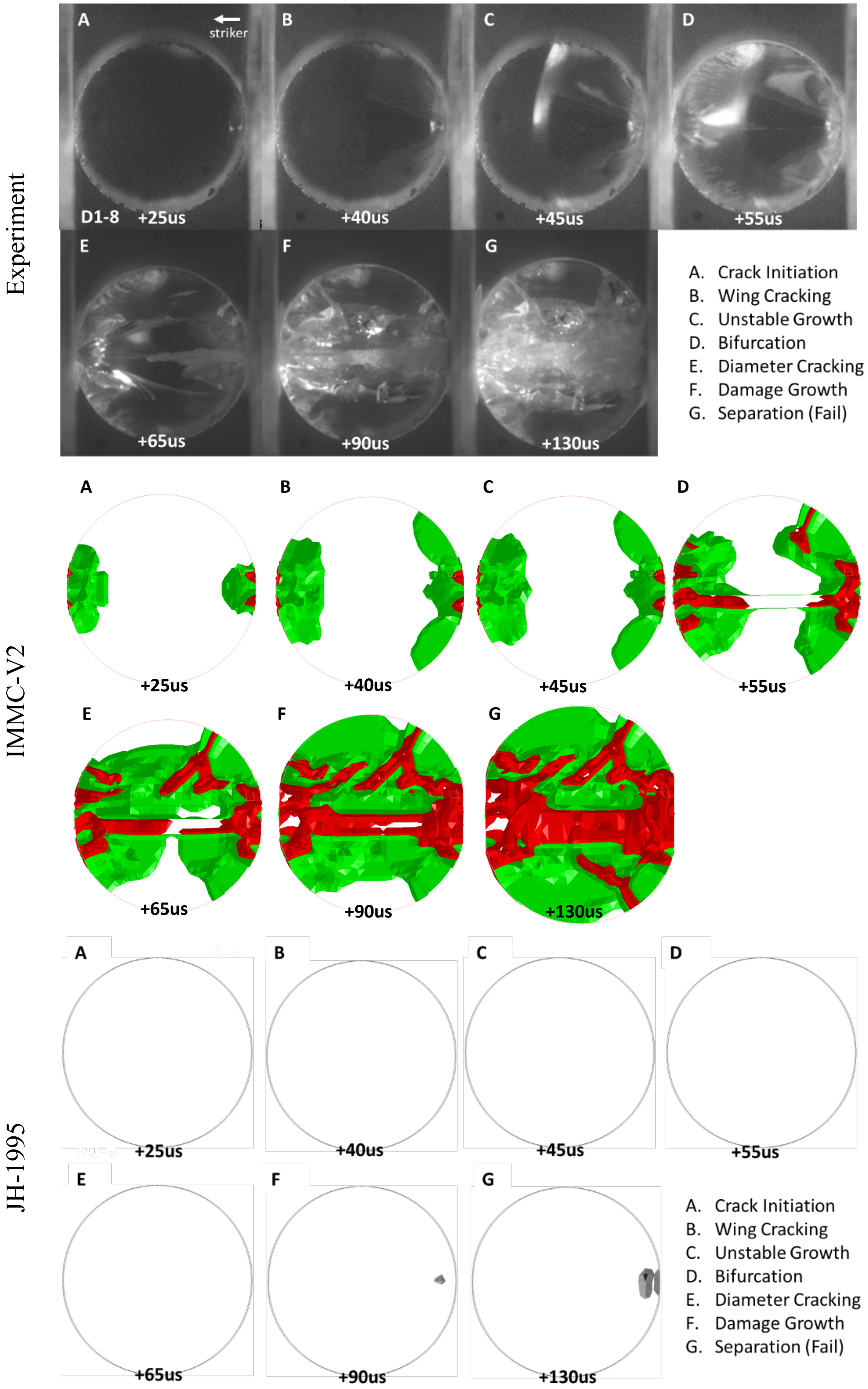

*Figure 78: Damage evolution in dynamic Brazilian tests and simulations (history variable 2, material damage plotted: white (D = 0), green (D > 0, D < 1), red (D = 1)*

### 6.3.2 Sphere on Glass Tests

The sphere on glass tests were used to assess the ability of the model to predict damage progression in soda-lime glass under ballistic impact loading. Visually, the updated parameters predicted material damage better than the JH-1995 set of parameters over the range of impact velocities (Figure 79).

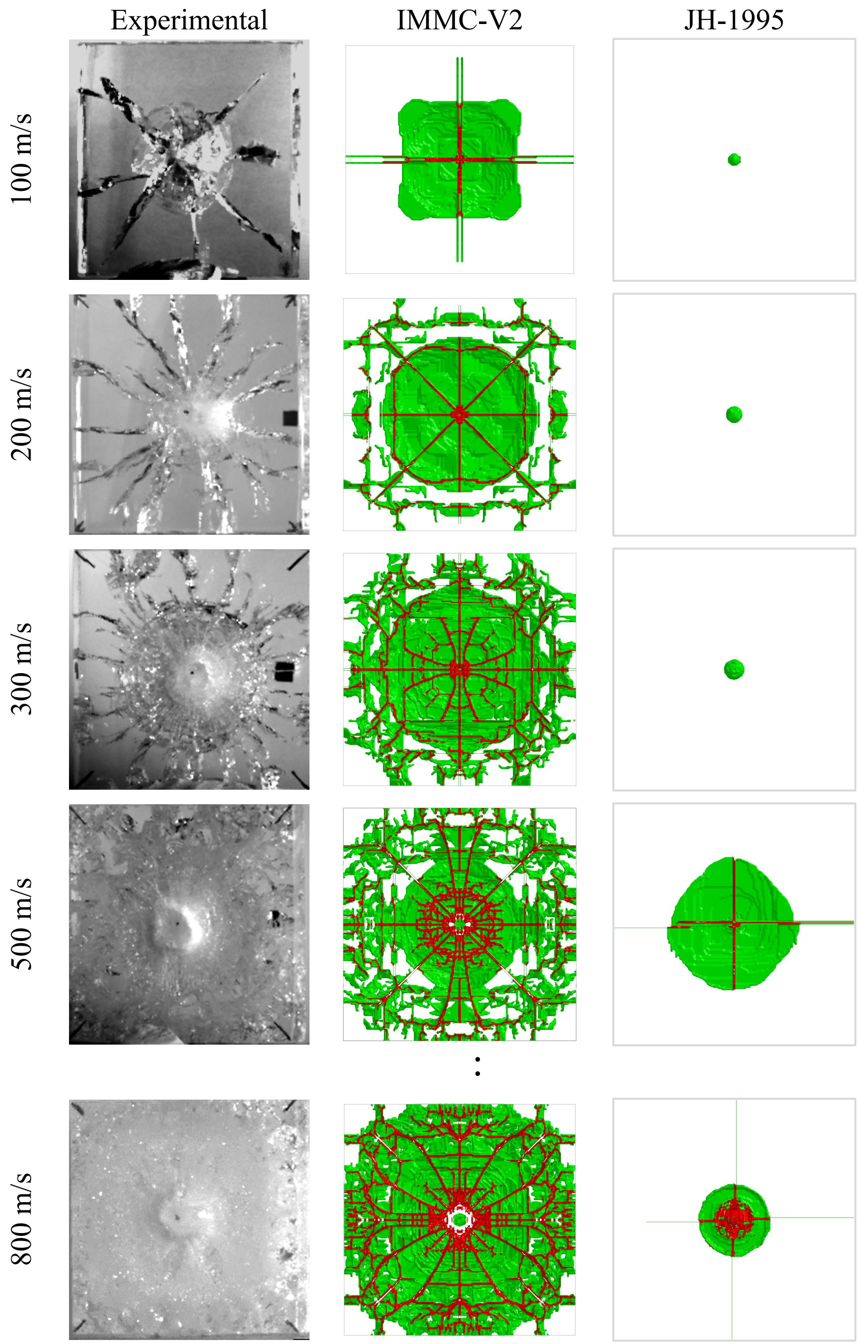

*Figure 79: Damaged sphere on glass tile simulation at 100 m/s (reverse side pictured, IMMC-V2) (history variable 2, material damage plotted: white (D = 0), green (D > 0, D < 1), red (D = 1)*

At low velocities (e.g. 100 m/s), the model predicted discrete fracture as the primary mode of failure (Figure 80). A fracture cone formed over 25 µs post impact (Figure 80A-B), and eight (8) radial cracks extended to the edges of the tile (Figure 80C).

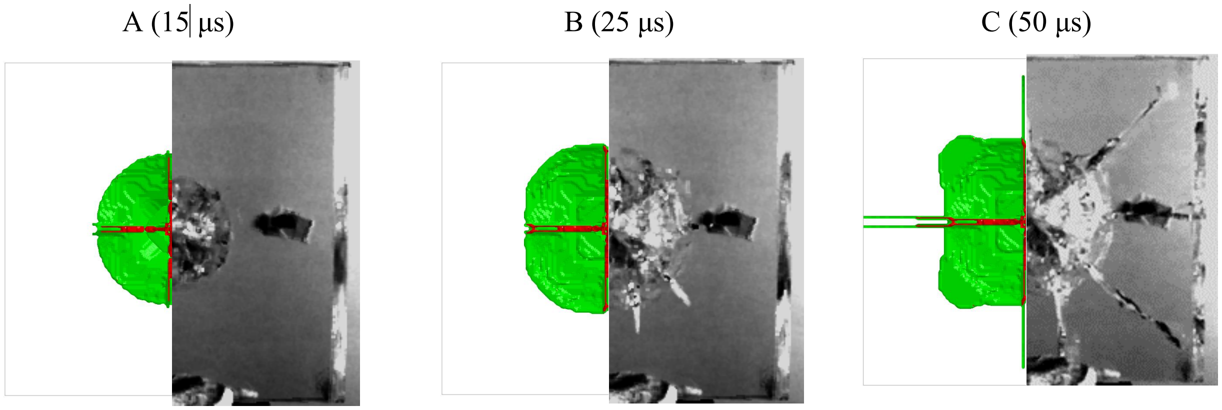
A (15 µs) B (25 µs) C (50 µs)

*Figure 80: Progression of damage for a 100 m/s impact; simulation (right), experiment (left) (history variable 2, material damage plotted: white (D = 0), green (D > 0, D < 1), red (D = 1)*

At intermediate velocities (e.g. 500 m/s), comminution and discrete fracture were present (Figure 81). Discrete fracture preceded the damage front (Figure 81A), and initiated further damage (Figure 81B). There was more discrete fracture in the model than observed in experiments.

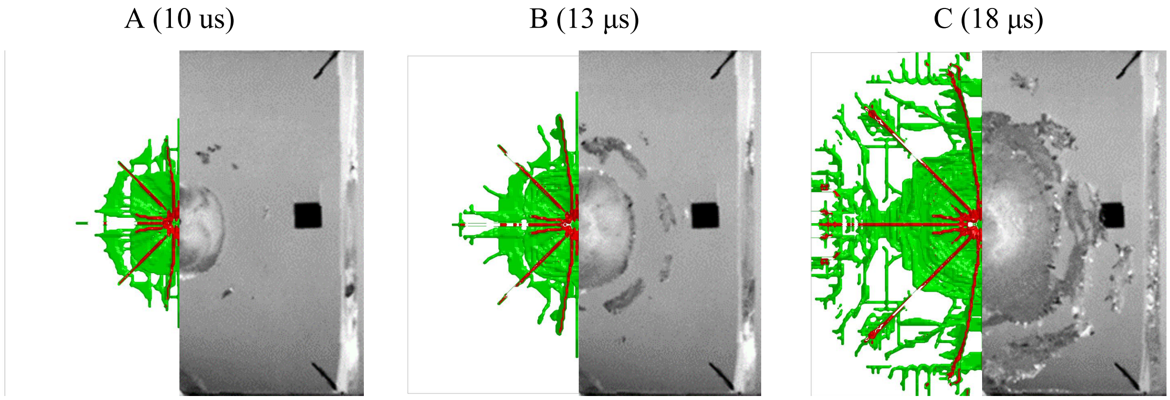
A (10 us) B (13 µs) C (18 µs)

*Figure 81: Progression of damage for a 500 m/s impact; simulation (right), experiment (left) (history variable 2, material damage plotted: white (D = 0), green (D > 0, D < 1), red (D = 1)*

At higher velocities where the projectile perforated the target (e.g. 800 m/s), bulk comminution was the dominant mode of failure (Figure 82).

.

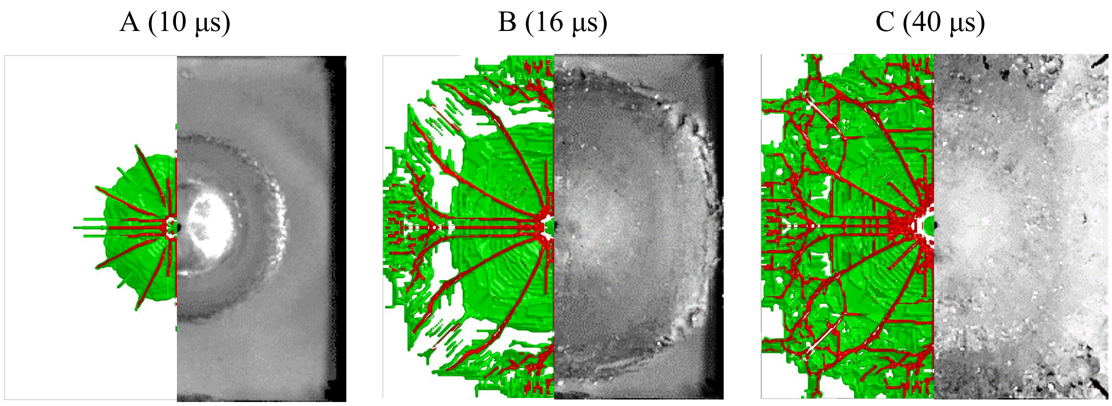

*Figure 82: Progression of damage for an 800 m/s impact; simulation (right), experiment (left) (history variable 2, material damage plotted: white (D = 0), green (D > 0, D < 1), red (D = 1)*

To quantify the progression of damage, the damage front displacements over time of the experiments and simulations were compared. At 100 m/s, the experimental damage front compared well with the simulated damage front (Figure 83).

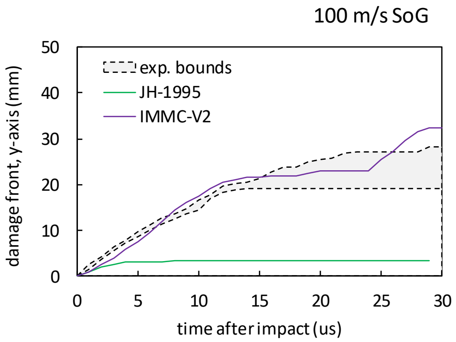

*Figure 83: SOG damage front displacements over time (100 m/s)*

At higher velocities (200, 300 m/s), discrete cracks predicted in the model dominated the damage front and caused the damage front to progress at a faster rate than seen in experiments (Figure 84).

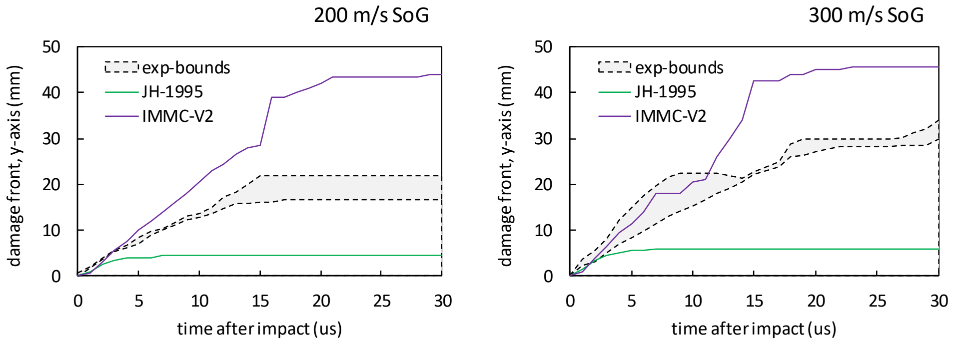

*Figure 84: SOG damage front displacements over time (200 m/s & 300 m/s)*

Some of the deviation from experimental behaviour was due a limitation of the damage tracking methodology. At 200 m/s, edge cracks produced in simulations were disjoint from the rest of the damage and not representative of the damage front. Alternative damage tracking methods should be considered in future studies. Past the point of perforation (~ 500 m/s), the whole tile was eventually comminuted. The model predicted this, but there was a sudden jump in the damage to 50 mm (the edge of the tile) at about 16 μs, caused by edge cracking produced by release waves (Figure 85). At higher velocities, the experimental ranges exceed 50 mm, likely due to the spheres missing the geometric centre of the target in the experiments.

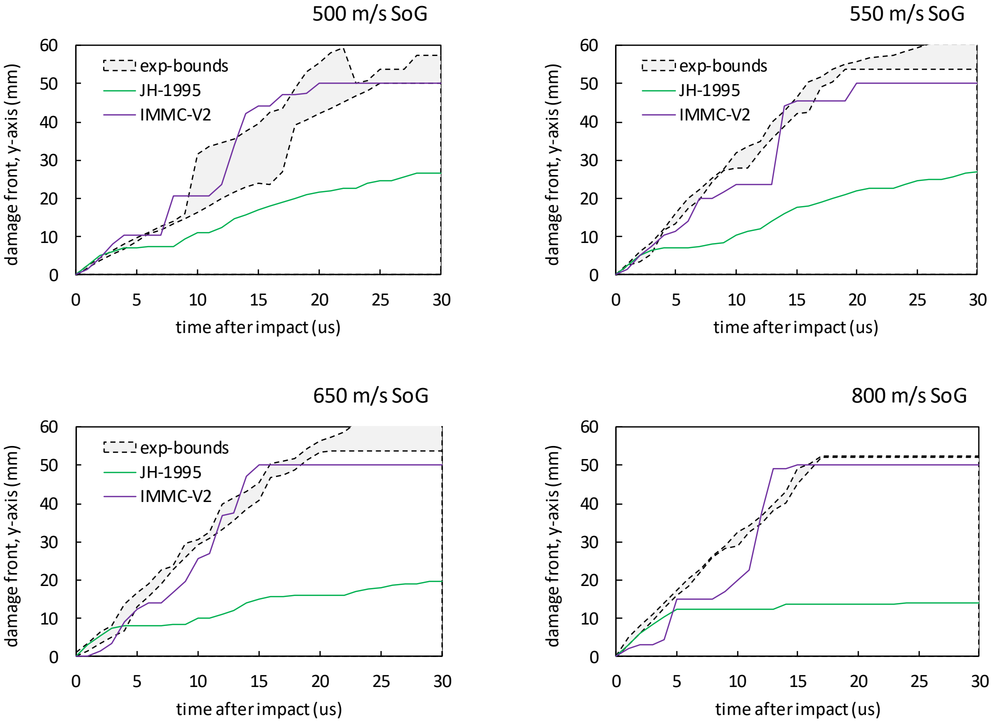

*Figure 85: SOG damage front displacements over time (500 m/s to 800 m/s)*

The models (both JH-1995 and the updated IMMC-V2 parameters), showed some mesh dependence with respect to damage formation. A good example would be the radial cracks that formed in all cases in the JH-1995 models (Figure 79), that ran straight along rows of elements, but did not progress along any other directions. Mesh dependence effects in damage formation could also be seen in the formation of the fracture cone in the updated parameters. The fracture cone was conical at first (Figure 80A-B) but took a more rectangular shape as the cone progressed through the target (Figure 80C). This is a limitation of the modelling technique used in this study.

### 6.3.3 Depth of Penetration Tests

The depth of penetration test data was used to assess the ability of the model to predict ballistic performance of soda-lime glass. Both the IMMC-V2 and JH-1995models predicted depth of penetration over time with good agreement (Figure 86).

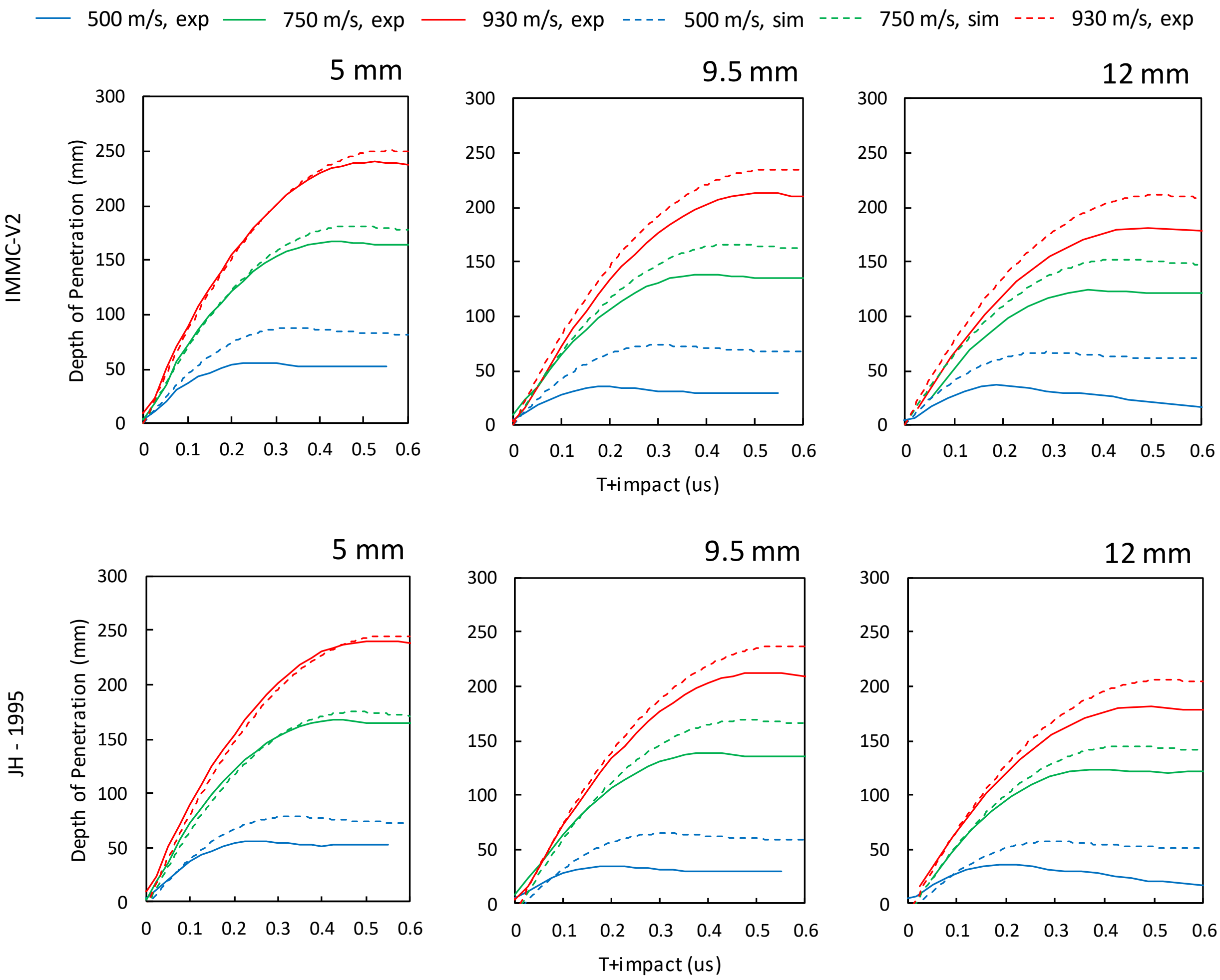

*Figure 86: Simulated (IMMC-V2 and JH-1995) depth of penetration versus time.(500 m/s, 750 m/s and 930 m/s)*

The model predicted many phenomena seen in the experiments. For example, in the 890 m/s impact case, the jacket was stripped away during impact (Figure 87). The model also predicted the ejection of soda-lime glass during impact.

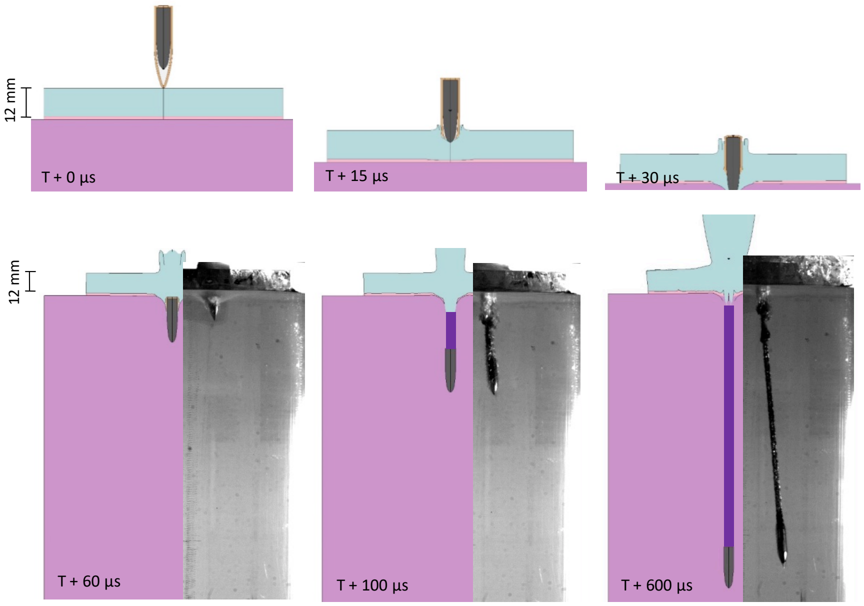

*cavity resulting from penetration enhanced for visualization purposes

*Figure 87: DOP test with 12 mm of glass with polycarbonate backing (impact velocity 890 m/s)*

Maximum depths of penetration were extracted from the projectile displacement-time data (Figure 86) and plotted against experimental ranges (Figure 88). The updated parameters predicted projectile kinematics in the depth of penetration tests with some accuracy, with predicted differences as low as 4% at higher velocities (930 m/s) and 95% in lower velocity impacts (500 m/s). Both the JH-1995 and IMMC-V2 set of parameters performed similarly, despite having different tensile strength responses (section 6.3.1) and damage propagation responses (section 6.3.2), and supports the idea that comminution of ceramic is more important in predicting local penetration than crack propagation (Anderson, 2007). Both the IMMC-V2 and JH-1995 parameters over-predicted the final depth of penetration into the polycarbonate in all test cases.

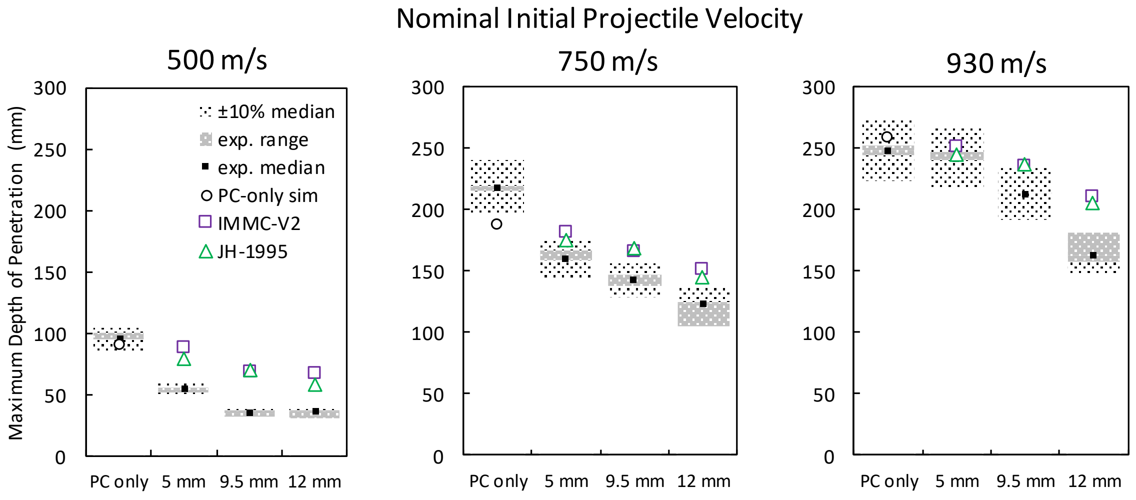

*Figure 88: Maximum projectile depth of penetrations for all depth of penetration configurations*

The updated parameters predicted projectile kinematics in the depth of penetration tests with some accuracy, with predicted differences as low as 6% at higher velocities (930 m/s) and 95% in lower velocity impacts (500 m/s). A possible contributor to the over-prediction of depths of penetration may be the stripping of the jacket from the projectile core in the tests. The tip of the core is much sharper than the jacket of the projectile. If the jacket strips off earlier in the impact (in the glass) leaving the core, this could increase the depth of penetration as the core may penetrate farther than the entire projectile. The model also over-predicted depth of penetration in cases where there was significant change in projectile trajectory upon entering the polycarbonate (for example 12 mm impact at 890 m/s). The current DOP model was modelled in quarter symmetry and therefore, the effects of the projectile deviating from an axial path (relative to the cylinder) could not be studied in these models.

Both the JH-1995 and the updated set of parameters predicted similar depths of penetration despite having different responses in both the dynamic Brazilian and sphere on glass validation cases. Generally, the models over predicted the depth of penetration of the projectile likely due to the stripping of the projectile jacket and the inability of the model to predict deviations of the projectile trajectory upon entering the polycarbonate cylinder.

## 6.4 Limitations of Numerical Methods Used in Ballistic Impact

The limitations of modelling ballistic impact problems using numerical methods were discussed briefly in section 2.4. The contact loads due to ballistic impacts result in a localized material response leading to high stress gradients and very high local deformations. Limitations of the numerical methods used in the study were identified during the verification process.

Out of the three solution methods tested (FEM, SPH and EFG), all methods were able to predict the pre-perforating velocities of the projectile with some accuracy (within an order of magnitude). Only SPH was able to predict projectile velocities over the entire range of impact velocities using published literature parameters (JH-1995) (Figure 61). This is likely due to the erosion of elements in both FEM and EFG. SPH did not require element erosion and therefore SPH kept all the material in the calculation and this may have allowed SPH to predict projectile velocities at higher impact velocities more accurately than other methods. Although SPH did predict residual projectile velocities well, the model showed poor convergence tendencies (Figure 64) with diverging projectile velocities at finer mesh sizes (Table 16). This indicated that discretization error was not the main source of modelling error. SPH also required artificially reduced time steps and SPH meshed projectiles to resolve the contact without large inter-penetrations. The FEM models were well behaved, albeit, inaccurate using literature parameters.

The sub-structuring method of meshing used in the solution methods study may be valid for EFG meshes, especially in larger parts where computational power can become a limiting factor. However, coupling SPH with FEM meshes produced spurious wave reflections at the interface in the end-to-end Hopkinson bar simulations (Figure 52) in SMP LS-DYNA R712. Since impact is a wave propagation problem (Zukas, 2004) and the interaction between stress waves control the behaviour of the solid, spurious wave reflections may adversely affect the ability of the model to predict projectile kinematics.

## 6.5 Limitations of the Developed Parameters

With material bulking enabled (beta = 1.0), single element tests showed stress oscillations in compression. Material bulking is a known phenomenon in ceramics including glass. Bulking may result in an increase in pressure when confined and result in an increase in material strength. However due to the observed oscillations during single element testing, the effects of bulking were not explored in this study. This study did not also incorporate the pressure effects on damage accumulation to simplify the analysis process. Confined compression tests at low confining pressures (100 MPa and 250 MPa) show that there may be some effect of pressure on damage accumulation in soda lime glass (Dannemann et al., 2011 Figure 89).

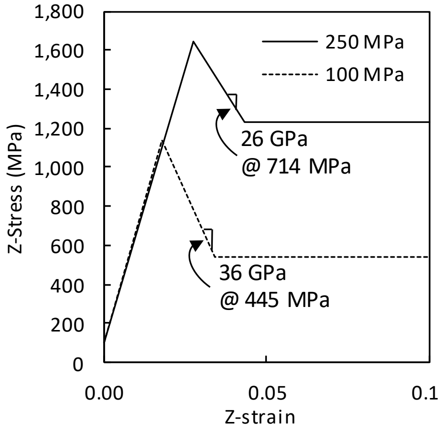

*Figure 89: Dannemann experimental axial compression data for two confinement pressures (pressure at fully fractured strength 445 MPa @ 100 MPa confinement and 714 MPa @ 250 MPa confinement)*

The JH-2 model did not attempt to quantify the effect of strain rate on damage accumulation. Using Grady's analysis (section 2.2), it was clear that there should be some effect of strain rate on damage accumulation.

As strain rate increases, the particle size should decrease. It is possible that quasi-static tests did capture levels of material comminution seen in ballistic impact. Post-impact observations of the projectiles in the sphere on glass tests showed scratches spaced roughly 2 - 10 μm apart (Figure 33), and are consistent with the size of particles found post-test in the Dannemann experiments (~ 10 μm, 2011).

There is a practical limit on a size of particles that can be produced by a certain process (Tanaka, 1966). Since the lack of strain rate effects on damage accumulation did not present a problem in ballistic validation of the model, there are two possibilities. Either the effect was compensated for by other mechanisms in the parameter identification process, or the effects were negligible. Current iterations of the Johnson-Holmquist ceramics model do include strain rate term in their damage model (Holmquist et al., 2017).

# 7. Conclusions & Recommendations

## 7.1 Experimental Conclusions

1. The sphere on glass tile tests were found to be repeatable for a wide range of impact velocities (Table 6), and provided a set of simple to model experimental data that could be used in the assessment of computational models (section 6.3.2). The sphere on glass tests also presented a wide range of damage mechanisms, including features like fracture cones, radial cracks, concentric cracks, edge cracks and material comminution (Table 7). These features were quantified through the use of high speed imaging (Table 8).

2. Successful tensile testing of soda-lime glass requires samples to be made to sub-millimeter precision. Deviations in geometry can result in non-standard modes of failure (Figure 40). However, as long as deviations in the geometry are consistent, the results can still be repeatable (Figure 39) and possibly useful (for example, as a set of validation data).

3. Depth of penetration testing on transparent materials provided a unique opportunity to study projectile penetration. Projectile kinematics (Figure 43) and final depth of penetration (Table 9) can be obtained without the use of expensive equipment (such as x-ray imaging). Overall the tests were repeatable, with higher variability in tests with thicker facing material (12 mm).

## 7.2 Simulation Conclusions

4. Ballistic impacts of soda-lime glass can be modelled using the standard finite element method (as opposed to mesh-free methods) and still be numerically stable and converge with respect to projectile velocities in the sphere on glass models, provided a fine enough mesh is used in the calculation (Table 11).

5. Of the three solution methods tested in this study (Finite Element Method, Smooth Particle Hydrodynamics and element free Galerkin), all methods predicted both perforating and non-perforating events in the sphere on glass models using literature parameters (Johnson & Holmquist, 1995) (Figure 61).

6. Element Free Galerkin exhibited good convergence tendencies (p = 2.1) in the sphere on glass models but was inaccurate with respect to projectile velocities using literature parameters (Table 11).

7. Smooth Particle Hydrodynamics predicted projectile velocities with some accuracy (Figure 61), but exhibited poor convergence tendencies and diverged at finer particle spacing in the sphere on glass tile models using literature parameters (Table 16). Additionally, SPH required smaller time steps and SPH projectiles to properly resolve contact in LS-DYNA SMP R712.

8. The sub structuring method used in this study where a mesh-free zone is supported by a FEM mesh with the goal of reducing computational costs may be a valid approach when using EFG. However, SPH exhibited spurious wave reflections at the mesh-particle interface (Figure 52), that can possibly lead to erroneous results and is therefore not recommended.

9. Problems highly dependent on contact and material erosion (like ballistic impact problems) can be highly sensitive to the order of summation when performing simulations on multiple CPUs and using LS- DYNA SMP R712 and may result variations of results between runs of identical simulations. In this study, the error was resolved by enabling the "consistent right-hand summation" in *CONTROL_PARALLEL (Table 17).

10. More realistic tensile behaviour can be achieved in the JH-2 model by adjusting the hydrostatic tensile pressure to failure (T) of the JH-2 model such that it conserves energy (section 6.2.3)

11. The decreasing rate of damage accumulation (D1) not only changed the magnitude of a response but also managed to change the mode of failure in the sphere on glass tile simulations (Figure 73).

12. The JH-2 constitutive model predicted a wide range of soda-lime glass behaviour over a range of load cases accurately with parameters derived through primarily physics based arguments (as opposed to direct calibration).

## 7.3 Experimental Recommendations

1. During the parameter identification phase, the acceleration-time profiles of the projectiles in the sphere on glass tile simulations provided a quantitative method to characterize an impact event (Figure 72). It

is possible that these acceleration-time curves can be found experimentally by tracking the projectile as it impacts the target using high-speed imaging.

Displacement data is obtained by tracking the projectile. Since acceleration is the second derivative of displacement with respect to time, even small errors in displacement tracking can result in large errors in accelerations. In simulations, peak accelerations at 100 m/s were $20 \times 10^6$ m/s$^2$. Assuming an error of 1% is low enough to determine general trends in data, this would require an error in acceleration measurements on the order of 200 000 m/s$^2$.

The initial loading phase occurs on the order of microseconds. An ideal capture rate would be around 0.1 microseconds (ten samples to capture the event). This would require a framerate of 10 million frames per second. Assuming a ¼" projectile fills the frame of a Shimadzu HPV-X (the camera used in this study), each pixel would have a spatial resolution of $2.54 \times 10^{-5}$ m/pixel. An error of one pixel would result in an error in acceleration of $254 \times 10^6$ m/s (or 10 times the peak acceleration). Subpixel techniques (like the use of DIC) and capturing only the end of the projectile may reduce this error, but would require unrealistic precision when firing the projectile. So it is clear that using high speed imaging would be restrictive (at least at the resolutions provided by current cameras). Another possibility would be to a round nose, cylindrical projectile that is fitted with either a strain gauge or an accelerometer to determine projectile acceleration with respect to time or some other capture method.

2. The dynamic Brazilian tests in the current study were useful in the validation of the ballistic glass model, but due to irregular failure of the samples (Figure 40), they could not be used to directly assess the tensile strength of soda lime glass. To facilitate diametric failure (cracking from the centre and along the diameter), the samples must be made to sub-millimetre precision. Both Dannemann (2011) and Scapin (2017) have guidelines for the dimensions of these samples. Generally, the samples must be parallel and cylindrical within 0.01 mm and have a polished surface (80/50 scratch-dig).

3. This study did not explore the effects of multiple hits on ballistic performance of soda-lime glass. Some laminate tests (glass-polycarbonate layered tiles) were performed and impacted twice. However, the tests were not repeatable due to the loss of soda lime glass in the first impact, and subsequent damage sustained by the tile post-impact. The DOP tests could provide a repeatable test bench to study the effects of multiple hits on the ballistic performance of soda lime glass. A polycarbonate front layer can be used to contain the glass between hits.

## 7.4 Simulation Recommendations

4. This study identified a possible error in the implementation of the JH-2 constitutive model in LS-DYNA. This error can be fixed, but would require access to LS-DYNA source code and a means of compiling said code. Alternatively, other constitutive models can be explored, such as *MAT_GLASS.

5. The effects of multiple hits on the ballistic performance of soda-lime glass were not characterized in this study (either though experimentation or simulation). Future work can focus on characterizing the degradation in performance (see point 3) and validating the model in multi-hit performance.

6. The model is currently validated for LS-DYNA SMP R712. Validating the model on newer platforms (like R910) and for use with MPP DYNA could extend the utility of the model. For example, if validated on MPP DYNA, the glass models could be run on high performance computing, allowing for larger, full scale models to be run quicker.

# 8. References

*Akazawa T (1943) New test method for evaluating internal stress due to compression of concrete: the splitting tension test. J Japan Soc Civil Eng 29:777–787*

*Anderson, C. E., Jr., Hohler, V., Walker, J. D., & Stilp, A. J. (1993). Penetration of Long Rods into Steel and Glass Targets: Experiments and Computations. Proc. 14th Int. Symp. on Ballistics, 1, 145-154.*

*Anderson, C. E., Jr. (2007). A Review of Computational Ceramic Armor Modelling. In Advances in ceramic armor II a collection of papers presented at the 30th International Conference on Advanced Ceramics and Composites, January 22-27, 2006, Cocoa Beach, Florida (pp. 1-18). Hoboken, N.J: Wiley.*

*Andreev, G. (1991). A review of the Brazilian test for rock tensile strength determination. Part I: Calculation formula. Mining Science and Technology, 13(3), 445-456. doi:10.1016/0167-9031(91)91006-4*

*Antoine, G., & Batra, R. (2015). Optimization of transparent laminates for specific energy dissipation under low velocity impact using genetic algorithm. Composite Structures, 124, 29-34. doi:10.1016/j.compstruct.2014.12.066*

*Askeland, D. R., Wright, W. J., Bhattacharya, & Chhabra, R. P. (2016). The science and engineering of materials. Boston, MA: Cengage learning.*

*ASM International. (1995). ASM handbook: Volume 2 properties and selection: Nonferrous alloys and special purpose materials. Ohio: ASM International.*

*ASTM International. (2018). ASTM C1273 - 18: Standard Test Method for Tensile Strength of Monolithic Advanced Ceramics at Ambient Temperatures. West Conshohocken, PA: American Society for Testing and Materials.*

*Barstow, F. E., & Edgerton, H. E. (1939). Glass-Fracture Velocity. Journal of the American Ceramic Society, 22(1-12), 302-307. doi:10.1111/j.1151-2916.1939.tb19471.x*

*Bathe, K. (2014). Finite element procedure. Englewood Cliffs, NJ: Prentice Hall.*

*Belytschko, T., Liu, W. K., Moran, B., & Elkhodary, K. I. (2006). Nonlinear finite elements for continua and structures. Chichester: J. Wiley & Sons.*

*Belytschko, T., Lu, Y. Y., & Gu, L. (1994). Element-Free Galerkin Methods. INTERNATIONAL JOURNAL FOR NUMERICAL METHODS IN ENGINEER, 37, 229-256. doi:https://doi.org/10.1002/nme.1620370205*

*Berenbaum, R., & Brodie, I. (1959). Measurement of the tensile strength of brittle materials. British Journal of Applied Physics, 10(6), 281-287. doi:10.1088/0508-3443/10/6/307*

*Bertholf, L., & Karnes, C. (1975). Two-dimensional analysis of the split Hopkinson pressure bar system. Journal of the Mechanics and Physics of Solids, 23(1), 1-19. doi:10.1016/0022-5096(75)90008-3*

*Binar, T., Švarc, J., Vyroubal, P., Kazda, T., Rolc, S., & Dvořák, A. (2018). The comparison of numerical simulation of projectile interaction with transparent armour glass for buildings and vehicles. Engineering Failure Analysis, 92, 121-139. doi:10.1016/j.engfailanal.2018.05.009*

*Birkhoff, G., Macdougall, D. P., Pugh, E. M., & Taylor, S. G. (1948). Explosives with Lined Cavities. Journal of Applied Physics, 19(6), 563-582. doi:10.1063/1.1698173*

*Bless, S. J. (2009). Failure Waves and their Possible Roles in Determining Penetration Resistance of Glass. International Journal of Applied Ceramic Technology, 7(3), 400-408. doi:10.1111/j.1744-7402.2009.02355.x*

*Bless, S. J., & Rajendran, A. M. (1996). Initiation and Propagation of Damage Caused by Impact on Brittle Materials. High-Pressure Shock Compression of Solids II, 194-218. doi:10.1007/978-1-4612-2320-7_8*

*Børvik, T., Forrestal, M. J., & Warren, T. L. (2009). Perforation of 5083-H116 Aluminum Armor Plates with Ogive-Nose Rods and 7.62 mm APM2 Bullets. Experimental Mechanics, 50(7), 969-978. doi:10.1007/s11340-009-9262-5*

*Brace, W. F., Paulding, B. W., & Scholz, C. (1966). Dilatancy in the fracture of crystalline rocks. Journal of Geophysical Research, 71(16), 3939-3953. doi:10.1029/jz071i016p03939*

*Braess, D. (2007). Finite Elements Theory, Fast Solvers, and Applications in Solid Mechanics. Cambridge: Cambridge University Press.*

*Buckley, D. H. (1973). FRICTION BEHAVIOR OF GLASS AND METALS IN CONTACT WITH GLASS IN VARIOUS ENVIRONMENTS (Tech. No. NASA TN 0-7529). Washington, D. C.: NASA.*

*Callister, W. D. (1991). Materials science and engineering. New York: Wiley.*

*Cannon, N., Schulson, E., Smith, T., & Frost, H. (1990). Wing cracks and brittle compressive fracture. Acta Metallurgica Et Materialia, 38(10), 1955-1962. doi:10.1016/0956-7151(90)90307-3*

*Carneiro, F. (1943). A new method to determine the tensile strength of concrete. Proceedings of the 5th Meeting of the Brazilian Association for Technical Rules ("Associação Brasileire De Normas Técnicas—ABNT"), 3d. section 16 September 1943, 126-129.*

*Chaudhri, M. M., & Walley, S. M. (1978). Damage to glass surfaces by the impact of small glass and steel spheres. Journal of Materials Science, 12(8), 1573-1586. doi:10.1080/01418617808235430*

*Chocron, S., Anderson, C. E., Nicholls, A. E., & Dannemann, K. A. (2010). Characterization of Confined Intact and Damaged Borosilicate Glass. Journal of the American Ceramic Society, 93(10), 3390-3398. doi:10.1111/j.1551-2916.2010.03863.x*

*Cook, R. F., & Pharr, G. M. (1990). Direct Observation and Analysis of Indentation Cracking in Glasses and Ceramics. of the American Ceramic Society, 73(4), 787-817. doi:10.1111/j.1151-2916.1990.tb05119.x*

*Corbett, B. (2006). Numerical simulations of target hole diameters for hypervelocity impacts into elevated and room temperature bumpers. International Journal of Impact Engineering, 33(1-12), 431-440. doi:10.1016/j.ijimpeng.2006.09.086*

*Cronin, D. (2013). Impact on Hard Armour Investigation (Rep.).*

*Cronin, D. S., Bui, K., Kaufmann, C., McIntosh, G., & Berstad, T. (2003). Implementation and Validation of the Johnson-Holmquist Ceramic Model in LS-DYNA. In 4th European LS-DYNA Conference.*

*Curran, D., Seaman, L., Cooper, T., & Shockey, D. (1994). Micromechanical model for comminution and granular flow of brittle material under high strain rate application to penetration of ceramic targets. International Journal of Impact Engineering, 13(1), 53-83. doi:10.1016/0734-743x(93)90108-j*
*Dannemann, K. A., Anderson, C., Chocron, S., & Spencer, J. (2011). Damage Development in Confined Borosilicate and Soda-Lime Glasses. Technical Report - US Army. doi:10.21236/ada549073*

*Dannemann, K. A., Chocron, S., Nicholls, A. E., & Anderson, C. E. (2008). Compressive damage development in confined borosilicate glass. Materials Science and Engineering: A, 478(1-2), 340-350. doi:10.1016/j.msea.2007.06.053*

*Davies, E., & Hunter, S. (1963). The dynamic compression testing of solids by the method of the split Hopkinson pressure bar. Journal of the Mechanics and Physics of Solids, 11(3), 155-179. doi:10.1016/0022-5096(63)90050-4*

*Davies, R. M. (1948). A Critical Study of the Hopkinson Pressure Bar. Philosophical Transactions of the Royal Society A: Mathematical, Physical and Engineering Sciences, 240(821), 375-457. doi:10.1098/rsta.1948.0001*

*Den Reijer, P. C., & Arbocz, J. (1991). Impact on ceramic faced armour. Unpublished doctoral thesis/dissertation.*

*Doremus, R. H., & Doremus, R. H. (1973).* Glass science*. New York: J. Wiley & Sons.*

*Dorogoy, A., Godinger, A., & Rittel, D. (2019). Modelling ballistic perforation of soda-lime glass using ductile and brittle incubation time fracture criteria. Engineering Fracture Mechanics. doi:10.1016/j.engfracmech.2019.03.030*

*Gama, B. A., Lopatnikov, S. L., & Gillespie, J. W. (2004). Hopkinson bar experimental technique: A critical review. Applied Mechanics Reviews, 57(4), 223. doi:10.1115/1.1704626*

*Gorfain, J. E., Key, C. T., & Alexander, C. S. (2016). Application of a Computational Glass Model to the Shock Response of Soda-Lime Glass. Journal of Dynamic Behavior of Materials, 2(3), 283-305. doi:10.1007/s40870-016-0066-2*

*Gorham, D. A. (1989). Specimen inertia in high strain-rate compression. Journal of Physics D: Applied Physics, 22(12), 1888-1893. doi:10.1088/0022-3727/22/12/014*

*Grady, D. (1988). The spall strength of condensed matter. Journal of the Mechanics and Physics of Solids, 36(3), 353-384. doi:10.1016/0022-5096(88)90015-4*

*Griffith, A. A. (1920). The phenomena of rupture and flow in solids. London.*

*Grujicic, M., Panduragangan, B., Coutris, N., Cheeseman, B. A., Fountzoulas, C., Patel, P., . . . Bishnoi, K. (2009). A simple ballistic material model for soda-lime glass. International Journal of Impact Engineering, 36(3), 386-401.*

*Grujicic, M., Pandurangan, B., & Coutris, N. (2011). A Computational Investigation of the Multi-Hit Ballistic-Protection Performance of Laminated Transparent-armor Systems. Journal of Materials Engineering and Performance, 21(6), 837–848. doi: 10.1007/s11665-011-0004-3*

*Grujicic, M., Bell, W., & Pandurangan, B. (2012a). Design and material selection guidelines and strategies for transparent armor systems. Materials & Design, 34, 808-819. doi:10.1016/j.matdes.2011.07.007*

*Grujicic, M., Bell, W. C., Pandurangan, B., Cheeseman, B. A., Patel, P., & Dehmer, P. G. (2012b). Effect of the tin- versus air-side plate-glass orientation on the impact response and penetration resistance of a laminated transparent armour structure. Proceedings of the Institution of Mechanical Engineers, Part L: Journal of Materials: Design and Applications, 226(2), 119–143. doi: 10.1177/1464420711433991*

*Guide for verification and validation in computational solid mechanics ASME V & V 10-2006: An American national standard. (2006). New York, NY: The American Society of Mechanical Engineers.*
*Hagan, J., & Zwaag, S. V. (1984). Plastic processes in a range of soda-lime-silica glasses. Journal of Non-Crystalline Solids, 64(1-2), 249-268. doi:10.1016/0022-3093(84)90221-7*

*Hallquist, J. O. (2006, March). LS-DYNA Theory Manual. 7374 Las Positas Road, Livermore, California.*
*Hamming, R. W. (1988). Numerical methods for scientists and engineers. New York, NY: Dover Pub.*

*Haney, E., & Subhash, G. (2012). Damage Mechanisms Perspective on Superior Ballistic Performance of Spinel over Sapphire. Experimental Mechanics, 53(1), 31-46. doi:10.1007/s11340-012-9634-0*

*Hazell, P. J. (2010). Measuring the strength of brittle materials by depth-of-penetration testing. Advances in Applied Ceramics, 109(8), 504-510. doi:10.1179/174367610x12804792635387*

*Hibbeler, R. C. (1997). Mechanics of Materials (3rd ed.). Upper Saddle River, NJ: Prentice Hall.*

*Holmquist, T. J. (1994). An Improved Computational Constitutive Model For Brittle Materials. In G. R. Johnson (Author), High-pressure science and technology -- 1993: Proceedings of the joint International Association for Research and Advancement of High Pressure Science and Technology and American Physical Society Topical Group on Shock Compression of Condensed Matter Conference held at Colorado Springs, Colorado, June 28-July 2, 1993 (pp. 981-984). New York, NY: American Institute of Physics.*

*Holmquist, T. J., Johnson, G. R., & Gerlach, C. A. (2017). An improved computational constitutive model for glass. Phil. Trans. R. Soc. A, 375(2085). doi:https://doi.org/10.1098/rsta.2016.0182*

*Holmquist, T. J., Johnson, G. R., Grady, D. E., Lopatin, C. M., & Hertel, E. S., Jr. (1995). 15th International Symposium on Ballistics. Retrieved February 2, 2018, from https://www.osti.gov/scitech/servlets/purl/41367 doi:10.2172/41367*

*Hu, W., Wu, C. T., Guo, Y., Ren, B., & Wu, Y. (2016, June 15). LS-DYNA ® Advanced FEM and Meshfree Methods for Solid and Structural Analyses – Manufacturing Applications [LS-DYNA© Training Class]. Detroit.*

*Hutton, D. V. (2004). Fundamentals of finite element analysis. Boston: McGraw-Hill Higher Education.*

*Iyengar, K. T., & Chandrashekhara, K. (1962). On the theory of the indentation test for the measurement of tensile strength of brittle materials. British Journal of Applied Physics, 13(10), 501-507. doi:10.1088/0508-3443/13/10/309*

*Johnson, G. R. (2011). Numerical algorithms and material models for high-velocity impact computations. International Journal of Impact Engineering, 38(6), 456-472. doi:10.1016/j.ijimpeng.2010.10.017*

*Johnson, G. R., & Holmquist, T. J. (1992). A computational constitutive model for brittle materials subjected to large strains. In Shock-wave and High Strain-rate Phenomena in Materials (pp. 1075-1081). Marcel Dekker.*

*Johnson, W., & Chandrasekar, S. (1992). Rupert's glass drops: Residual-stress measurements and calculations and hypotheses for explaining disintegrating fracture. Journal of Materials Processing Technology, 31(3), 413-440. doi:10.1016/0924-0136(92)90292-z*

*Karazi, S. M., Ahan, I. U., & Benyounis, K. Y. (2017). Laser Micromachining for Transparent Materials. Elsevier. doi:10.1016/B978-0-12-803581-8.04149-7*

*Kaufmann, C. K. (2004). Impact on Ceramic Materials - An Experimental and Numerical Investigation (Unpublished master's thesis). University of Waterloo.*
*Kaufmann, C., Cronin, D., Worswick, M., Pageau, G., & Beth, A. (2003). Influence of Material Properties on the Ballistic Performance of Ceramics for Personal Body Armour. Shock and Vibration, 10(1), 51-58. doi:10.1155/2003/357637.*

*Kolsky, H. (1949). An Investigation of the Mechanical Properties of Materials at very High Rates of Loading. Proceedings of the Physical Society. Section B, 62(11), 676-700. doi:10.1088/0370-1301/62/11/302*

*Kuna, M. (2013). Finite Elements in Fracture Mechanics Theory - Numerics - Applications. Dordrecht: Springer Netherlands.*

*Kupchella, R., Stowe, D., Weiss, M., Pan, H., & Cogar, J. (2015). SPH Modeling Improvements for Hypervelocity Impacts. Procedia Engineering, 103, 326-333. doi:10.1016/j.proeng.2015.04.054*

*Küppers, H. (1967). The initial course of crack velocity in glass plates. International Journal of Fracture Mechanics, 3(1). doi:10.1007/bf00188641*

*Liu, H.-G., Chen, Y.-P., Peng, X.-Q., & Xie, J.-M. (2011). A classification method of glass defect based on multiresolution and information fusion. The International Journal of Advanced Manufacturing Technology, 56(9-12), 1079–1090. doi: 10.1007/s00170-011-3248-z*

*LSTC. (2014, May 26). LS-DYNA® KEYWORD USER'S MANUAL: VOLUME I, [LS-DYNA R7.1]. Livermore, California.*

*LSTC. (2017, October 16). LS-DYNA® KEYWORD USER'S MANUAL: VOLUME I, [LS-DYNA R10.0]. Livermore, California.*

*Lucy, L. B. (1977). A numerical approach to the testing of the fission hypothesis. The Astronomical Journal,82, 1013. doi:10.1086/112164*

*Massoudi, M., & Mehrabadi, M. M. (2001). A continuum model for granular materials: Considering dilatancy and the Mohr-Coulomb criterion. Acta Mechanica, 152(1-4), 121-138. doi:10.1007/bf01176949*
*Mescall, J. F., & Tracey, C. A. (1986). Improved Modeling of Facture in Ceramic Armors (Rep.). Watertown, MA: Army Materials Technology Laboratory.*

*Mescall, J., & Weiss, V. (1983). Material behavior under high stress and ultrahigh loading rates. New York: Plenum.*

*Meyers, M. A. (1994). Dynamic behavior of materials. New York: John Wiley & Sons.*

*Monaghan, J. (2000). SPH without a Tensile Instability. Journal of Computational Physics, 159(2), 290-311. doi:10.1006/jcph.2000.6439*

*Monaghan, J., & Gingold, R. (1983). Shock simulation by the particle method SPH. Journal of Computational Physics, 52(2), 374-389. doi:10.1016/0021-9991(83)90036-0*

*Moynihan, T. J., Chou, S., & Mihalcin, A. L. (2000). Application of the Depth-of-Penetration Test Methodology to Characterize Ceramics for Personnel Protection. doi:10.21236/ada376698*
*Murakami, S. (2012). Continuum Damage Mechanics. Dordrecht: Springer.*

*Naik, N., Shrirao, P., & Reddy, B. (2006). Ballistic impact behaviour of woven fabric composites: Formulation. International Journal of Impact Engineering, 32(9), 1521-1552. doi:10.1016/j.ijimpeng.2005.01.004*

*NATO Standards Organization. (2011). Kinetic Energy and Artillery Threat (2nd ed., Vol. 1, PROCEDURES FOR EVALUATING THE PROTECTION LEVEL OF ARMOURED VEHICLES, Rep. No. AEP-55 STANAG 4569).*

*Nedderman, R. M. (2005). Statics and kinematics of granular materials. Cambridge, UK: Cambridge University Press.*

*Pilkington, L. A. B. (1969). Review Lecture. The Float Glass Process. Proceedings of the Royal Society A: Mathematical, Physical and Engineering Sciences, 314(1516), 1–25. doi: 10.1098/rspa.1969.0212*

*Progelhof, R. C., & Throne, J. L. (1993). Polymer engineering principles: Properties, processes and tests for design. Munich: Hanser.*

*Rajendran, A. (1994). Modeling the impact behavior of AD85 ceramic under multiaxial loading. International Journal of Impact Engineering, 15(6), 749-768. doi:10.1016/0734-743x(94)90033-h*

*Rajendran, A. M. (2002). Historical Perspective on Ceramic Materials Damage Models. In Ceramic armor materials by design: Proceedings of the Ceramic Armor Materials by Design Symposium held at the Pac Rim IV International Conference on Advanced Ceramics and Glass, November 4-8, 2001 in Wailea, Maui, Hawaii (Vol. 134, pp. 281-297). Westerville, OH: American Ceramic Society.*

*Reed, J. (1985). Energy losses due to elastic wave propagation during an elastic impact. Journal of Physics D: Applied Physics, 18(12), 2329-2337. doi:10.1088/0022-3727/18/12/004*

*Roache, P. J. (1994). Perspective: A Method for Uniform Reporting of Grid Refinement Studies. Journal of Fluids Engineering, 116(3), 405. doi:10.1115/1.291029*

*Rozenberg, Z., & Yeshurun, Y. (1988). The relation between ballistic efficiency and compressive strength of ceramic tiles. International Journal of Impact Engineering, 7(3), 357-362. doi:10.1016/0734-743x(88)90035-8*

*Salagame, R. R., & Belegundu, A. D. (1994). Distortion, degeneracy and rezoning in finite elements — A survey. Sadhana, 19(2), 311-335. doi:10.1007/bf02811901*

*Sathananthan, P., Sirois, A., Singh, D., & Cronin, D. (2019). Sphere on Tile Ballistic Impact Experiment to Characterize the Response of Soda Lime Glass. International Journal of Impact Engineering, 103321. doi:10.1016/j.ijimpeng.2019.103321*

*Scapin, M., Peroni, L., & Avalle, M. (2017). Dynamic Brazilian Test for Mechanical Characterization of Ceramic Ballistic Protection. Shock and Vibration, 2017, 1-10. doi:10.1155/2017/7485856*

*Schwer, L. E. (2009). Aluminum Plate Perforation: A Comparative Cast Study Using Lagrange with Erosion, Multi-material ALE and Smooth Particle Hydrodynamics. 7th European LS-DYNA Conference*

*Schwer, L. E. (2010). A brief look at *MAT_NONLOCAL: A possible cure for Erosion Illness? A Brief Look at *MAT_NONLOCAL: A Possible Cure for Erosion Illness?, 19-36.*
*Shang, J., Hatkevich, S., & Wilkerson, L. (2012). Comparison between experimental and numerical results of electromagnetic tube expansion. 12th International LS-Dyna Users Conference.*

*Sharpe, W. N. (2008). Springer Handbook of Experimental Solid Mechanics. Springer US.*

*Shockey, D. A., Marchand, A., Skaggs, S., Cort, G., Burkett, M., & Parker, R. (1990). Failure phenomenology of confined ceramic targets and impacting rods. International Journal of Impact Engineering, 9(3), 263-275. doi:10.1016/0734-743x(90)90002-d*

*Slater, J. W. (2008, July 17). Retrieved from https://www.grc.nasa.gov/www/wind/valid/tutorial/spatconv.html*

*Talladay, T. G., & Templeton, D. W. (2014). Glass Armor - An Overview. International Journal of Applied Glass Science, 5(4), 331-333. doi:10.1111/ijag.12096*

*Tanaka, T. (1966). Comminution Laws. Several Probabilities. Industrial & Engineering Chemistry Process Design and Development, 5(4), 353-358. doi:10.1021/i260020a00*

*Templeton, D. W., Holmquist, T. J., Meyer, H. W., Grove, D. J., & Leavy, B. (2002). A Comparison of Ceramic Material Models. CERAMIC TRANSACTIONS, 134, ceramic armor materials by design symposium, 299-308.*

*Thornton, J. I., & Cashman, P. J. (1986). Glass Fracture Mechanism—A Rethinking. Journal of Forensic Sciences, 31(3), 818-824. doi:10.1520/jfs11092j*

*Ti, K. S., Huat, B. B., Noorzaei, J., Jaafar, M. S., and Sew, G. S. (2009). A review of basic soil constitutive models for geotechnical application. Electronic Journal of Geotechnical Engineering, 14:1–18.*
*Ulusay, R., & Hudson, J. A. (2007). The complete ISRM suggested methods for rock characterization, testing and monitoring 1974-2006. Ankara: International Soc. for Rock Mechanics, Commission on Testing Methods.*

*Vivek, R., & Ramesh, K. (2014). Residual Stress Analysis of Commercial Float Glass Using Digital Photoelasticity. International Journal of Applied Glass Science, 6(4), 419–427. doi: 10.1111/ijag.12106*

*Van Der Velde, O. (2015). Finding the strength of glass: A mechanical and fractographic research of glass' biaxial strength for structural purposes (Unpublished master's thesis). TU Delft.*
*Walley, S. M. (2010). Historical review of high strain rate and shock properties of ceramics relevant to their application in armour. Advances in Applied Ceramics, 109(8), 446-466. doi:10.1179/174367609x422180*

*Weinhold, C. (2013). U.S. Patent No. US 8,603,616 B1. Washington, DC: U.S. Patent and Trademark Office.*

*Wereszczak, A. A., & Anderson, C. E. (2014). Borofloat and Starphire Float Glasses: A Comparison. International Journal of Applied Glass Science, 5(4), 334–344. doi: 10.1111/ijag.12095*

*Wilkins, M. L. (1968). Third Progress Report of Light Armor Program (Rep. No. UCRL-50460). Livermore, CA: Lawrence Livermore National Laboratory.*

*Wilkins, M. L. (1978). Mechanics of penetration and perforation. International Journal of Engineering Science, 16(11), 793-807. doi:10.1016/0020-7225(78)90066-6*

*Wilkins, M. L. (1978). Mechanics of penetration and perforation. International Journal of Engineering Science, 16(11), 793-807. doi:10.1016/0020-7225(78)90066-6*

*Willmott, G. R., & Radford, D. D. (2005). Taylor impact of glass rods. Journal of Applied Physics, 97(9), 093522. doi:10.1063/1.1889249*

*Wu, C., Li, L., & Thornton, C. (2005). Energy dissipation during normal impact of elastic and elastic–plastic spheres. International Journal of Impact Engineering, 32(1-4), 593-604. doi:10.1016/j.ijimpeng.2005.08.007*

*Zhang, X., Hao, H., & Ma, G. (2015). Dynamic material model of annealed soda-lime glass. International Journal of Impact Engineering, 77, 108-119. doi:10.1016/j.ijimpeng.2014.11.016*

# Appendix A: Parameter Sensitivity Study

To determine the relative effects of the JH-2 parameters on a ballistic impact problem, a parameter study was conducted. A quarter model of the sphere on glass tests (see section 5.2), was constructed (Figure A.1) and model parameters were changed independently of one another. The JH-1995 parameters were used the baseline. Six parameters were altered (C, B, FS, T, D1 & D2). Residual velocities were recorded at 100 m/s, 500 m/s and 800 m/s to determine the effects at a range of velocities (Figure A.2).

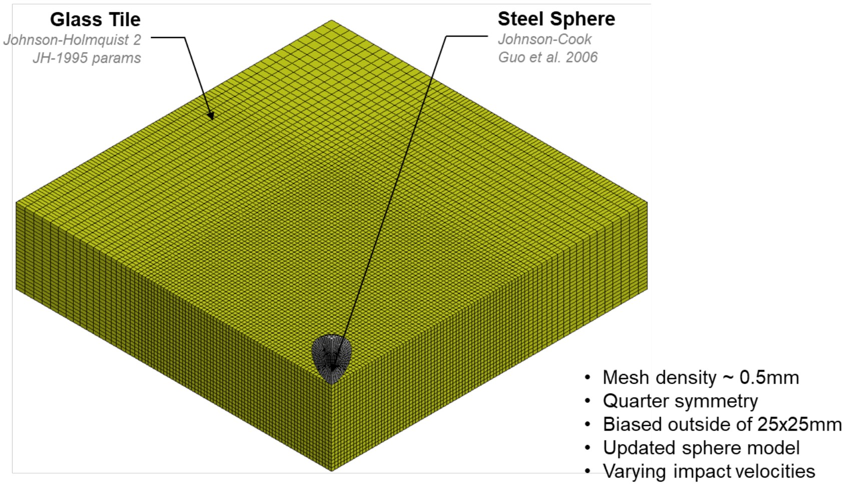

- Mesh density ~ 0.5mm
- Quarter symmetry
- Biased outside of 25x25mm
- Updated sphere model
- Varying impact velocities

*Figure A.1: Sphere on glass tile model used in parameter sensitivity study.*

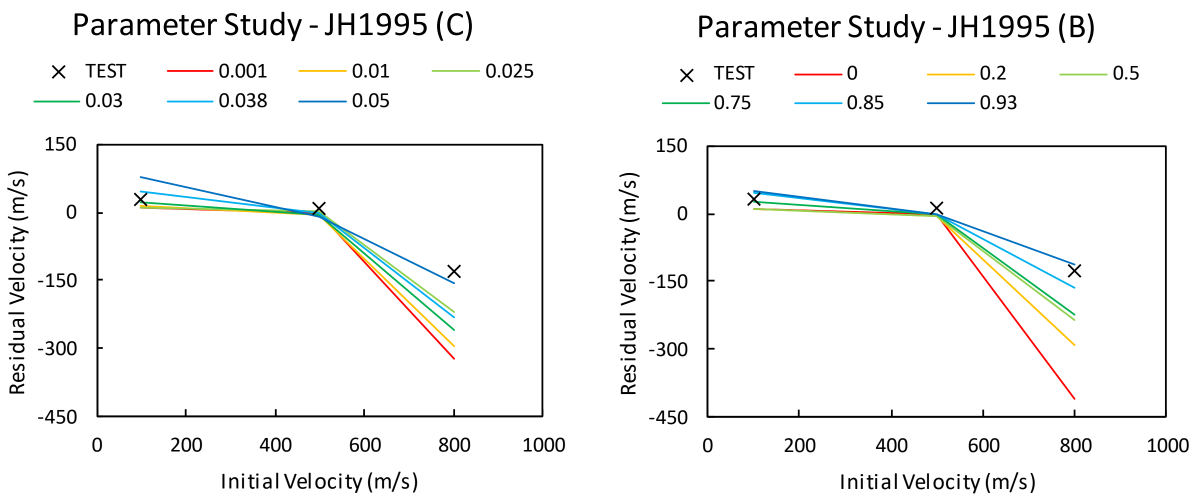

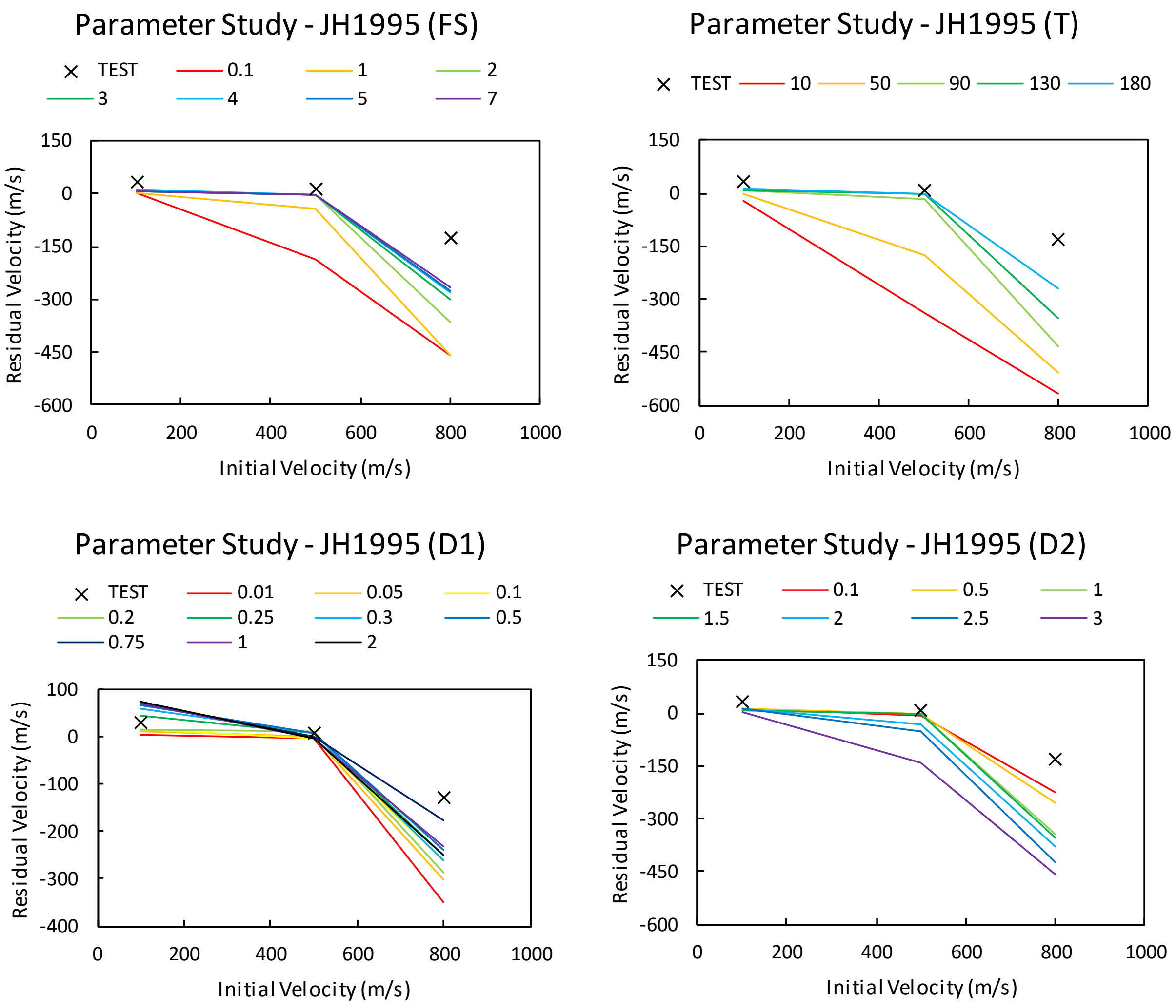

*Figure A.2: Relative effect of JH-2 parameters on projectile residual velocities.*

# Appendix B: Least-Squares Fitting Code (MATLAB)

```
clear
clc
Seqt = 0.05
Pt = -Seqt/3.0
%get xy data
spdata = [
% Pressure    Eq. Stress  (GPa)
% Tensile Strength Contstraint
Pt, Seqt
% … x 9
Pt, Seqt
% Dannemann Pressure-Strength Data
0.42768595  , 1.291525424
0.522727273 , 1.569491525
0.719008264 , 2.152542373
0.671487603 , 1.718644068
0.896694215 , 1.955932203
0.92768595  , 2.484745763
1.200413223 , 2.857627119
1.355371901 , 2.566101695
1.326446281 , 2.796610169
1.355371901 , 2.884745763
1.623966942 , 3.379661017 ];

pnorm = spdata(:,1)./2.92;
snorm = spdata(:,2)./4.545;

spnorm = [pnorm snorm];

%get model to minimize
nlr_model = @(b) sum((snorm - (b(1).*(pnorm+b(2)).^b(3))).^2)

%function to evaluate
yield_eval = @(b,pstar) b(1).*(pstar+b(2)).^b(3);

%initial guesses
b0 = [0.93,0.20,0.77];
bmin = [0,0,0];
bmax = [10,1,1];

result = fminsearchbnd(nlr_model, b0,bmin,bmax);

plot(2.92.*pnorm, 4.54.*snorm, 'k.')
hold on
pplot = linspace(-.150,4);
plot(2.92.*pplot, 4.54.*yield_eval(result, pplot), 'r')
plot(2.92.*pplot, 4.54.*yield_eval([0.93,150/2920,0.77], pplot), 'k')
xlabel('Pressure (GPa)')
ylabel('Stress (GPa)')
yield_eval(result, pnorm)
result
ylim([0 4]);
title ('Intact Strength Curve');
legend({'Dannemann (2011)','IMMC','JH-1995'},'Location','northwest')
yield_eval(b0,pnorm)
```